

Novel Magnetic Nanoparticles for Medical Applications

Thesis submitted for the degree of
Doctor of Philosophy
at the University of Leicester

by

Katie Dexter MPhys
Condensed Matter Physics Group
Department of Physics and Astronomy
University of Leicester

December 2017

Abstract

The main purpose of this work was to investigate methods of producing nanoparticles with higher magnetic moments and saturation magnetisations than in current commercially available (Fe-oxide) nanoparticles. Such nanoparticles could be used to realise novel treatment of cancer, magnetic nanoparticle hyperthermia (MNH). These particles can also be optimized for use as magnetic resonance imaging (MRI) contrast agents and in a novel imaging system called magnetic particle imaging (MPI).

It is advantageous to use pure Fe as the nanoparticle material as it has a much higher magnetisation than Fe-oxide, so these nanoparticles should perform better in MNH. In medical applications however, pure Fe needs to be encapsulated in a biocompatible shell, so high-performance nanoparticles need to be produced as core-shell particles. Here, data is presented from Fe@Cu, Fe@Ag, Fe@Al, Fe@Mg core-shell nanoparticles, and a set of pure Fe nanoparticles.

Transmission electron microscopy (TEM) images were utilised for obtaining detailed nanoparticle size and shape distributions, and, specifically, were also analysed using a novel parameter: the geometry factor. The geometry factor is the ratio of the true area of the nanoparticle (in 2-D), divided by its maximum possible area if it were scaled to a sphere: a less subjective manner to judge particle shape than by eye. Composition analysis was performed using energy dispersive x-rays (EDX).

The magnetic nature of our nanoparticles was investigated through magnetometry. Measurement of the magnetisation (M-H curves) enabled the magnetic moments of the samples to be determined.

Our best performing nanoparticles were pure Fe with a saturation magnetisation higher than that of bulk pure Fe ($0.220 \text{ Am}^2/\text{g}$) of $0.262 \pm 0.026 \text{ Am}^2/\text{g}$ at 300 K. These nanoparticles were produced at room temperature ($21 \pm 2 \text{ }^\circ\text{C}$), a mean diameter of $\sim 18 \text{ nm}$, and a geometry factor of ~ 0.8 , indicating they are likely to contain mostly cuboctahedral shapes.

Acknowledgements

Firstly, I must mention my colleagues and friends in the CMP group at the University of Leicester. I am greatly appreciative of all their time and effort moulding me into the scientist that I am today. I must also thank my collaborators for all their hard work in providing me with the data I required for this thesis.

My heartfelt thanks go to Stu for all his hours teaching me how to use SLUMPS, for fixing things I kept breaking, for keeping entertained in the office, and for the many discounted Tigers tickets over the years. You are one in a million, Stu.

My supervisor Bakes, who took me on after my first year. Without you this thesis would never have materialised, and I would have probably given up on this work years ago. Keep doing what you do, you make the world of difference to students like myself.

I thank Lucky, the black Labrador who I have walked almost every week for the past 2 years. She will never know how much happiness she has brought into my life.

There are so many friends that have helped me over the years – I would be lost without them. Without the endless coffee breaks and alcohol-filled evenings, I would not have coped. I would also like to thank all those who ran endless obstacle course races with me over the years. In particular, must express my gratitude to Emma, for her friendship has made this past year much more enjoyable than it otherwise would have been.

I cannot thank Andy enough, he has a source of immense joy over the past year or so. I could not imagine submitting this thesis without his support.

Of course, I must mention my mum. I could not ask for anything more out of her, she is thoughtful, insightful, fun, and above all, lives in a lovely warm country where the beer is cheap!

Inevitably, I have to thank the VC and HoC for all their support over the course of this project, for they tried their hardest to push me to my limits.

Finally, I would also like to thank the Graduate Dean, and to chance, that this thesis was submitted on my 27th birthday – truly the best birthday gift yet! To the pub!

Figures

Figure 1 - Schematic of the UHV sputter source, SLUMPS.	10
Figure 2 – Schematic of the core shell evaporator.....	13
Figure 3 – Photograph of the sample holder and induction coil for the heating tests carried out by INSA, Toulouse.	15
Figure 4- TEM images of the pure Fe nanoparticles. Scale bar for each image shown in bottom left.....	15
Figure 5 – Some common interactions of a high energy electron beam with a sample. 16	
Figure 6 - Schematic of the TEM (Amin, 2012).....	18
Figure 7 –temperature readings of the inner and outer bore thermocouples whilst ramping up and down in power. Exponential fits are over plotted to each.....	23
Figure 8 – the relation between the inner and outer bore thermocouple temperature readings. a) splits the data into ramping up and down with individual exponential fits whereas b) has only one exponential over both ramping up and down.....	24
Figure 9 – the inner bore thermocouple temperature readings whilst the power is ramped up.	26
Figure 10 - Simplistic illustration of domain structure and magnetic energy. From (Zureks, 2008).....	33
Figure 11 – A generic M-H plot illustrating hysteresis, magnetisation saturation, residual magnetism and coercivity (coercive force). (Electronics-micros, 2017).....	34
Figure 12 – Typical B-H curve of a superparamagnetic material.....	37
Figure 13 - Susceptibility heating via superparamagnetic nanoparticles, hysteresis heating through blocked nanoparticles and stirring (viscous heating) due to friction with nanoparticle size dependency illustrated for each. Image from (Binns, 2010).....	39
Figure 14 - Regions of the amplitude and frequency of an alternating magnetic field (AMF) applied to tissues that would generate direct eddy current heating at a power density of 0.025 W cm^{-3} or stimulate peripheral nerves and cardiac tissue. (Pankhurst , Thanh, Jones, & Dobson, 2009)	43
Figure 15 - MRI with (right) and without (left) a contrast agent added on a patient following a stroke where the blood-brain barrier has been broken down (Hellerhoff, 2010)	46

Figure 16 - The spin-echo sequence illustrated with red arrows to represent the proton spins within hydrogen. (Morley, 2011)	48
Figure 17 – a Manipulation of the nonlinearity of M-H curves gives a steady cyclic signal when an oscillating magnetic field is applied. Fourier analysis reveals the harmonic frequencies. When a static magnetic field is also applied to saturate the nanoparticles (as with b), the induced signal reveals no significant frequencies when put through Fourier analysis. (Gleich & Weizenecker, 2005)	52
Figure 18 - Diagram of 3D MPI Scanner taken from (Weizenecker, Gleich, Rahmer, Dahnke, & Borgert, 2009)	52
Figure 19 - Setup of a single-sided MPI scanner made up of two concentrically positioned transmit coils (light grey) and a separate receive coil (dark grey). The selection field is generated by direct currents of opposite direction (indicated by arrows). The 1-D field of view is indicated schematically as a black line (Sattel, et al., 2009)	53
Figure 20 - TEM images of the pure Fe nanoparticles. Scale bar for each image shown in bottom left.....	58
Figure 21 – A snapshot of the process in which data is extracted from a TEM image. From left to right: the raw TEM image, the binarised image and the edge tracking from ImageJ.....	60
Figure 22 - Geometry Factor Histograms with Weibull distributions overplotted for pure Fe samples synthesised with the core shell evaporator operating at 263.8 ± 44.7 °C, (left) and 702.6 ± 43.6 °C (right).....	62
Figure 23- The geometry factor vs the temperature of the core shell evaporator for the pure Fe samples. The plotted values are the means of Weibull distributions fits plus a one sigma error bar. The dotted lines indicate the separation of the cubic (0.4 – 0.7), cuboctahedral (0.7 – 0.8), and spherical (0.8 – 1.0) regions.....	63
Figure 24 - The percentage of cubes (black squares), cuboctahedrals (red circles), and spheres (blue triangles) for each of the pure Fe samples.	64
Figure 25 - An example histogram plus lognormal fit for the pure Fe sample made at 702.6 ± 43.6 °C. The means and one sigma values (error bars) plotted in Figure 26 are taken from this lognormal plot and others like it from the other samples.	65
Figure 26 - The area of each pure Fe 2-D nanoparticle vs the temperature of the shell evaporator. Plotted values are the means of the sample from lognormal fitting with one sigma error bars. A linear fit has been added.	65

Figure 27- The diameter of each pure Fe 2-D nanoparticle vs the temperature of the core shell evaporator. Plotted values are the means of the sample from lognormal fitting with one sigma error bars.....	66
Figure 28- Geometry factor versus area for all 1929 pure Fe nanoparticles analysed in this dataset. The dotted lines indicate the separation of the cubic (0.4 – 0.7), cuboctahedral (0.7 – 0.8), and spherical (0.8 – 1.0) regions	67
Figure 29 - Number of spheres (blue), cuboctahedrals/cbhl (red) and cubic nanoparticles in each area bin (200 nm ² in size) for the pure Fe samples.	68
Figure 30 - Raw magnetometry data of the pure Fe samples in the SQUID at 5 K. a) shows the full data range obtained from ± 5 T, and b) shows the same data but between ± 1 T to show the hysteresis behaviour in more detail.	74
Figure 31- Raw magnetometry data of the pure Fe samples in the SQUID at 300 K. a) shows the full data range obtained from ± 5 T, and b) shows the same data but between ± 1 T to show the hysteresis behaviour in more detail.	75
Figure 32 - An example of the Langevin fit applied to the pure Fe sample produced with the core shell evaporator operating at $225.9 \pm 44.9^\circ\text{C}$ at 5 K in the SQUID magnetometer.	76
Figure 33 - Saturation Magnetisation from Langevin fits of the raw hysteresis curves shown in Figure 30 and Figure 31, plotted against the temperature of the core shell evaporator the pure Fe nanoparticles were subjected to.	76
Figure 34 – Example polygon area measurement for the $1137.7 \pm 43.2^\circ\text{C}$ pure Fe sample at 300 K. The grey shaded section indicates the absolute measured area of the polygon and what is plotted in Figure 35.....	77
Figure 35 – Polygon areas of the hysteresis curves from the pure Fe samples plotted in Figure 30 and Figure 31.....	77
Figure 36 – Preliminary data from the pure Ag sample, 4 % volume fraction Fe in an Ag matrix, and an 8 % volume fraction Fe in an Ag matrix sample, achieved using an RF field to stimulate the production of heat, and measuring this directly with an infrared camera.	80
Figure 37 - Magnetometry measurements of Fe in Ag (black), SiO (red), and Ge (green). Plots in b) is the same data shown in a) but within the magnetic field range ± 1 T to illustrate the hysteresis loops more clearly.	81

Figure 38 - TEM images of the Fe@Cu nanoparticles. Scale bar for each image is shown in the bottom left of the images.	86
Figure 39 - Fe@Cu sample produced at 1130.6 ± 43.2 °C with a mean geometry factor of 0.730 ± 0.009 (1 standard deviation) with a scale parameter value of 0.770 and a shape parameter of 9.48 from the Weibull fitting (red line).	89
Figure 40 – Geometry factor for the 9 TEM samples produced with the core shell evaporator loaded with ~ 1 g Cu. The dotted lines indicate the separation of the cubic (0.4 – 0.7), cuboctahedral (0.7 – 0.8), and spherical (0.8 – 1.0) regions. The values come from Weibull fits of the raw data with \pm one sigma error bars.	89
Figure 41 - Geometry factor for the 9 Fe@Cu TEM samples (black) and the 12 pure Fe TEM samples (red) produced with the core shell evaporator. The dotted lines indicate the separation of the cubic (0.4 – 0.7), cuboctahedral (0.7 – 0.8), and spherical (0.8 – 1.0) regions. The values come from Weibull fits of the raw data with \pm one sigma error bars.	90
Figure 42 – The percentage of cubes (geometry factor 0.4 -0.7, black squares), cuboctahedrals (0.7 – 0.8, red circles) and spheres (0.8 - 1.0, blue triangles) versus the core shell temperature when loaded with ~ 1 g of Cu.	91
Figure 43 - The diameter of each Fe@Cu 2-D nanoparticle vs the temperature of the core shell evaporator. Plotted values are the means for the sample obtained from lognormal fitting with one sigma error bars.	92
Figure 44 – Example histogram and lognormal fitting for the 218.0 ± 44.9 °C Fe@Cu sample.	92
Figure 45 – Comparison of nanoparticle diameter for the 12 pure Fe TEM samples (red squares) and the 9 Fe@Cu TEM samples (black circles).	93
Figure 46 – Geometry factor versus area for all 1148 Fe@Cu nanoparticles analysed in this dataset. The dotted lines indicate the separation of the cubic (0.4 – 0.7), cuboctahedral (0.7 – 0.8), and spherical (0.8 – 1.0) regions.	93
Figure 47 – Number of spheres (blue), cuboctahedrals/cbhl (red), and cubic (black) Fe@Cu nanoparticles in each area bin (200 nm^2) in size.	94
Figure 48 – Dark field TEM image of an example Fe@Cu nanoparticle created with the shell evaporator operating at 316.8 ± 44.6 °C. The numbers represent three of the areas measured with point-and-shoot EDX.	99

Figure 49 - 2 regions of EDX spectra (EDXS) TEM analysis of the Fe@Cu nanoparticle in Figure 48, with a) referring to the background, point 1, and b) the area within the particle, denoted with the number 3 in Figure 48.	99
Figure 50 – Three line-scans of a Fe@Cu nanoparticle from the 316.4 ± 44.6 °C sample. Notice the increase in Fe as the line crosses the centre of the nanoparticle and the abundance of O at the surface.	100
Figure 51 - Phase diagram for Fe-Cu binary alloy, with the bottom right section highlighted as this is the appropriate temperature range and percentage of Fe/Cu for these experiments. Figure from (Hansen, 1958).	101
Figure 52 – EDX mapping of Cu and Fe for 3 nanoparticles in the 316.8 ± 44.6 °C sample.	102
Figure 53 - 2 regions of EDXS TEM analysis of the Fe@Cu nanoparticle in Figure 54, with a) referring to the background, point 1, and b) the area within the particle, denoted by the number 3 in Figure 54.	103
Figure 54 - Dark field TEM image of an example Fe@Cu nanoparticle created with the shell evaporator at 777.4 ± 43.5 °C. The numbers represent three of the areas measured with point-and-shoot EDX.	103
Figure 55 – EDX mapping of a nanoparticle from the 777.4 ± 43.5 °C sample. The abundance of Cu, and Fe have been highlighted in the two panels, middle and right, respectively, with the far-left panel showing the original dark field TEM image.	103
Figure 56 - Dark field TEM image of an example Fe@Cu nanoparticle created with the shell evaporator at 994.1 ± 43.1 °C. The numbers represent three of the areas measured with point-and-shoot EDX.	104
Figure 57 - 2 regions of EDXS TEM analysis of the Fe@Cu nanoparticle in Figure 56 with a) referring to the background, point 1, and b) the area within the particle, denoted with the number 3 in Figure 56.	104
Figure 58 - EDX mapping of a Fe@Cu nanoparticle from the 994.1 ± 43.1 °C sample. The abundance of Fe and Cu have been highlighted in the two panels, middle and right, respectively, with far-left the original dark field TEM image.	105
Figure 59 - Dark field TEM image of an Fe@Cu nanoparticle created with the shell evaporator at 1130.6 ± 43.2 °C. The circled area represents the two areas measured with Point and Shoot EDXS.	105

Figure 60 - A region of EDXS TEM analysis of the Fe@Cu nanoparticle in Figure 59. The top spectrum is from the whole particle, (left image in Figure 59), and the bottom spectra is from the edge of the nanoparticle (right image in Figure 59).....	106
Figure 61 - EDX mapping of a nanoparticle from the 1130.6 ± 43.2 °C sample. The abundance of Fe and Cu have been highlighted in the two panels, middle, and right, respectively, with the far-left panel the original dark field TEM. image.	106
Figure 62 - Cu atomic percentage across the four core shell temperatures measured with point-and-shoot EDX.....	107
Figure 63 - Example Langevin fitting for the Fe@Cu 773.6 ± 43.5 °C sample	109
Figure 64 - Magnetometry data from the Fe@Cu sample measured in the SQUID at 5 K. a) shows the full data range obtained from ± 5 T and b) shows the same data but between ± 1 T to show the hysteresis behaviour of the nanoparticles in more detail.....	110
Figure 65 – Magnetometry data from the Fe@Cu samples measured in the SQUID at 300 K. a) shows the full data range obtained from ± 5 T and b) shows the same data but between ± 1 T to show the hysteresis behaviour of the nanoparticles in more detail. .	111
Figure 66 – Saturation magnetisation of Fe@Cu samples from Langevin fits of the raw hysteresis curves shown in Figure 64 and Figure 65, plotted against the temperature of the core shell evaporator the nanoparticles were subjected to.....	112
Figure 67 – Comparison of the saturation magnetisation of Fe@Cu and Fe samples from Langevin fits of the raw magnetometry data of samples measured at 300 K in the SQUID magnetometer.....	113
Figure 68 – Comparison of the saturation magnetisation of Fe@Cu and Fe samples from Langevin fits of the raw magnetometry data of samples measured at 5 K in the SQUID magnetometer.....	114
Figure 69 - Example hysteresis curve from the sample produced with the core shell evaporator operating at 773.6 ± 43.5 °C with the grey shaded section representing the area enclosed by the loop, plotted in Figure 70.	114
Figure 70 -The polygon areas from the three Fe@Cu samples, measured at 5 K and 300 K in the SQUID magnetometer. The values plotted arise from plots such as Figure 69.	115
Figure 71 - The polygon areas of hysteresis from the three Fe@Cu samples (black) and the 13 pure Fe samples (red)nmeasured at 300 K in the SQUID magnetometer.....	115

Figure 72 - The polygon areas of hysteresis loops from the Fe@Cu samples (black) and the pure Fe samples (red) measured at 5 K in the SQUID magnetometer.....	116
Figure 73 – Example TEM images of the Fe@Ag samples.	123
Figure 74 – Left: Geometry factor histogram with a Weibull distribution overplotted for the 1137.7 ± 43.2 °C Fe@Ag sample. Right: The geometry factor versus the temperature of the core shell evaporator, where the plotted values are the means for the Weibull distributions fits (\pm one sigma error bar).	124
Figure 75 - The geometry factor versus the temperature of the core shell evaporator, where the plotted values are the means for the Weibull distributions fits \pm one sigma error bar. The data from the Pure Fe samples in black (see Chapter 4: Pure Fe Studies for further information) and the Fe@Ag samples in red. The dotted lines indicate the separation of the cubic (0.4 – 0.7), cuboctahedral (0.7 – 0.8), and spherical (0.8 – 1.0) regions.....	125
Figure 76 - The percentage of cubes (black squares), cuboctahedrals (red circles), and spheres (blue triangles) for each Fe@Ag sample.	126
Figure 77 – Left: An example histogram plus lognormal fit for the Fe@Ag sample made at 800.7 ± 43.4 °C. The means and one sigma values (error bars) from this and the other 4 samples are plotted in the right-hand plot.....	126
Figure 78 - The diameter of each 2-D nanoparticle vs the temperature of the core shell evaporator for both the Fe@Ag and the pure Fe samples from Chapter 4: Pure Fe Studies. Plotted values are the means of the sample from lognormal fitting with one sigma error bars.....	127
Figure 79 – Geometry factor as a fraction of area for all 455 nanoparticles analysed in this dataset. The dotted lines indicate the separation of the cubic (0.4 – 0.7), cuboctahedral (0.6 – 0.8), and spherical (0.8 – 1.0) regions	127
Figure 80 – Left: the number of spheres (blue), cuboctahedrals/cbhl (red) and cubic (black) Fe@Ag nanoparticles in each area bin (200 nm ² in size). Right: the percentage of spheres (blue), cuboctahedrals/cbhl (red) and cubic (black) nanoparticles within the same area bins.	128
Figure 81 - Geometry factor for the 10 pure Fe TEM samples produced without coolant supplied to the sputter head. The dotted lines indicate the separation of the cubic (0.4 – 0.7), cuboctahedral (0.7 – 0.8), and spherical (0.8 – 1.0) regions. The values come from Weibull fits of the raw data with \pm 1 sigma error bars.	131

Figure 82 - The percentage of cubes (geometry factor 0.4 -0.7, black), cuboctahedrals (0.7 – 0.8, red) and spheres (0.8 - 1.0, blue) versus the core shell temperature for the 10 pure Fe TEM samples without coolant supplied to the sputter head.	132
Figure 83 - The diameter of each 2-D pure Fe (no coolant) nanoparticle vs the temperature of the core shell evaporator. Plotted values are the means for the sample obtained from lognormal fitting with one sigma error bars.	133
Figure 84 - Comparison of nanoparticle diameter for the 12 pure Fe TEM samples with the coolant supplied to the sputter head (black squares), and the 10 pure Fe (no coolant) TEM samples (red triangles).....	133
Figure 85 – Geometry factor versus area for all 1077 pure Fe (no coolant) nanoparticles analysed in this dataset. The dotted lines indicate the separation of the cubic (0.4 – 0.7), cuboctahedral (0.6 – 0.8), and spherical (0.8 – 1.0) regions.....	134
Figure 86 - Number of spheres (blue), cuboctahedrals/cbhl (red), and cubic (black) nanoparticles in each area bin (200 nm ²) in size for the pure Fe (no coolant) samples.	135
Figure 87 - Raw magnetometry data for the pure Fe (no coolant) samples from SQUID measurements at 5 K. a) shows the full data range obtained from -5 T to +5 T and b) shows the same data but between -1 T and +1 T to show the hysteresis behaviour in more detail.....	137
Figure 88 - Raw magnetometry from the pure Fe (no coolant) data from SQUID measurements at 300 K. a) shows the full data range obtained from -5 T to +5 T and b) shows the same data but between -1 T and +1 T to show the hysteresis behaviour in more detail.....	138
Figure 89 - Saturation Magnetisation obtained from Langevin fits of the raw hysteresis curves shown in Figure 87 and Figure 88, plotted against the temperature of the core shell evaporator to which the pure Fe (no coolant) nanoparticles were subjected.....	139
Figure 90 - Comparison of the saturation magnetisation of the pure Fe samples (no coolant, red) and the pure Fe samples (with coolant, black) obtained from Langevin fits to the raw magnetometry data for samples measured at 5 K (left) and 300 K (right)..	139
Figure 91 – Fe@Cu (no coolant) sample produced at 693.1 ± 43.6 °C with the Weibull fitting overplotted (red line).....	143
Figure 92 – Geometry factor for the 4 Fe@Cu (no coolant) TEM samples produced with the core shell evaporator loaded with ~ 1 g Cu. The dotted lines indicate the separation	

of the cubic (0.4 – 0.7), cuboctahedral (0.7 – 0.8), and spherical (0.8 – 1.0) regions. The values come from Weibull fits of the raw data with ± 1 sigma error bars.....	144
Figure 93 - Geometry factor for the 9 Fe@Cu (with coolant) TEM samples (red) and the 4 Fe@Cu (no coolant) TEM samples (black) produced with the core shell evaporator. The dotted lines indicate the separation of the cubic (0.4 – 0.7), cuboctahedral (0.7 – 0.8), and spherical (0.8 – 1.0) regions. The values come from Weibull fits of the raw data with ± 1 sigma error bars.	144
Figure 94 - The percentage of cubes (geometry factor 0.4 -0.7, black squares), cuboctahedrals (0.7 – 0.8, red circles) and spheres (0.8 - 1.0, blue triangles) versus the core shell temperature when loaded with ~ 1 g of Cu.	145
Figure 95 - The diameter of each 2-D Fe@Cu (no coolant) nanoparticle vs the temperature of the core shell evaporator. Plotted values are the means for the sample obtained from lognormal fitting with one sigma error bars.....	146
Figure 96 - The diameter of each 2-D nanoparticle vs the temperature of the core shell evaporator for the Fe@Cu (no coolant) samples (black squares) and the Fe@Cu (with coolant) samples (red triangles). Plotted values are the means for the sample obtained from lognormal fitting with \pm one sigma error bars.	146
Figure 97 – Geometry factor versus area for all 456 nanoparticles analysed in the Fe@Cu (no coolant) dataset. The dotted lines indicate the separation of the cubic (0.4 – 0.7), cuboctahedral (0.7 – 0.8), and spherical (0.8 – 1.0) regions.....	147
Figure 98 - Number of spheres (blue), cuboctahedrals/cbhl (red), and cubic (black) nanoparticles in each area bin (200 nm ²) in size for the Fe@Cu (no coolant) samples.	147
Figure 99 - Raw data from SQUID magnetometry of the Fe@Cu (no coolant) samples with measurements at 300 K. a) shows the full data range obtained from -5 T to +5 T and b) shows the same data but between -1 T and +1 T to show the hysteresis behaviour in more detail.	149
Figure 100 - Raw data from SQUID magnetometry of the Fe@Cu (no coolant) samples with measurements at 5 K. a) shows the full data range obtained from -5 T to +5 T and b) shows the same data but between -1 T and +1 T to show the hysteresis behaviour in more detail.	150

Figure 101 - Saturation Magnetisation from Langevin fits of the raw hysteresis curves shown in Figure 99 and Figure 100, plotted against the temperature of the core shell evaporator that the Fe@Cu (no coolant) nanoparticles were subjected to. 151

Figure 102 - Saturation Magnetisation of the Fe@Cu (no coolant) sample (red), and the Fe@Cu (coolant) sample (black) plotted against the temperature of the core shell evaporator for the 5 K (left) and 300 K (right) measurements in the SQUID magnetometer..... 151

Figure 103 - Saturation Magnetisation of the Fe@Cu (no coolant) sample (red), and the pure Fe (no coolant) sample (black) plotted against the temperature of the core shell evaporator for the 5 K (left) and 300 K (right) measurements in the SQUID magnetometer..... 152

Contents

Chapter 1: Introduction (1 - 8)

Chapter 2: Experimental Methods (9 - 26)

1. Introduction	9
2. Equipment.....	9
3. Calibration of the Shell Evaporator	22

Chapter 3: Magnetic Nanoparticle Theory and Medical Applications (27 - 54)

1. Introduction	27
2. Basic Magnetism	28
3. Superparamagnetic behaviour	35
4. Magnetic Nanoparticle Hyperthermia	38
5. Magnetic Resonance Imaging	46
6. Magnetic Particle Imaging	50
7. Summary.....	54

Chapter 4: Pure Fe Studies (55 - 83)

1. Introduction	55
2. TEM Data	57
3. Magnetometry Data	71
4. Heating Data.....	79
5. Conclusions	82

Contents

Chapter 5: Fe@Cu Studies (84 - 119)

1. Introduction	84
2. TEM Data	86
3. EDX Data	97
4. Magnetometry Data	108
5. Conclusions	118

Chapter 6: Other Core Shell Studies (120 - 154)

1. Introduction	120
2. Fe@Ag.....	121
3. No coolant Fe	129
4. No coolant Fe@Cu	141
5. Conclusions	154

Chapter 7: Conclusions (154 - 160)

References (161 - 164)

Chapter 1: Introduction

Nanoparticles have become an intense area of research due to their many potential applications. These applications span areas of research including biomedicine, electronics, materials science, and energy. Nanoparticles are of great fundamental and applied interest due to their unique size-dependant properties. This size-dependence is due to a significant proportion of the atoms being located at the surface of the particle, and also quantum size effects when the nanoparticles are below ~ 10 nm. To illustrate why the size of the particle has such a critical role determining the properties of the particle, picture a 2 cm diameter sphere. This sphere has approximately 1 in 10 million atoms at the surface whereas a 10 nm diameter particle has around 1 in 10 located at the surface. Surface atoms are in a different chemical bonding environment compared to atoms in the bulk/centre of the particle in that they have a reduced coordination. A reduced coordination leads to a narrowing of energy bands, which affects electronic and magnetic properties. It is therefore clear that when approximately 10 % of the atoms are at the surface, the surface atoms' behaviour become significant to the properties of the overall nanoparticle. These are arguably the two key reasons why materials at the nanometre scale behave so differently to the corresponding bulk material.

For this project, the unique magnetic properties exhibited by nanoparticles, such as large magnetic moments, are investigated in order to assess their suitability for use in diagnostic imaging and cancer therapy; these applications are explained in more detail in the following paragraphs. Firstly, a brief overview of magnetic nanoparticle theory is required to understand how they may be manipulated for such applications. To be useful in magnetic resonance imaging (MRI), the nanoparticles behave as a contrast agent; i.e. they increase the contrast in the image between neighbouring tissues. This allows for clearer images, thus an increased chance of an accurate diagnosis for the patient as MR contrast is generally rather poor when compared to that of computerised tomography (CT). MRI does, however, allow for soft tissue imaging, which X-ray images do not and so effort into synthesising appropriate contrast agents is clearly valuable. The addition of an appropriate biological moiety to the nanoparticle means that they also have the potential to bind to a particular type of cell – not unlike an enzyme in a reaction it is catalysing. If the colloid is then injected into the patient and time allowed for the nanoparticles to bind to cells of interest then there is a possibility of locating metastasised

cancers. This would revolutionise cancer detection as metastasised tumours are often difficult to spot and are usually rather large when they are finally detected – thus making treatment less effective; it is common knowledge that the earlier the treatment, the higher the success.

For use in the treatments of cancer, magnetic nanoparticles have the interesting characteristic whereby they can be manipulated to heat their surroundings, and therefore potentially used in killing cells through excessive heating. When subjected to an applied alternating magnetic field, magnetic nanoparticles warm their immediate environment, and when cells are heated from their normal 37 °C up to 42 °C, their proteins are denatured and their membranes become permeable, ultimately resulting in cellular death. The nanoparticle heat output efficiency is highly dependent on their size due to the nature of nanoparticle magnetism. Nanoparticles with sizes less than ~ 50 nm are magnetically single-domain. Those with sizes \lesssim 15 nm are superparamagnetic and heat their surroundings through superparamagnetic heating. A slightly larger nanoparticle does not exhibit superparamagnetism but is ferromagnetic and follows a hysteresis loop when subjected to such an applied alternating magnetic field. The heat output in this case is proportional to the area of the hysteresis loop. Increasing the size further will not produce heat through magnetic interactions as the particle will no longer be single domain or have lower number of multi-domains. The particles will produce some heat through frictional forces as the whole particle is physically moved by the applied alternating magnetic field.

Nanoparticle uses encompass a wide range of medical applications including magnetic nanoparticle hyperthermia and MRI as detailed above. Another particularly interesting nanoparticle application in medicine is the concept of targeted drug delivery whereby specific drugs are attached to nanoparticles and the nanoparticles guided to the treatment area – be this with targeted biological proteins and/or the addition of a magnetic field gradient. The nanoparticles are then triggered by a radiofrequency pulse, for example, to release the drugs. This allows for a targeted therapy with significantly reduced side-effects.

With an estimated 14.1 million new cancer cases occurring in 2012, cancer is a leading cause of disease across the globe. Cancer is also a leading cause of death with 8.2 million deaths worldwide in 2012 (Ferlay, et al., 2013). Furthermore, when the death rate from

cancer is compared with other illnesses (stroke, heart disease and influenza/pneumonia) over the last sixty years, the probability of dying from cancer is almost the same today as it was previously, unlike deaths from other major illnesses which have drastically fallen in the same time period (Davies, 2013).

The reason cancer is such a problem to diagnose and treat in modern medicine is due to the body's inability to recognise cancerous cells. Healthy cells become cancerous due to a fault in the replication or death processes, whether this is caused by a genetic factor or an environmental stress (such as trauma, poisoning, radiation). Whereas bacteria and viruses have different antigens, or markers, on their surface, cancerous cells generally 'look' similar to healthy cells to the body's immune system. This means that the immune system does not recognise a cancerous cell as foreign and does not remove it as it would with a pathogen.

The current cancer treatments can include chemotherapy, radiotherapy, hormone therapy, and surgery. Chemotherapy poisons the cells and causes many side effects as it cannot distinguish between cells that are healthy, and those that are cancerous. Chemotherapy is often used in conjunction with radiotherapy as this is more effective; radiotherapy uses high energy x-rays to kill the cancer. However, radiotherapy can also damage nearby healthy cells although these can often repair themselves whereas cancerous cells cannot. Although these treatments are improving and success rates are also increasing, they are still riddled with side-effects because they are not targeting the cancerous cells alone, and healthy cells are adversely affected by the treatments.

Magnetic nanoparticle hyperthermia (MNH) is designed to be a targeted therapy for cancer, thus having far less side-effects than the current treatment options. The theory behind MNH is simple. A hydrosol sample (i.e. a colloidal suspension in water) with magnetic nanoparticles dispersed throughout is injected into a cancer site. An alternating magnetic field is applied to the patient and, as the magnitude and frequency of this applied alternating magnetic field is kept relatively low, only the magnetic nanoparticles are significantly affected by the field. They respond to this stimulus by releasing heat into the surroundings, warming the cells nearby. When these cells reach a high enough temperature (~ 42 °C), their proteins denature and their cell membranes become permeable, ultimately killing them.

The final application targeted by this project is a new imaging tool known as magnetic particle imaging (MPI). This utilises the non-linear nature of superparamagnetic nanoparticles to produce 3D maps of tracer density – much like a gamma camera does with radioactive tracers. It works by applying an alternating magnetic field to a small area of superparamagnetic nanoparticles while the rest of the nanoparticles in the field of view are saturated. The nanoparticles allowed to react to the applied alternating magnetic field are detected and their magnitude, and therefore tracer density, can be inferred. This new imaging modality can be set up in a similar manner to that required for MNH, and so imaging and treatment of a cancer could theoretically be achieved in one sitting with one machine. To realise this technology, targeting cells of interest would allow for detection and treatment of not only the primary tumour, but also any metastasised tumours throughout the body.

Unfortunately, current nanoparticles available commercially do not produce enough heat for magnetic nanoparticle hyperthermia treatment to be realised. However, as Maier-Hauff K., et al. (2007) have shown, magnetic nanoparticle hyperthermia can be used in conjunction with chemotherapy, radiotherapy and other gold-standard treatments for cancer, and can increase the rates of remission and survival rates. Brusentsov, et al., (2002) have also demonstrated how these currently available (albeit sub-par) nanoparticles have the ability to completely eradicate a tumour in a small rat, where the field frequency and magnitude can be significantly larger than in humans. These papers strongly suggest that with higher performing nanoparticles, i.e. those with a higher magnetic moment and/or a larger hysteresis loop (significance explained later in this chapter), MNH can be realised as a stand-alone cancer treatment with substantially fewer side-effects than today's available treatment options.

It may seem obvious that to increase the heating from the magnetic nanoparticles one could simply increase the applied alternating field magnitude and frequency, so that more (larger) hysteresis loops are formed per second or, for superparamagnetic nanoparticles, there are more rotations of the internal magnetic moments per second. However, as the field magnitude and frequency are increased, Eddy currents form. Eddy current heating produces serious adverse reactions which patients would most certainly like to avoid, including nerve and muscle stimulation. The Atkinson-Bresovich limit refers to the upper limit for the field frequency and magnitude of the applied alternating magnetic field used

in magnetic nanoparticle hyperthermia. If the applied alternating field exceeds this limit ($H_o \times f = 4.85 \times 10^8 \text{ Am}^{-1} \text{ s}^{-1}$), the patient may start experiencing nerve and muscle stimulation, which is of particular concern near the heart. If the applied magnetic field frequency and magnitude is increased further, the patient may well be warmed, not just by the magnetic nanoparticles' reaction to the field, but the whole body will be heated. This is evidently not a solution to overcome the minimal heating from the current sub-par nanoparticles.

To improve upon the magnetic nanoparticle hyperthermia treatment, one must look to the nanoparticle properties, and seek to improve their magnetic characteristics. If it is possible to design and prepare nanoparticles with higher magnetic moments, and higher saturation magnetisations, they will therefore produce more heat than their predecessors. Magnetic nanoparticle hyperthermia may then no longer be a potential treatment, rather, an actual contender for cancer treatment.

There are multiple methods to synthesise nanoparticles including gas phase, chemical precipitation, and sol-gel. Chemical synthesis methods generally offer a high yield whereas the yield from physical synthesis is often low. So why use gas-phase synthesis to create our nanoparticles? The answer is simple. It is in principle straight forward for us with our experimental set-up to change the size, shape, and composition of the core and shell material of the synthesised nanoparticles. This allows us to relatively quickly cycle through multiple variations of core and shell materials, and in principle optimise the structure for a given property. Once the optimum nanoparticle structure for each of the three applications has been created, then a higher yield, and faster production method (such as chemical synthesis) may well need to be employed to realistically enable their use in medical applications. It is also worth noting that nanoparticles are generally highly reactive when synthesised, and a gas phase method which operates under ultra-high vacuum allows for clean synthesis. This is particularly important when considering that the nanoparticles we intend to use are pure iron and well known to oxidise readily in air and water.

Although gas-phase synthesis is not known for its ease of deposition into water, this problem has been solved previously by the research group here at the University of Leicester (Binns, et al., 2012). To produce a sample in hydrosol, a hollow tube is filled

with liquid nitrogen and aligned with the nanoparticle beam. A separate jet of water vapour is introduced, aimed at the same liquid nitrogen cooled tube, and of course subsequently freezes onto the surface. The water vapour and nanoparticles co-deposit, giving nanoparticles dispersed in an ice matrix. This is then removed and allowed to melt, producing a liquid sample containing the nanoparticles. Previous molecular dynamics simulations also carried out within our research group (Binns, et al., 2012) indicated that there should be no significant deformation of the nanoparticles when they impact into the ice matrix; they also predicted that there should be no melting of the ice structure (confirmed by experiments).

Magnetic nanoparticle hyperthermia is strongly dependant on nanoparticle size (since nanoparticle properties are size-dependent) so a synthesis technique with tight size control is extremely beneficial. In this thesis, a gas-phase, ultra-high vacuum method is presented with the ability to synthesise core-shell nanoparticles with independent variation of the core size and shell thickness. The method also allows for control over the particle shape (Atkas, 2014), and liquid suspensions can also be produced from the gas-phase (as outlined above (Binns, et al., 2012)). It is advantageous to use pure Fe as the core material as it has a much higher magnetisation than Fe oxide, so the nanoparticles should perform better in MNH. In medical applications however, pure Fe needs to be encapsulated in a biocompatible shell, so high-performance nanoparticles need to be produced as core-shell particles. The core-shell (notation: core material@shell material) nanoparticles created during this project include Fe@Cu, Fe@Ag, Fe@Al, and Fe@Mg, alongside a pure Fe sample set.

To analyse the nanoparticles synthesised throughout this project, multiple techniques have been employed. Firstly, transmission electron microscopy (TEM) is utilised for its ability to not only image the nanoparticles in 2-D, showing their shape and size, but also for energy dispersive x-ray (EDX) measurements so that the composition of the sample can be investigated. Further to this, TEM not only images the surface, as scanning electron microscopy or as atomic force microscopy do, it allows for imaging of the whole nanoparticle, including the core, so that the shells can be viewed and analysed thoroughly. TEM is used here not only for shape and size distributions of the nanoparticles, but also for composition analysis.

Secondly, to investigate the magnetic nature of the nanoparticles, the use of magnetometers is paramount, enabling the magnetic moments of the samples to be measured. Two such instruments were employed in this project are a vibrating sample magnetometer (VSM) operated by collaborators at the University of Warwick, and a superconducting quantum interference device (SQUID) operated by our collaborators at Ciudad Real, Spain. These analysis methods give vital information on the magnetic nature of our nanoparticles through the measurement of M-H curves (see *Chapter 3: Magnetic Nanoparticle Theory and Medical Applications*). From these, values of saturation magnetisation and information relating to the specific nanoparticle magnetism (e.g whether the nanoparticles display superparamagnetic or blocking behaviour). Further information on all of these measurements are explained in detail in the following chapters, *Chapter 2: Experimental Methods*, and *Chapter 3: Magnetic Nanoparticle Theory and Medical Applications*.

Lastly, novel measurements made with a custom-built device by our collaborator at the Institut national des sciences appliquées de Toulouse (INSA), allows for the nanoparticles to be stimulated by an externally applied alternating magnetic field, and the resulting temperature increase measured by means of an infra-red camera. Further details of this instrument are included in *Chapter 2: Experimental Methods*.

The structure of this thesis is as follows: the second chapter (*Chapter 2: Experimental Methods*) details the experimental equipment used to synthesise and analyse the nanoparticles created in this project. This includes a detailed explanation of the (ultra-high vacuum compatible) system responsible for the synthesis of the nanoparticles, known as SLUMPS. Also included are details of the sputtering system used to produce the nanoparticles, and the method used for producing core-shell nanoparticles. The electron microscopes and magnetometers used to analyse our sample are also explained within this chapter. Further to this, a section on the calibration of the core-shell evaporator is included, which allowed a more accurate determination of the temperatures to which the nanoparticles are subjected.

The third chapter (*Chapter 3: Magnetic Nanoparticle Theory and Medical Applications*) includes all the relevant theory for the project. This chapter covers some basic magnetism, the mechanisms of magnetic nanoparticle hyperthermia (MNH), magnetic resonance

imaging (MRI), and magnetic particle imaging (MPI). This chapter explains in full detail what exactly is required from our nanoparticles so that they may perform to their full potential.

The three following chapters relate to the core-shell nanoparticle systems that we have created and studied. Firstly, *Chapter 4: Pure Fe Studies* discusses the pure Fe nanoparticle samples and investigations into how their shape affects the overall magnetic properties of the particles, with detailed size and shape distributions presented. This is achieved through heating the nanoparticles as they pass through the core-shell evaporator, without any shell material present, and the data stems from TEM imaging as well as magnetometry measurements.

Chapter 5: Fe@Cu Studies presents TEM, EDX and magnetometry data on Fe@Cu nanoparticles. Extensive analysis of the size, shape, composition, and magnetic properties of these nanoparticles is detailed. Although not biocompatible, a copper shell has the potential to protect the iron core from oxidation. Another biocompatible shell can then be added to ensure the nanoparticles' safety in patients.

Chapter 6: Other Core Shell Studies details other systems created within SLUMPS, such as Fe@Ag, and investigations into producing nanoparticles with a smaller diameter. Experimentally, this focussed on removing the water cooling to the sputter head, which was thought from previous work to produce smaller nanoparticles. As described in *Chapter 3: Magnetic Nanoparticle Theory and Medical Applications*, smaller nanoparticles behave as superparamagnetically and superparamagnetic nanoparticles are more suited for MRI contrast agents and for magnetic particle imaging (two medical applications targeted in this thesis).

Finally, chapter 7 (*Chapter 7: Conclusions*) summarises the main findings of this project and puts forward some suggestions for further work in this exciting field of research.

Chapter 2: Experimental Methods

1. Introduction

This chapter details the equipment used for the synthesis of nanoparticles investigated in this thesis (see section 2. *Equipment*); specifically, information on our ultra-high vacuum chamber set-up, the method of creating core shell nanoparticles and on the deposition techniques. Included are also descriptions of the techniques used to analyse our nanoparticles; magnetometry, electron microscopy, and specialised heating tests. A calibration of the shell evaporator is also detailed in section 3. *Calibration of the Core Shell Evaporator*, whereby accurate temperature measurements are investigated.

2. Equipment

2.1 Introduction

This section describes the equipment and techniques used for the synthesis and characterisation of our iron nanoparticles. The nanoparticles are produced in ultra-high vacuum (UHV) conditions with a sputter gas aggregation cluster source known as SLUMPS (Sputter Leicester University Mesoscopic Particle Source). The nanoparticles were observed in transmission electron microscopy (TEM) at the University of Leicester's JEOL 2100 TEM and also the JEOL 2200 TEM at the University of York. Heating tests were carried out by our collaborators at Institut national des sciences appliquées de Toulouse (generally referred to as INSA Toulouse) with a magnetic field generator and an infrared camera. Descriptions of the superconducting quantum interference device (SQUID) magnetometer in Ciudad Real, Spain, and vibrating sample magnetometer (VSM) at the University of Warwick, used in this work, have also been included here.

2.2 SLUMPS

Figure 1 shows the layout of our cluster source, SLUMPS. SLUMPS comprises of four main chambers: cluster production, inter aperture, core shell and sample deposition.

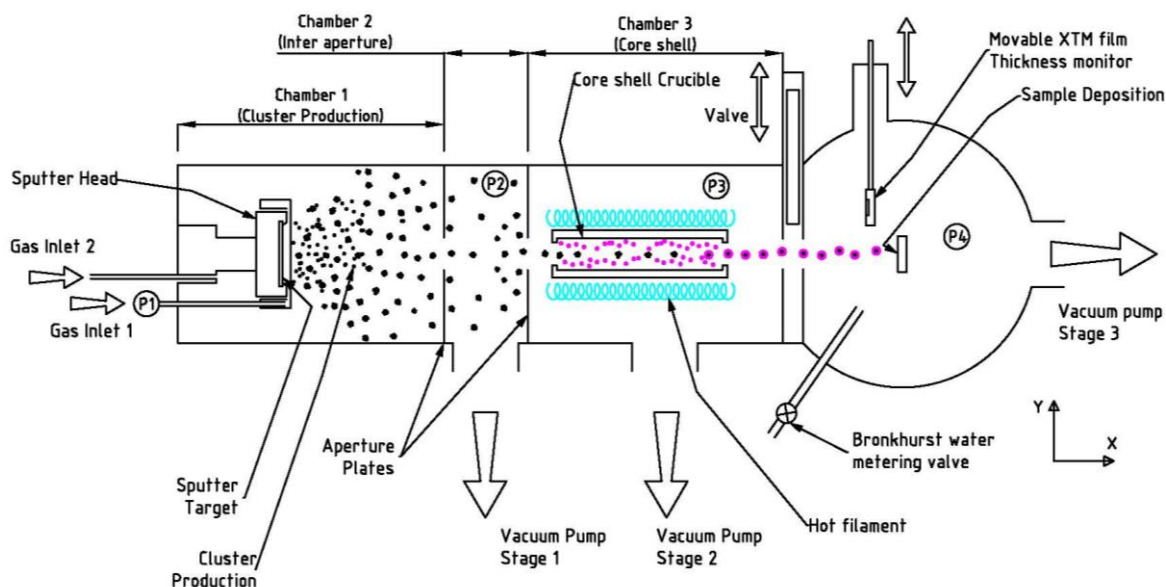


Figure 1 - Schematic of the UHV sputter source, SLUMPS.

SLUMPS has a base pressure of at $\sim 2 \times 10^{-9}$ mbar or lower. This is achieved with characteristic baking of the whole system over a minimum of two days. The pressure gauges, P₁, P₂, P₃ and P₄ are used to set up the system for cluster production by indicating the amount of Ar flowing throughout the system – the importance of Ar is explained in the following sections, 2.3 *DC Magnetron Sputtering* and 2.4 *Gas Aggregation*. P₁ is a pirani gauge and is located behind the leak valve of one of the Ar gas inlets outside the first chamber. P₂ is Penning gauge but is not currently installed. The other two are ion gauges and are located in the other two chambers as shown in Figure 1. The values of P₁ should not be taken as the real pressure present in the first chamber, rather a value for comparative use.

There are three turbo molecular pumps (Edward STPA 1303C) backed by three scroll pumps (Edward XDS35i) attached to SLUMPS which maintain UHV conditions and also create a pressure gradient when the source is running, aiding cluster movement through the system; this is differential pumping. The clusters are produced through sputtering and

gas aggregation methods and use an NCU 200 DC magnetron sputter source from Oxford Applied Research Ltd.

The clusters pass through a shell evaporator (details in section 2.5) allowing a shell of chosen material and thickness to be attached, and the clusters are then deposited on a substrate of choice in the deposition chamber. The nanoparticles can also be deposited into water as water vapour can be introduced through the needle valve labelled in Figure 1. The water vapour is aimed at a liquid nitrogen cooled hollow tube allowing the formation of an ice matrix. The nanoparticles then embed themselves into this ice matrix which is removed from the UHV environment and allowed to melt (Binns, et al., 2012). As mentioned previously, Binns, et al., (2012) indicated that there should be no deformation of the nanoparticles when they impact into the ice matrix, nor should there be any melting of the ice structure (confirmed by experiments).

A crystal thickness monitor (XTM) is installed to measure the deposition rate of the Fe nanoparticles and other materials used in sample production. The piezoelectric effect is employed to estimate the film thickness on a quartz crystal by measuring its oscillation frequency during the deposition. An AC signal induces oscillations whose frequency is affected by the mass of the material deposited on the crystal, and thus the deposition rate can be inferred. The thickness of the material deposited on the crystal is obtained from the density of said material and the ratio of acoustic impedance of the material to that of the quartz crystal (Milton, 2001).

The values recorded from the XTM are used to produce estimates of the mass of iron within magnetometry samples in this thesis. Comparing the XTM values to the number of nanoparticles per unit area within the Transmission Electron Microscope (TEM) images, it is estimated the error on this mass calculation to be of the order 10% (see section 2.8 of this chapter for more information on TEM).

2.3 DC Magnetron Sputtering

In the first chamber, cluster production, the nanoparticles are produced through the sputtering process with an NCU 200 nanocluster source (Oxford Applied Research). This is achieved through an exchange of kinetic energy between argon (Ar) ions and a water-

cooled Fe target (\sim purity of 99.8%, diameter 50.88 mm, and thickness 0.5 mm). The Fe target is negatively charged due to an applied DC voltage supply (160 V to 190 V, 8 W to 25 W) between the target (acting as a cathode) and the magnetron cover (the anode) which is located at a distance 0.3 mm from the target. Ar gas is injected in close proximity to the target and is ionized by the free electrons present there. The now positively charged Ar ions are attracted to the negatively charged Fe target and an exchange of kinetic energy/momentum through collisions ejects Fe from the plate. The region close to the target is at super-saturation and the Fe vapour nucleates after cooling through further collisions with Ar gas and eventually forms Fe clusters. An extra Ar gas inlet and the pressure gradient through the system (achieved with differential pumping) forces the Fe clusters to flow through the system. Magnets are present behind the target to trap the plasma near the surface of the target increasing the likelihood of the Ar vapour colliding with the target, thus increasing the sputtering efficiency and flux of nanoparticles.

2.4 Gas Aggregation

Ar is introduced through two inlets near the sputter head; one is positioned directly above the target while the other is placed behind the target. These inlets ensure the plasma required for sputtering (see section 2.3. *DC Magnetron Sputtering*, above) is well maintained and aids the removal of clusters from the aggregation region. The Ar flow is monitored by measuring the pressure at different points throughout the chamber, specifically P_1 and P_3 – their whereabouts are shown in Figure 1.

Following the sputtering process, the atoms have high momentum which makes them unable to form clusters. Repeated collisions with Ar atoms, and other sputtered Fe atoms, reduces their kinetic energy allowing for cluster formation. The heat released from the Fe atoms bonding is removed by Ar atoms. The clusters are forced through the chamber due to the flow of Ar and a pressure gradient - P_1 (\sim 30 mbar) to P_4 (\sim 2×10^{-5} mbar).

2.5 Core Shell Evaporator

To coat the nanoparticles in a shell they are passed through a heated tubular crucible with the shell material on the inside. The shell thickness is controlled by changing the temperature of the shell evaporator (i.e. the vapour pressure). The method works best if the vapour pressure of the core material at the temperature of the shell evaporator is significantly lower than the vapour pressure of the shell material. Otherwise, the Fe clusters may also be vaporised (or at least partially so).

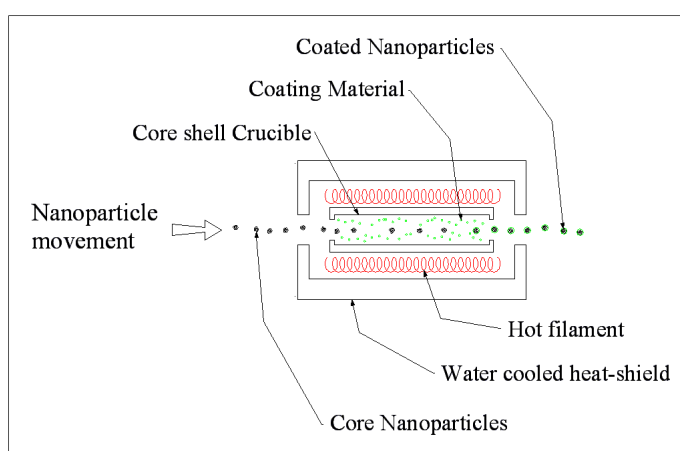


Figure 2 – Schematic of the core shell evaporator.

In these studies, the core shell evaporator is also utilised without any coating material for investigating the effect of temperature on nanoparticle shape (see *Chapter 4: Pure Fe Studies*). In this case, the evaporator is employed as a heating instrument only, without intending to coat the core particle in a shell of another.

The shell evaporator measures 100 mm in length, with an 8 mm diameter alumina crucible through which the nanoparticles pass. This alumina crucible is surrounded by the filament from which a current is supplied to heat the crucible. Outside this there are multiple heat shields to protect the surroundings from the temperatures of the shell evaporator. The shell evaporator runs between 0 and ~ 260 W, with currents up to ~ 6.0 A. Further details on the core shell evaporator can be found in Binns, et al. (2012).

2.6 Thermal Evaporator

Thermal evaporators are used to produce the matrix materials in which Fe nanoparticles are embedded for the heating tests outlined below (section 2.7. *Heating Tests*) and also for magnetometry (see section 2.9. *Magnetometry*). These are in-house built Knudsen cells containing a crucible, thermocouples, and a water cooling system (Binns, et al., 2012). The crucible is loaded with the material of choice and warmed until the material evaporates into an atomic vapour. Here we have used Ag, Ge, and SiO. The beam is aimed at the sample holder and can be co-deposited alongside the sputtered Fe clusters. The evaporator is installed in the final, deposition chamber below the horizontal Fe beam, angled at 45° upwards.

2.7 Heating Tests

The heating tests were carried out by Nicolas Hallali and Julian Carrey at INSA, Toulouse, and used an applied alternating magnetic field (AMF) at 300 kHz, ranging from 10 mT to 80 mT in order to stimulate our magnetic nanoparticles to produce heat. The samples produced for these studies were nanoparticles embedded in a matrix upon a glass substrate (24 mm x 24 mm x 1 mm), with capping and buffer layers of ~ 20 nm to 30 nm. The ratio of iron to matrix material was between 5 and 10% volume filling fraction, to ensure the nanoparticles are appropriately spaced to prevent interparticle interactions. The infrared camera used was a Testo 885 and the magnetic field was setup using a Fives Celes MP 12/400 with a 12 kW power supply. A photograph of the induction coil and sample holder is shown in Figure 3.

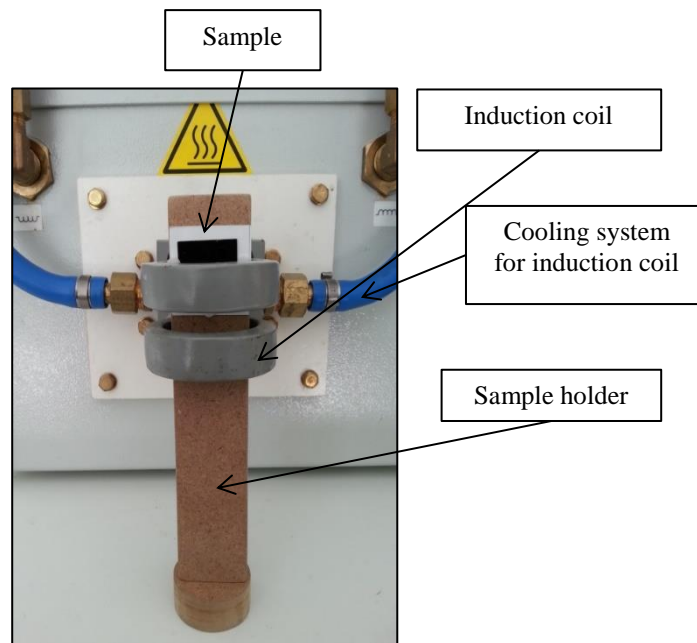


Figure 3 – Photograph of the sample holder and induction coil for the heating tests carried out by INSA, Toulouse.

2.8 Transmission Electron Microscopy (TEM)

2.8.1 TEM

Transmission Electron Microscopy (TEM) is a technique used to characterise samples down to atomic scales. It is utilised in this project for its ability to penetrate the nanoparticles and give information not only on the size/shape, but also the shell and core material. A typical TEM image of our samples is shown in Figure 4 below.

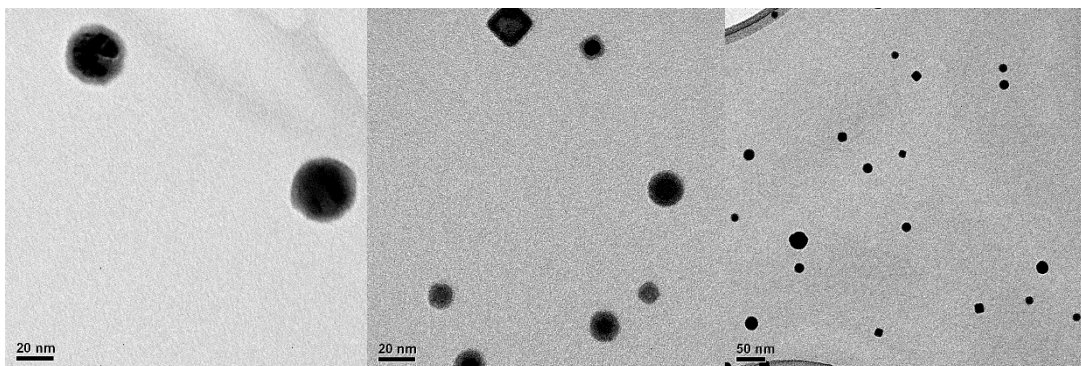


Figure 4- TEM images of the pure Fe nanoparticles. Scale bar for each image shown in bottom left.

There are many interactions that occur when a high energy electron beam is in contact with a sample. They are illustrated in Figure 5 and consideration of these interactions is important to understand the artefacts that may occur within TEM images and

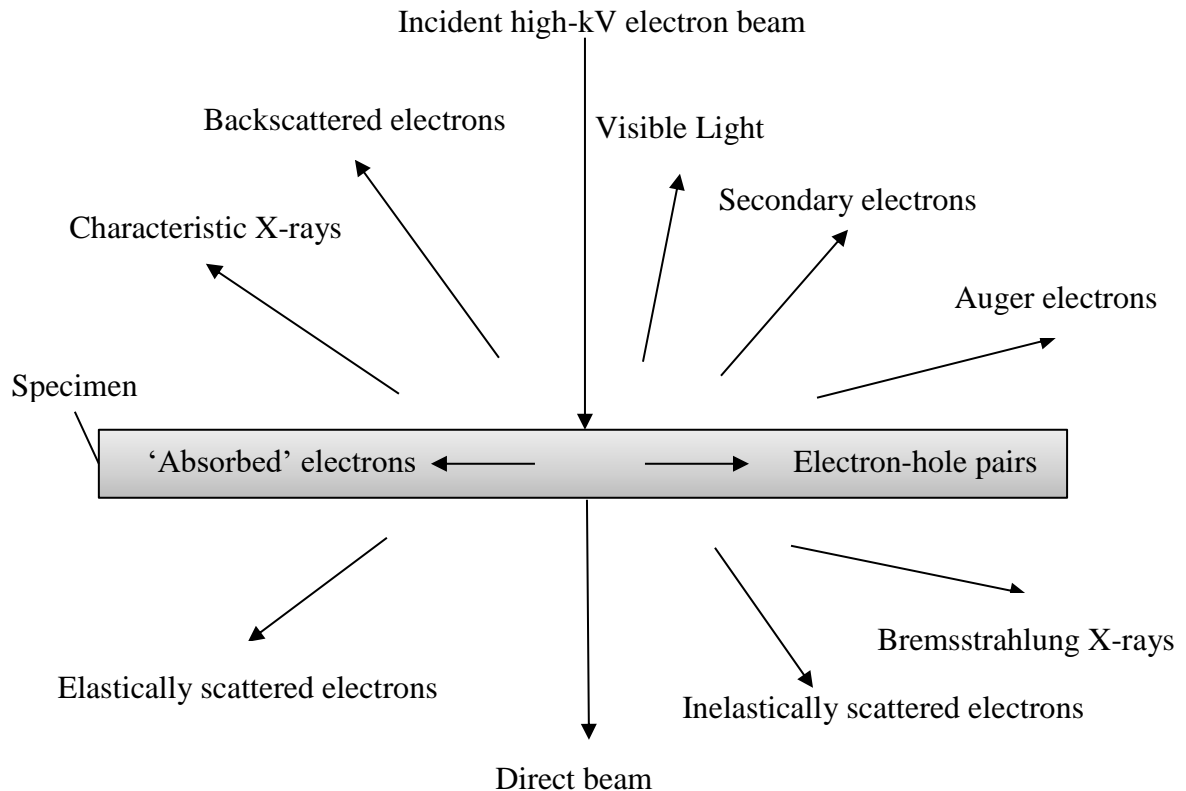


Figure 5 – Some common interactions of a high energy electron beam with a sample.

spectroscopic measurements. These processes are explained in more detail below.

The atom at rest contains ground state electrons bound in discrete energy levels. The incident electron beam may excite an electron in an inner shell and eject it from the atom. This allows for an electron in a higher energy state to fill this hole, releasing energy in the form of an x-ray in the process. This x-ray is characteristic of the energy level difference between the two electrons shells and of the structure of the atom, hence the title that these x-rays are given: characteristic x-rays. Characteristic x-rays are the basis of energy dispersive x-ray spectroscopy (EDX) which is explained further in section 2.8.3.

The process in which an Auger electron is emitted follows on from the emission of a characteristic x-ray. The incident electron ejects an inner-shell electron, and an outer-shell electron transitions into the hole releasing energy. This energy is then absorbed by another outer-shell electron, which is ejected from the atom.

Bremsstrahlung x-rays occur due to an inelastic interaction of the incoming electron with the nucleus. As the electron moves closer to the nucleus, it is decelerated by the coulomb charge field, and emits x-rays of any energy up to the incident beam energy. Other such processes of note are plasmons and phonons. Plasmons are the oscillations of the free electrons in the specimen when an electron from the incident beam. Phonons are similar but relate to the lattice vibrations rather than oscillations of the free electrons. Both of these processes work to warm the sample, giving less focussed images. Sputtering can also occur as surface atoms can be ejected even with an electron beam operating at 100 kV.

Diffraction patterns can also be obtained from electrons passing through a thin crystal. These patterns can be analysed to give information on the crystallography and chemistry of the sample. Different interplanar spacings correspond to specific structures therefore information about the sample structure can be inferred.

As the TEM system allows for high resolution, only a small portion of the specimen may be imaged at any one time. It can be time consuming to continually search through the specimen to obtain enough nanoparticles (in this case) to analyse with enough numbers for appropriate statistics. Secondly, the conclusions made on data from TEM are from 2-D images of 3-D structures – therefore incorrect assumptions can be easily made, especially where shape analysis is concerned. The samples used must also be ‘thin’ enough for electrons to be transmitted. Finally, as the samples in this thesis are magnetic, they can easily affect the lenses and cause the focus to shift and the TEM to become misaligned during imaging.

2.8.2 TEM Design and Alignment

The TEM can be divided into three main sections: the illumination system (the gun and condenser lenses), the objective lens, and the imaging system. The illumination system can be operated in two modes, a parallel beam for use in TEM or a convergent beam for scanning TEM (STEM) mode. For the work in this thesis, only a parallel beam is used as the JEOL 2100 TEM here at Leicester does not have the capabilities to effectively run in STEM mode. Parallel illumination is essential to get the sharpest diffraction patterns and best image contrast.

The objective lens stage is arguably the heart of the TEM. This is where the beam-specimen interactions take place and where dark field and bright field images are created. The better the quality of the image formed by the objective lens the better the resolution of the sample.

Several lenses are utilised in the imaging system for magnification of the image. These can be broken down into the magnification lens and the projection lens (projects the image onto a screen for viewing). Further details on TEM design can be found in (Williams & Carter, 1996).

Aligning the illumination system can be a tedious task and requires much manual effort with tilting the gun, translating the gun, tilting the lenses, centering the apertures and so on and so forth. Without proper alignment the beam will not be focussed and the images will be poor. On average, it takes this user approximately 30 - 40 minutes to align the system to a decent standard. However, as mentioned previously, the magnetic nature of the samples measured in this project can result in the beam becoming misaligned, causing much frustration as the TEM can then require realignment part-way through imaging. This alignment must be repeated per sample but generally a good gun alignment will be semi-acceptable throughout a sitting. This is not to say, however, that the gun does not require further realignment, rather a better alignment than usually found at the start of each session. This then leads to a further 20 or so minutes per sample to ensure the images are in focus and usable.

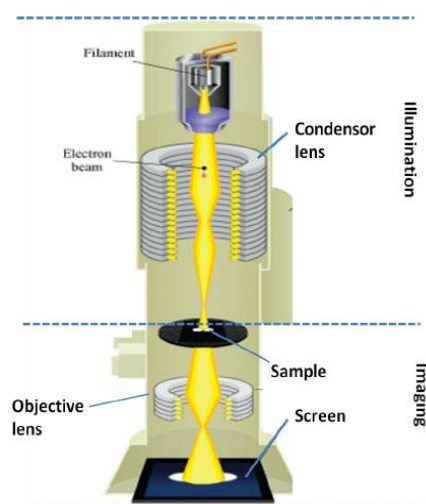


Figure 6 - Schematic of the TEM (Amin, 2012)

2.8.3 Energy-dispersive X-ray Spectroscopy (EDX)

Energy-dispersive X-ray spectroscopy (also commonly shortened to EDX, or EDS) is an analytical technique for the elemental analysis/characterisation of a sample. EDX relies on the characteristic x-rays emitted from a sample when in contact with an incident energy electron beam or a x-ray beam, the former being used here in a TEM environment. These x-rays are characteristic of the elemental composition; therefore the specimen's composition can be inferred from this data.

2.8.4 Sample Preparation

The nanoparticles are created with the sputter source outlined previously. If they are to be heated or coated in a shell, they are passed through the core shell evaporator and then enter the deposition chamber. Here they are deposited onto a TEM grid appropriate to the sample. Usually this is a Cu grid with an amorphous carbon film, but for the Cu coated iron samples (notation: Fe@Cu), the grids used are nickel based so that the only Cu in the EDX signal will be from the Fe@Cu nanoparticles. 2 - 3 Å of material is deposited (using XTM measurements taken before and after the sample is made) as this gives a good coverage of nanoparticles on the grid. Too much material and the nanoparticles tend to stack on top of each other, making measurements more difficult to make, and too little means spending too long searching for enough particles to give enough data for reasonable conclusions and statistics to be applied.

2.9 Magnetometry

As one of the main aims of this work is for the nanoparticles to have high magnetic moments, analysis of the magnetic behaviour is invaluable in assessing their performance. This data will also allow comparisons with nanoparticles in the literature and those that are commercially available to purchase.

Superconducting quantum interference devices (SQUIDs) and vibrating sample magnetometers (VSMs) are utilised in this project to measure the total magnetic moment of our samples. From this and an estimate of the mass of iron in the sample measured

(from various XTM measurements taken throughout the deposition), a value for the moment per gram of Fe can be calculated. This can then be compared with other magnetic nanoparticles in the literature to check whether our nanoparticles have a higher magnetic response and are therefore better equipped for the applications explained in detail in *Chapter 3: Nanoparticle Theory and Medical Applications*. Explanations of the operations of these two magnetometers are given below.

2.9.1 VSM

Vibrating sample magnetometry (VSM) as the name suggests, vibrates the sample to measure its magnetic moment. The sample of interest - the unknown sample - is vibrated perpendicular to the applied field to induce a voltage in the stationary detection coils. From measurements of this voltage one can deduce the magnetic properties of the sample. This is direct application of Faraday's Law.

A second voltage is induced in a similar set of voltage coils with a reference sample (i.e. electromagnetic or a small permanent magnet). The reference sample and the unknown sample are driven by the same machinery, so the phase and amplitude of the induced voltages are directly related.

The known portion of the induced voltage from the reference sample is phased to balance the voltage induced from the unknown sample. This is proportional to the magnetic moment of the sample. This makes the measurements insensitive to changes of vibration amplitude, vibration frequency, small magnetic field instabilities, magnetic field non-uniformity, amplifier gain, or amplifier linearity. However, some VSM designs do not allow for simultaneous measurement of the sample of interest and a reference sample. In this case, the reference sample is often measured before the measurements as a calibration measure and this information is then used for comparison with the sample of interest (Foner, 1959).

The magnetising field is produced by a superconducting magnet which consists of a large number of coils. These must be cooled below its critical temperature to be superconducting which is achieved by liquid helium cooling.

2.9.2 SQUID

A superconducting quantum interference device (SQUID) is a highly sensitive instrument for measuring a magnetic field. It utilises the Josephson Effect and DC SQUIDs house two Josephson junctions connected in parallel.

The Josephson Effect is the phenomenon of a supercurrent where current flows across a junction comprising of two superconductors coupled by a weak link. The weak link can be a thin insulating layer or a physical constriction through which electrons tunnel. If a line of magnetic flux is threaded through a ring of superconducting material, a current is induced in the ring. The magnitude of this induced current is indicative of the flux density and can respond to a change in the field equivalent to fractions of a single quantum unit of magnetic flux ($h/2e$). This is why the SQUID magnetometer is more sensitive than the VSM.

As the magnetic flux in this superconducting loop changes, the critical current of the two junctions oscillates with a period equal to the flux quantum. In other words, the supercurrent rises to a peak as the field is increased, then falls to zero, and then increases again, and so on and so forth. These periodic variations in the current have the same pattern as the interference fringes produced by the diffraction of light.

SQUIDs exploit these periodic variations to measure the current in the superconducting ring and hence measure the ambient magnetic field. In DC SQUIDs, if the two weak links are matched through proper instrumental design, the current in the ring has a DC response to the flux going through it. As these devices are superconducting, the need for coolant is paramount. As in a VSM, liquid helium is used to cool the instrument down to 4 K. This not only allows for lower Johnson noise in readout electronics, but also higher rigidity between gradiometer coils and lower thermal gradients and variations across the superconductors. This is why SQUIDs often seem large when actually, the electronics are rather small (Lenz, 1990).

2.9.3 Sample Preparation

The samples made for the VSM and SQUID were deposited onto silicon substrates of 7 mm × 5 mm and into a matrix of appropriate material such as Ag (diamagnetic). Using

XTM measurements throughout deposition, the overall aim was to produce samples of approximately 100 - 200 nm thickness, with a buffer layer of the matrix material of ~ 20 nm to ensure the nanoparticles definitely stick to the substrate and a capping layer of ~ 50 nm so that they are protected from oxygen and other contaminants after removal from the vacuum chamber. The volume fraction of Fe nanoparticles in the samples was between 5 - 10 %, so as to avoid interparticle effects. The samples are removed from UHV and placed into a gelatine capsule, which was inserted directly into the VSM/SQUID magnetometer for measurement.

3. Calibration of the Shell Evaporator

3.1 Introduction

The shell evaporator, as mentioned previously, is a heated tubular crucible that nanoparticles pass through before they are deposited on a suitable substrate. If there is material employed on the inside of the evaporator, i.e. in the bore, it will vaporise at a temperature specific to that material. For this reason, it is important to know the temperature inside the bore of the evaporator during deposition to ensure the material has vaporised and has the capability to coat the iron nanoparticles passing through. An accurate temperature measurement is also important for the investigation of heat on our Fe nanoparticles' shape, size and magnetic behaviour; see *Chapter 4: Pure Fe Studies* for these investigations.

The thermocouple installed in the core-shell evaporator is placed beside the bore and not inside as it would interfere with the evaporator function by blocking nanoparticle passage. The following data was extracted from experiments to calculate the 'true' temperature that the nanoparticles would be subjected to, that is, inside the bore itself. This was achieved by the introduction of a second thermocouple placed inside the bore, directly in-line with the sputter beam. Three measurements were noted; the temperature of the thermocouple outside the bore, measured by the 'outer thermocouple,' the temperature of the thermocouple inside the bore, measured by the 'inner thermocouple,' and the power supplied to the evaporator. The power was increased to maximum and decreased from maximum (hereby referred to as ramping up and down, respectively) and plots to relate

these three measurements were made. The pressure was kept at what would be typical for our deposition with Argon gas flowing from the sputter end of the chamber. This gives pressures of ~ 30 mbar at P_1 , $\sim 2 \times 10^{-4}$ mbar at P_3 , and $\sim 2 \times 10^{-5}$ mbar at P_4 .

Each time the power was increased, the core shell evaporator is left for 30 minutes for the temperature to stabilise. The power was increased by raising the current supplied to the evaporator in steps of 0.5 A. The voltage was noted at the same time as the temperature measurements for both the inner and outer bore so that the power supplied could be accurately calculated.

3.2 Results and Analysis

The temperature of the two thermocouples, inner and outer, plus the power was recorded to produce graphs to relate the three, for both ramping up and ramping down of the core shell evaporator – this is shown in Figure 7 and Figure 8.

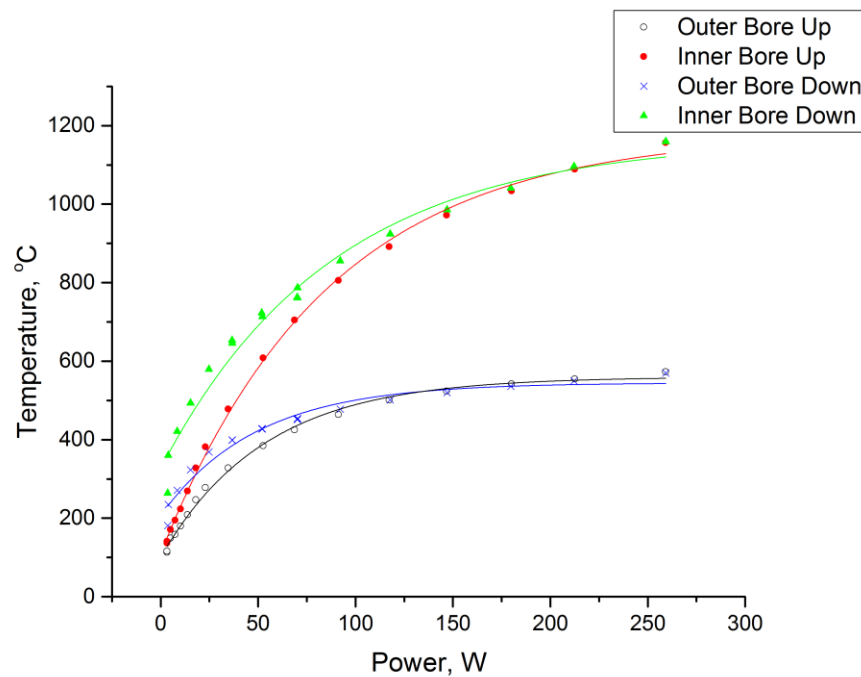


Figure 7 –temperature readings of the inner and outer bore thermocouples whilst ramping up and down in power. Exponential fits are over plotted to each.

The experimental errors on temperature measurements are estimated to be below 5 °C, and on power measurement to be of order 1 W. Their inclusion in Figure 7 blurs the points, and does not add anything to the plot, hence their removal.

The plots in Figure 7 have been fitted with exponentials and the standard errors (one sigma) taken from these to calculate the error. The temperatures quoted from this point onwards are from these exponential fits with the associated error. The exponentials fitted are of the form

$$y = a + be^{cx},$$

with a , b and c varied parameters within the fitting model, applied using the software package Origin.

Figure 8 a) shows the relationship between in the inner bore and outer bore thermocouple temperatures as the power is ramped up and down. Figure 8b) shows the same data but without distinguishing between the directions the power was changed and shows excellent correlation (r-squared values: up = 0.999, down = 0.997, both = 0.997)

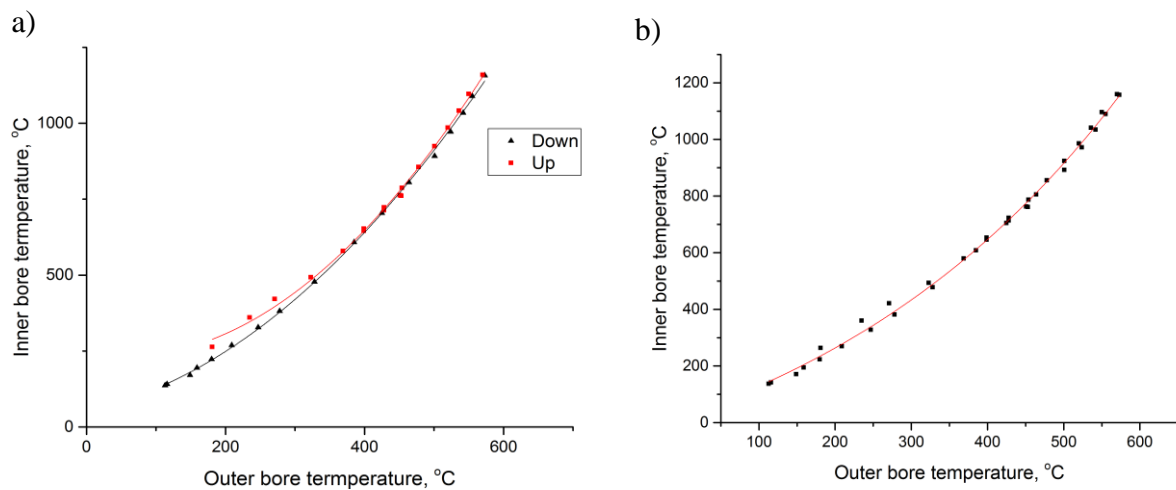


Figure 8 – the relation between the inner and outer bore thermocouple temperature readings. a) splits the data into ramping up and down with individual exponential fits whereas b) has only one exponential over both ramping up and down.

3.3 Conclusions

Figure 7 and Figure 8 show the relationships between the inner and outer bore thermocouple temperatures and the power supplied to the evaporator. They all follow an exponential relationship, clearly illustrating the vast difference in temperature between the outer and inner bore thermocouples, particularly at higher temperatures/powers. This calibration allows for more accurate representation of the temperature inside the bore of the shell evaporator and that the nanoparticles are subjected to.

There is also a clear difference between the ramping up and ramping down of the evaporator as shown by Figure 7, despite the time between measurements being approximately 30 minutes. This shows that the shell evaporator takes longer than 30 minutes for the temperature to stabilise. From this point onwards, the decision was made to always ramp up the power to the evaporator and to ensure the time between sample creations to be approximately 30 minutes to give the same reliable temperatures as was investigated here.

The decision to only use the power to infer the inner bore temperature was also influenced by the unreliability of the outer bore thermocouple during sample synthesis. Quite often the wires would overlap at an earlier point, thus measuring the temperature at a different place than in the outer bore, or the thermocouple would fail entirely. This was unavoidable due to the experimental set-up. For consistency, the power-inner bore thermocouple temperature relationship was used to estimate the temperature the material in the shell evaporator, and the temperature of the iron nanoparticles are subjected to – see Figure 9.

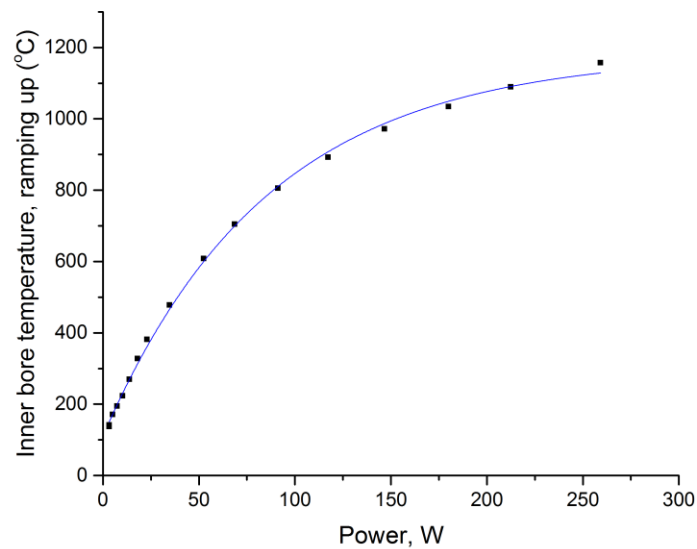


Figure 9 – the inner bore thermocouple temperature readings whilst the power is ramped up.

The difference in the ramping up or down of the power is less important when comparing the two thermocouple temperatures, as indicated by Figure 8, and the regression correlation value is 0.997 for this line across both ramping up and down. This is due to power to temperature lag, rather than a thermocouple discrepancy.

The error assumed from the thermocouple measurements is of the order 5 °C which is far less than we expect the temperature variation to be throughout the core-shell evaporator. It has been noticed in previous experimental work and in preliminary testing that the material inside the shell evaporator can gather at the ends of the bore. Sometimes this material can block the bore completely at either end. However, to quantify this temperature variance, the introduction of multiple thermocouples throughout the shell evaporator is required so that the temperatures across the bore can be measured and investigated – a tedious and not particularly insightful endeavour.

The errors on temperature taken from power measurements using Figure 8 are approximately 44 °C. This is an acceptable error when one considers that 15 measurements were taken over a range of ~ 1200 °C.

All further temperature values quoted in this thesis originate from the exponential fitting in Figure 8 and its associated error.

Chapter 3: Magnetic Nanoparticle Theory and Medical Applications

1. Introduction

In this chapter, the relevant nanoparticle theory is discussed with particular emphasis on the magnetic properties of single and multi-domain nanoparticles, and how they react when exposed to magnetic fields. Details on how they can be manipulated for magnetic nanoparticle hyperthermia, magnetic resonance imaging contrast agents and in a new tool, magnetic particle imaging, will also be explained here. Understanding the workings of these systems is important if the nanoparticle performance is to be optimised.

There are three ‘types’ of magnetic nanoparticle that are important for the above applications and these types can be selected through material choice, size, shape, temperature and other environmental factors (Atkas, et al., 2015). The size of the nanoparticle generally dictates whether the system is single- or multi-domain; the spins align in a single direction, or in regions of more than one particular alignment. This causes significant changes in the magnetic properties of the nanoparticle. The shape can have interesting effects on the canting of the surface spins, and when there are ~10% of atoms on the surface, their direction has a significant impact on the nanoparticle’s behaviour as a whole. Temperature can cause some particles to behave in a differing magnetic manner, i.e. at the macroscopic scale the Curie temperature dictates whether the material behaves as a ferromagnet or a paramagnet. A similar effect is observed for superparamagnetic nanoparticles in their Néel relaxation time. These effects are detailed in the following sections. Some other environmental factors, for example pressure, also impact the nanoparticle characteristics.

Some of these parameters can be easily manipulated and altered in our gas phase production of nanoparticles and are investigated thoroughly in the following data chapters. This chapter, however, serves to explain the significance of such characteristics in terms of their targeted application.

2. Basic Magnetism

2.1 Introduction

The behaviour of magnetic materials can be classified with a number of magnetic parameters, which are detailed in this section. Some materials are permanent magnets (ferromagnetic), whereas some are attracted to magnetic fields (paramagnetic), and others are repelled (diamagnetic). There are also other more complicated relationships such as antiferromagnetism and superparamagnetism. Each of these types of magnetism is, in part, related to the magnetic moments within the material and, sometimes, materials can display one or more type due to the environment in which they are subjected (i.e. temperature, pressure).

When a magnetic material is exposed to a magnetic field of strength, \mathbf{H} , the magnetic induction, \mathbf{B} , is given by,

$$\mathbf{B} = \mu_0 (\mathbf{H} + \mathbf{M}), \quad (1)$$

where μ_0 is the permeability of free space, \mathbf{M} is the magnetisation or the magnetic moment per unit volume where $\mathbf{M} = \mathbf{m}N/V$, with \mathbf{m} the atomic magnetic moment and N/V the number of atoms per unit volume.

To distinguish at small magnetic fields between different types of magnetic materials, the magnetic susceptibility, χ is used,

$$\mathbf{M} = \chi \mathbf{H}, \quad (2)$$

which describes the relationship between the magnetic field applied, \mathbf{H} , and the induced magnetisation, \mathbf{M} .

The magnetism in materials is due to the magnetic moments of the electrons, which originates from their orbital motion and their intrinsic spin momentum. To explain the contribution from their orbital motion, the electrons can be pictured classically as orbiting the nucleus in a circular orbit. If the electron is at a radius r from the nucleus and travelling at a velocity \mathbf{v} , then the current \mathbf{I} is,

$$|I| = \frac{e|\mathbf{v}|}{2\pi r}, \quad (3)$$

where e is the electron charge. The magnet moment $\boldsymbol{\mu}_L$ is given by,

$$|\boldsymbol{\mu}_L| = |I|\pi r^2, \quad (4)$$

and so it follows that the magnetic moment can be rewritten as,

$$|\boldsymbol{\mu}_L| = \frac{e|\mathbf{v}|}{2\pi r} \cdot \pi r^2 = \frac{e|\mathbf{v}|r}{2}. \quad (5)$$

As the angular momentum of the electron can be represented by $|\mathbf{L}| = m|\mathbf{v}|r$, equation (5) can be rewritten as,

$$|\boldsymbol{\mu}_L| = \frac{e|\mathbf{L}|}{2m}. \quad (6)$$

Or, alternatively,

$$\boldsymbol{\mu}_L = -\frac{e}{2m}\mathbf{L}. \quad (7)$$

Even though this has been derived from classical physics, it follows from quantum mechanics that the angular momentum is quantised, so the magnetic moment (due to orbital motion) must also be quantised. As mentioned previously, the electrons' intrinsic spin also contributes to the overall magnetic moment of the atom. The magnetic moment due to spin angular momentum, denoted with an \mathbf{S} , is

$$\boldsymbol{\mu}_S = -\frac{e}{m}\mathbf{S}, \quad (8)$$

where the e/m component emerges from Dirac's relativistic theory of electrons and is a result of Thomas precession. As with the orbital angular momentum, the spin angular momentum must also be quantised.

The solution of Schrödinger's equation in the radial potential of an atomic nucleus gives three quantum numbers: the principle quantum number n , the angular momentum number

l , and the magnetic quantum number m_l . These quantum numbers can only take particular values: $n = 1, 2, 3, \dots, \infty$; $l = 0, 1, \dots, n - 1$; $m_l = -l, -(l - 1), \dots, 0, \dots, (l - 1), l$. Dirac theory also gives another spin quantum number, m_s which can only take values of $\pm 1/2$. Due to the Pauli exclusion principle, each electron in the atom must have a unique set of values for these quantum numbers.

The magnetic moment of the multi-electron atom is the combination of the individual moments from each electron and gives a total orbital angular momentum quantum number L ,

$$|L| = \sqrt{L(L + 1)} \hbar, \quad (9)$$

and a total spin angular momentum quantum number S ,

$$|S| = \sqrt{S(S + 1)} \hbar, \quad (10)$$

where \hbar is the reduced Planck's constant. The values of L and S are found by adding together the individual m_s and m_l values. It therefore follows that filled shells give values of m_s and m_l that make L and S equate to zero, meaning they do not contribute to the overall magnetic moment of the atom. Only partially filled outermost shells of the atom actually contribute to the magnetic moment of the atom. This is reason that iron is so magnetic; iron has the most unpaired electrons of any pure element. To calculate the total angular momentum quantum number of the atom (denoted with J), one must add the L and S quantum numbers as appropriate according to Hund's rules (Softley, 1999). The total angular momentum, J , can be calculated in a similar manner as equations (9) and (10) using,

$$|J| = \sqrt{J(J + 1)} \hbar. \quad (11)$$

The total atomic moment, $|\mu|$ of an atom is related to J by,

$$|\mu| = g \mu_B J, \quad (12)$$

where g is the Landé g -factor and is given by,

$$g = \frac{3}{2} + \frac{S(S+1) - L(L+1)}{2J(J+1)}$$

(13)

(Softley, 1999).

The application of an applied magnetic field can distort the electron orbits and produce a field in opposition to the applied field. This response to the magnetic field is diamagnetic and is usually very weak. If the atom possesses a permanent magnetic moment, the diamagnetic component will be orders of magnitude lower than the paramagnetic susceptibility. Therefore, atomic diamagnetism only significantly affects the overall magnetism of the atom if the atom has no permanent magnetic moment, i.e. rare gases. The magnetic nanoparticles synthesised in this project are not rare gases, and so further information into diamagnetic theory is omitted.

When matter is placed in a magnetic field, the magnetic moment in the atom tends to align with the applied field if the material is paramagnetic. After the magnetic field is removed, however, the net magnetisation of the sample returns to zero. This is due to atomic (non-zero) moments being randomly orientated within a paramagnetic material until the introduction of a magnetic field forces their alignment. Once the magnetic field is removed, they return to a disordered, non-magnetic state. Paramagnetic materials therefore have a positive susceptibility due to this small positive attraction to magnetic fields.

The susceptibility, χ , of paramagnetic materials is also affected by temperature,

$$\chi = \frac{C}{T},$$

(14)

meaning the magnetisation can be rewritten as,

$$\mathbf{M} = \frac{\mathbf{H}}{T} \cdot C,$$

(15)

where C is a constant known as the Curie constant. (Curie, 1895)

Unreservedly, the most important, or rather, the most useful, magnetic material class is the ferromagnet. Due to their high permeabilities, high magnetic inductions are possible even with a reasonably low magnetic field. They have the ability to retain their magnetisation and therefore can act as a source of magnetic field and they can also be

used in electric motors through the torque on a magnetic dipole. As we will see further in this chapter, ferromagnetic materials also have the ability to behave as a superparamagnet at the nanoscale with interesting and useful behaviours. Ferromagnets are interesting magnetically because their total atomic moments are nonzero. Moreover, their atomic moments are strongly aligned with one another due to the exchange interaction.

The Curie temperature represents the point at which the magnetic behaviour of ferromagnetic material changes. Above the Curie temperature the material behaves paramagnetically whereas below the Curie temperature, ordered ferromagnetic behaviour exists with aligned magnetic domains (see 2.2 *Magnetic Domains* for more information). As the temperature applied to the ferromagnetic material is raised, the thermal energy increases. Above the critical Curie temperature, the randomising effect of thermal energy overcomes the exchange energy giving rise to disordered magnetic moments and a paramagnetic nature.

2.2 Magnetic Domains

If no domain structure existed within a magnetic material, its ‘magnetic self-energy’ would be indefinitely high. The inter-atomic alignment is due to a quantum mechanical interaction known as the exchange interaction or exchange force. This energy has no real roots in magnetism, but it is effectively a correction to the Coulomb energy required by quantum mechanics. It does, however, provide a large difference in energy between parallel and anti-parallel alignment of neighbouring spin moments. This exchange interaction is orders of magnitude higher than the magnetic dipolar interactions and is therefore the source of ferromagnetism.

If the atomic spins obey the exchange interaction, they align with the field in such a manner to produce the maximum magnetic energy. As the dipolar interaction is long range and the exchange interaction only operates between atomic neighbours, there is of course a compromise that will minimise the energy relative to the total magnetised state. That is to say the exchange interaction and the magnetic self-energy compete. If the material organises its magnetisation into domains of opposite magnetisation, the magnetic self-energy will be reduced in comparison to a state of uniform magnetisation. For example, Figure 10 shows the formation of domains within a cube. Part a) shows the

cube uniformly magnetised and its magnetic self-energy is reduced by a factor of $1/N$ when divided into N domains of opposite magnetisation (see Figure 10 b)). Figure 10 c) shows the domain structure to reduce the external field to zero. In a single-domain material, as with Figure 10 a), the majority of the magnetic energy is contained in volume around the magnetised body, whereas when this is increased, the magnetic energy is reduced due to the short distance the magnetic field has to cover. A multi-domain structure gives the minimum magnetic energy state as all the magnetic field is contained within the ferromagnetic.

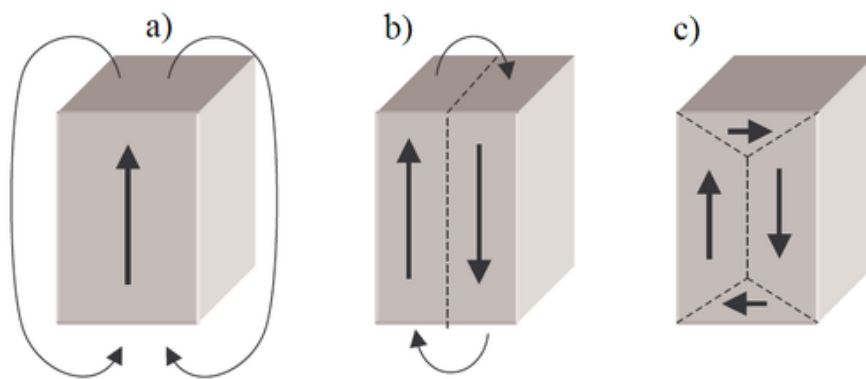


Figure 10 - Simplistic illustration of domain structure and magnetic energy. From (Zureks, 2008)

Forming as many domains as possible serves to minimise the magnetic self-energy. However, the introduction of another domain adds another domain boundary ultimately increasing the exchange energy within the material. Eventually, it becomes energetically unfavourable to increase the number of domains because of the extra exchange energy these boundaries would add. Actually, an abrupt boundary between domains would not work energetically as this would lead to a high exchange energy. The exchange energy can be reduced by spreading their direction over many atomic spins.

2.3 Magnetising a sample

Applying a low enough magnetic field to a sample with multiple domains aligns them with the applied field. The domains with the closest magnetisation directions to the applied field grow in size at the expense of the domains which are the least aligned. However, as this process is not the only one present, reversible domain wall motion will

only occur for small applied fields. For larger applied fields, there is irreversible domain wall motion meaning removing the field will not return the overall magnetisation of the sample to zero. This retained magnetisation is known as remnant magnetisation, thus hysteresis is observed.

Figure 11 shows a generic M-H/hysteresis plot for a normal magnetic material. The applied magnetic field is increased until the magnetisation of the material reaches its maximum, its saturation magnetisation M_S . At this point all spins are aligned with the magnetic field and increasing the field further cannot influence the system; the system is saturated. When the applied magnetic field is decreased and reversed, often the magnetisation of the sample is retained. This is due to remnant magnetisation, M_r , and indicates the coercive field, H_C , of the sample. It is this coercivity that gives rise to the hysteresis loops found in M-H curves of some magnetic systems. The area of said hysteresis loops is proportional to energy losses, and can lead to heating – an extremely useful consequence, and is the basis of magnetic nanoparticle hyperthermia (see section 4. *Magnetic Nanoparticle Hyperthermia*).

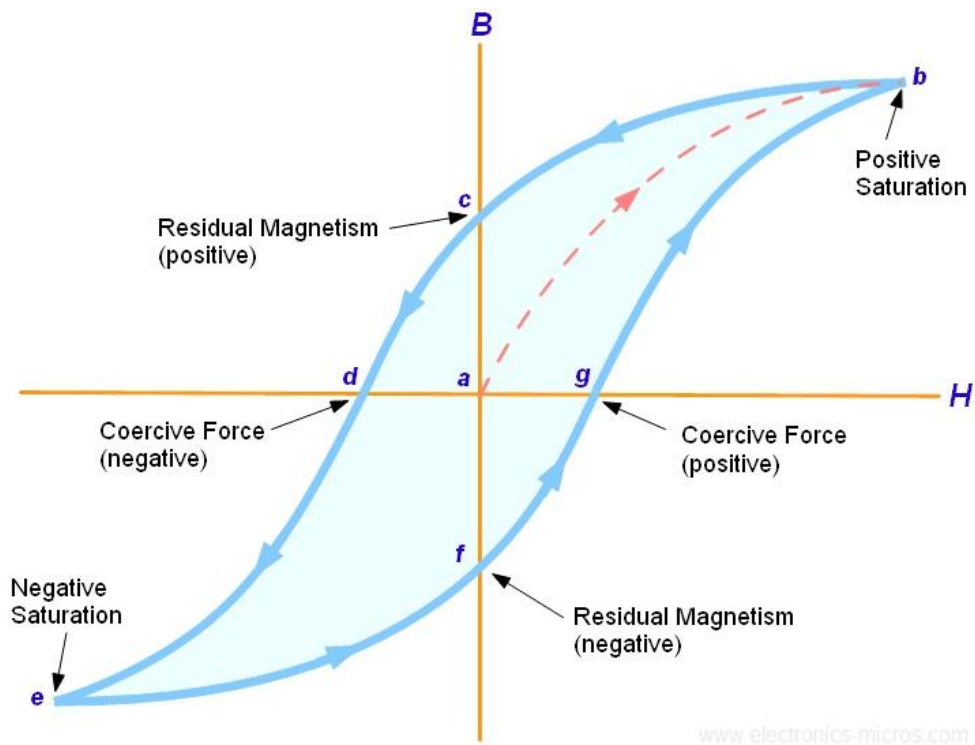


Figure 11 – A generic M-H plot illustrating hysteresis, magnetisation saturation, residual magnetism and coercivity (coercive force). (Electronics-micros, 2017)

3. Superparamagnetic behaviour

Arguably, one of the main factors affecting a nanoparticle's magnetic behaviour is its size. This is due to the large proportion of the atoms located at the surface and also attributed to the domain structure of the nanoparticle. At the macroscopic scale, all magnetic materials are formed of multiple domains, whereby large groups of electron spins are orientated in multiple directions. At the nanoscale however, due to the sizing, some have very few domains, and when small enough, are single-domain. This is due to the fact that there is clearly a minimum volume required for the process of creating more domain boundaries to minimise the magnetic self-energy. This means at a small enough volume, it is energetically favourable to have a single-domain sample.

Single-domain magnetic nanoparticles exhibit superparamagnetism. The size of superparamagnetic nanoparticles tends to be between a few nanometers and tens of nanometers in diameter, dependant on the environment and the nanoparticle material. The measurement time also influences the magnetic property of the nanoparticle as will be explained in more detail in this section. In a single-domain, the majority of the magnetic energy is contained in volume around the magnetised body, whereas when this is increased to two domain structures, the magnetic energy is reduced due to the short distance the magnetic field has to cover.

In ferromagnetic systems, the Curie point splits the ferromagnetic and the paramagnetic regimes. In a superparamagnet, a similar switching point is dictated by the Néel relaxation time, τ_N . If the material has uniaxial magnetic anisotropy, the energy is minimised if the magnetic moment is in one of two orientations, 180° apart. The Néel relaxation time is the average time period it takes for the nanoparticle's magnetization to randomly flip due to thermal fluctuations,

$$\tau_N = \tau_0 \exp\left(\frac{\Delta E}{k_B T}\right), \quad (16)$$

where τ_0 is the pre-exponential factor (of order 10^{-9} - 10^{-11} s) and is very weakly dependant on temperature, $k_B T$ is the thermal energy, and ΔE is the anisotropy energy barrier (Bahadur & Giri, 2003; Hergt, et al., 1998; Pankhurst, Connolly, Jones, & Dobson, 2003) The energy barrier ΔE is given by $KV\sin^2\theta$ where K is the anisotropy energy density, V is the volume of the particle and θ is the angle between the magnetisation

direction and the anisotropy axis (Binns, 2010; Pankhurst, Connolly, Jones, & Dobson, 2003). The $\sin^2\theta$ dependence illustrates the two minimum energy orientations the magnetic moment can reside in, 0 and π radians, with respect to the anisotropy axis. Therefore, an energy barrier of magnitude of KV has to be overcome in order for the magnetisation to be flipped. Therefore equation (16) can be rewritten as,

$$\tau_N = \tau_0 \exp\left(\frac{KV\left(1 - \frac{H}{H_K}\right)^2}{k_B T}\right), \quad (17)$$

where H is the applied field and H_K the anisotropy field. This time constant, τ_N , is known as the Néel relaxation of the superparamagnetic particle and is unique for each material. As the energy barrier is of a similar order to the thermal energy of the nanoparticle the relaxation time is very small, causing the net magnetisation of a superparamagnetic nanoparticle to equate to zero when the observation time is longer than the Néel relaxation time.

Alongside Néel relaxation, Brownian relaxation plays a part in magnetic nanoparticle hyperthermia as the nanoparticles are required to be in hydrosol suspensions for injection;

$$\tau_B = \frac{3 V_H \eta}{k_B T}, \quad (18)$$

where V_H is the hydrodynamic volume (i.e. the volume of the particle in solution) and η the viscosity. The combined relaxation time is given by

$$\tau = \frac{\tau_N \tau_B}{\tau_N + \tau_B}. \quad (19)$$

The application of a magnetic field to a superparamagnetic nanoparticle induces the particle moments to align with the direction of the magnetic field. However, thermal fluctuations prevent them all from aligning immediately but is overcome by an increase in magnetic field. Eventually they become saturated. Superparamagnetic nanoparticles do not exhibit hysteresis meaning the spins are free to orientate in any orientation when the field is removed due to thermal energy. This demagnetises the system leaving a sigmoidal but non-coercive M-H curve as is illustrated in Figure 12.

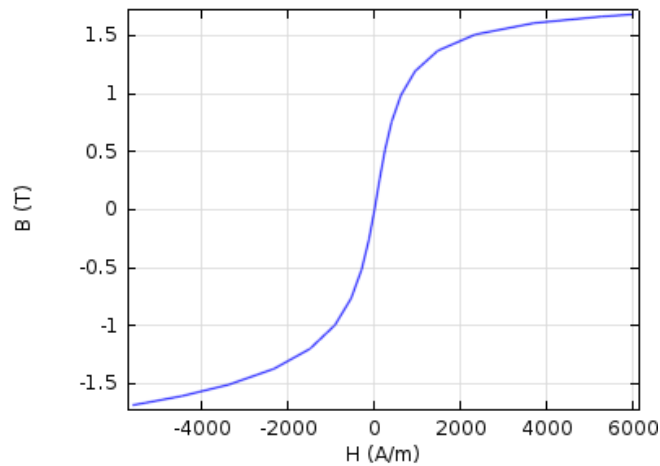


Figure 12 – Typical B-H curve of a superparamagnetic material.

At lower temperatures, the nanoparticles are no longer free to rotate when the field is removed and will align along their anisotropy axis in the direction nearest that of the applied field. They become 'blocked,' giving rise to coercivity and hysteresis. This temperature is known as the 'blocking temperature' and can be obtained by the rearrangement of equation (19). Below this temperature, the nanoparticles exhibit ferromagnetic behaviour.

Above single domain sizes, the nanoparticle is multi-domain and therefore does not exhibit superparamagnetic behaviour, rather they exhibit hysteresis loops (as described in section 2.3). If the size is increased further, the nanoparticles will not produce heat through superparamagnetic behaviour or through hysteresis heating, only through friction with the surroundings via Brownian motion as the magnetic field has the potential to physically rotate the entire nanoparticle.

4. Magnetic Nanoparticle Hyperthermia

4.1 Introduction

Magnetic nanoparticle hyperthermia (MNH) offers the potential for a targeted therapy for tumours and other unwanted masses in the body. This is an attractive alternative for cancer patients as current treatment plans including surgery, chemotherapy, and radiotherapy, for example, are unfortunately riddled with side-effects. This is due to the non-targeting nature of these therapies and due to the body's own immune system failing to recognise the difference between healthy cells and those that are cancerous. Chemotherapy works to kill the cancerous cells through disrupting the DNA synthesis, cell division, and through the prevention of cellular growth. This is achieved using drugs which affect not only the cancerous cells, but also healthy ones. Radiotherapy utilises high energy X-rays in order to break DNA strands through free-radical formation (King & Robins, 2006). Although this can be targeted somewhat more than with chemotherapy, the radiation causes adverse reactions to tissue located nearby. Surgery has very obvious side effects associated with anaesthetic and trauma due to incision of soft tissues. To produce a novel therapy with minimal side-effects would revolutionise the treatment of cancer. MNH has this potential.

MNH utilises the magnetic properties of nanoparticles to heat living tissue. Heating cells to 43 °C denatures their proteins and causes their membranes to become permeable, ultimately resulting in cell death. Controlling nanoparticle positioning allows for only a small selected area of the patient/body to be affected by the treatment, thus drastically reducing the side-effects that the patient is exposed to. The addition of molecules with the capacity of targeting specific cell-types also allows for location and treatment of otherwise unknown cancers in the body; a vital tool for discovering metastasised tumours.

There are three mechanisms responsible for nanoparticle heating; susceptibility heating, hysteresis heating, and viscous heating. Nanoparticles exhibit superparamagnetism below a critical diameter, d_{sp} , and produce heat through susceptibility heating due to a phase lag between the applied field and sample magnetisation. Above this critical diameter, the nanoparticles no longer exhibit superparamagnetism as they are 'blocked' and do not produce heat in this manner. Instead, a hysteresis loop is followed by the magnetisation of the particles when in an oscillating magnetic field, and the energy outputted by these nanoparticles is directly related to the area of the hysteresis loop. At larger diameters,

another critical diameter is met – $d_v(H)$. Above this size, the applied field is unable to flip the magnetisation of the sample but heat can still be produced by stirring as the nanoparticles move in response to the field gradients. These three types of heating are explained in further detail in the following sections and are illustrated in Figure 13 - Susceptibility heating via superparamagnetic nanoparticles, hysteresis heating through blocked nanoparticles and stirring (viscous heating) due to friction, below.

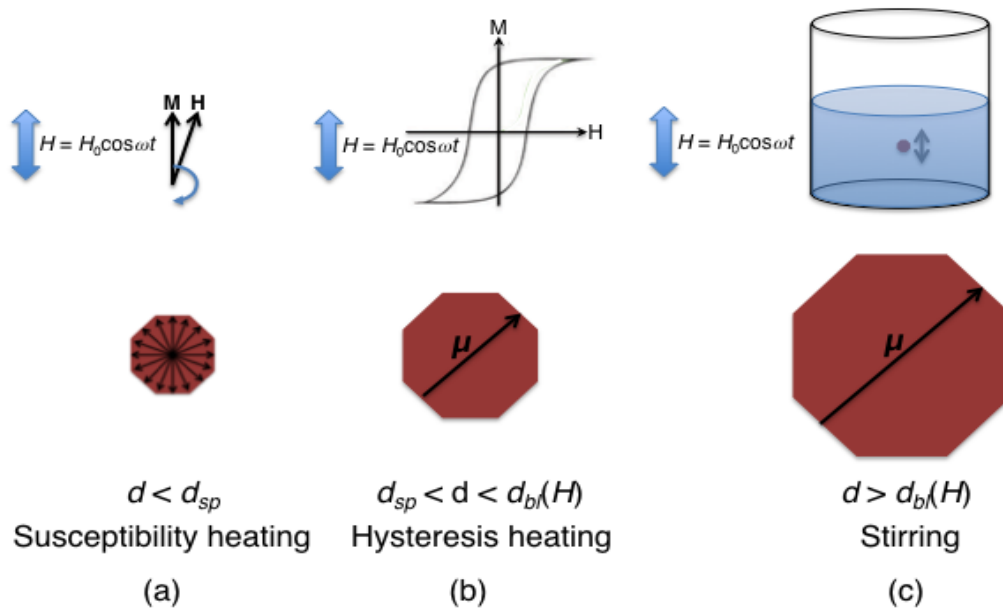


Figure 13 - Susceptibility heating via superparamagnetic nanoparticles, hysteresis heating through blocked nanoparticles and stirring (viscous heating) due to friction with nanoparticle size dependency illustrated for each. Image from (Binns, 2010)

4.2 Superparamagnetic Nanoparticles

Superparamagnetic nanoparticles produce heat due to thermodynamical processes as the anisotropic energy barrier is very small. To calculate the power dissipation through susceptibility heating from superparamagnetic nanoparticles in an alternating magnetic field, the first law of thermodynamics is considered (Rosensweig, 2002; Binns, 2010; Pankhurst Q., 2003; Laurent S., 2011). The first law of thermodynamics states that “the total work is the same in all adiabatic processes between any two equilibrium states having the same kinetic and potential energy” (Sears & Sallinger, 1982); $dU = dQ + dW$ with U representing the internal energy of the system, Q the heat and W the work done on the system. In adiabatic processes, $dQ = 0$ and using $dW = H \cdot dB$, and this then becomes, $dU = H \cdot dB$ or,

$$dU = \mu_0 H. d(H + M), \quad (20)$$

as H and B are always orientated in the same direction and $\mathbf{B} = \mu_0(\mathbf{H} + \mathbf{M})$. From here it is evident the change in the internal energy of the system over one cycle can be expressed as,

$$\Delta U = \mu_0 \int H d(H + M). \quad (21)$$

Integrating and noting the magnetic field intensity over one cycle equates to zero, this equation therefore becomes,

$$\Delta U = \mu_0 \int M dH. \quad (22)$$

Evaluation of the integral above when the magnetisation is lagging behind the field gives a positive change in internal energy over one cycle. This is the reason why heat is produced when an alternating field is applied to superparamagnetic nanoparticles. As H is sinusoidal, then $H(t) = \text{Re}[H_0 \exp\{i\omega t\}]$ where H_0 is a constant, ω is the angular frequency of the applied, field and t is a period of time. As $M = \chi H$ and the ferrofluid magnetic susceptibility (χ) can be expressed in terms of its real and imaginary parts; $\chi = \chi' - i\chi''$ (where the imaginary part of the susceptibility represents the loss). The magnetisation is then given by,

$$\begin{aligned} \mathbf{M} &= \text{Re}[\chi \mathbf{H}] \\ &= H_0 \{\chi' \cos(\omega t) + \chi'' \sin(\omega t)\}. \end{aligned} \quad (23)$$

Combining with $\frac{dH}{dt} = -\omega H_0 \sin(\omega t)$ gives,

$$\begin{aligned} \Delta U &= -\mu_0 H_0^2 \int_0^{\frac{2\pi}{\omega}} (\chi' \cos \omega t + \chi'' \sin \omega t)(\sin \omega t) dt \\ &= \mu_0 \pi H_0^2 \chi'' \end{aligned} \quad (24)$$

Multiplying the change in internal energy per cycle by the frequency, f , of the alternating magnetic field gives the total power dissipated, i.e. $P = f\Delta U = \mu_0\pi f H_0^2 \chi''$ (Hergt R., 1998; Rosensweig, 2002; Pankhurst, 2003; Binns, 2010; Hergt, 2006; Laurent, 2011). The imaginary ferrofluid magnetic susceptibility can be expressed in terms of frequency, ω , and the Néel relaxation time, τ , by,

$$\chi'' = \frac{\omega\tau}{1 + (\omega\tau)^2} \chi_0, \quad (25)$$

where χ_0 is the equilibrium susceptibility (as $\chi = \frac{\chi_0}{1+i\omega\tau}$) (Rosensweig, 2002). Therefore,

$$P_{sus} = \pi \mu_0 \chi_0 H_0^2 f \frac{2\pi f\tau}{1 + (2\pi f\tau)^2}, \quad (26)$$

where the magnetic susceptibility, χ_0 , is assumed constant (although with some dependence on the magnetic field).

To picture this heating, imagine the opposite process. For the magnetic moment of the nanoparticle to be constantly changing direction, it requires energy (heat) to be absorbed from the surroundings, and therefore a cooling effect is observed. If the opposite behaviour is desired, simply stopping the moment from changing direction at regular intervals will release heat into the surroundings.

4.3 Blocked Nanoparticles

Hysteresis heating involves blocked nanoparticles and occurs for particle diameters between d_{sp} and $d_v(H)$,

$$d_{sp}(H) = \frac{6 k_B T \ln(tf_0)}{\pi K}, \quad (27)$$

$$d_v(H) = \left(1 - \frac{H}{H_K}\right)^{\frac{2}{3}} d_{sp}, \quad (28)$$

where t is the time of measurement (Vallejo-Fernandez & Whear, 2013). Susceptibility heating no longer plays a role as the magnetisation of the nanoparticles will be switched when the magnetic field is applied. However, warming can still occur as the energy required to flip the magnetisation of the nanoparticles is released as heat into the surroundings. The magnitude of this released energy is calculated by the area of the hysteresis loop (as shown in Figure 11),

$$E = \int \mathbf{B}d\mathbf{M} \quad (29)$$

per unit volume where \mathbf{B} is the magnetic field and \mathbf{M} the magnetisation. The power generated is thus multiplication of the frequency of the alternating magnetic field and this energy,

$$P_{hyst} = f\mu_0 \int \mathbf{H}d\mathbf{M}. \quad (30)$$

Hysteresis heating has been proven to be the most effective for nanoparticle hyperthermia (Vallejo-Fernandez & Whear, 2013). It has been shown that the contribution to the overall heat output (also known as the specific absorption rate, or SAR – see section 4.6 *Comparing Nanoparticle Performance* for a full description) is more significant than with superparamagnetic nanoparticles or those of larger sizes (see 4.4 *Viscous Heating*).

4.4 Viscous Heating

For particles with diameters larger than $d_v(H)$ the magnetisation is not necessarily aligned with the field, preventing heating through hysteresis. However, viscous heating through stirring allows the nanoparticles to still produce heat when subjected to an oscillating magnetic field. Although exact equations describing this heating have not yet been developed, its heating effects should not be ignored as Vallejo-Fernandez & Whear (2013) demonstrated that it is not negligible, although it still pales in comparison to the heat output through hysteresis heating. As this effect is dependent on the surroundings, its contribution in vivo is highly variable and near impossible to calculate in the total heat production of the nanoparticle without extensive testing. For these reasons, this heating is not investigated in this thesis.

4.5 Limits on Applied Magnetic Field

Ideally, the alternating magnetic field affects only the magnetic nanoparticles. However, from Faraday's law, any alternating magnetic field will generate electric field gradients,

$$\nabla \times \mathbf{E} = -\frac{\Delta \mathbf{B}}{\Delta t}, \quad (31)$$

which in turn can produce eddy current heating in the surrounding tissue. If the direct eddy current heating is sufficient, nerve stimulation and even muscle stimulation are possible consequences; hence the need for an upper limit for the field strength and frequency was created. A plot of issues relating to these is included in Figure 14. The upper limit for $H_0 \times f$, the Atkinson-Brezovich limit, protects the patient against adverse reactions to a large and/or high frequency applied magnetic fields. Its value is $4.85 \times 10^8 \text{ Am}^{-1} \text{ s}^{-1}$ (Atkinson, Brezovich, & Chakraborty, 1984) and was calculated through consideration of the power deposited per unit volume (Wm^{-3}) in a cylinder of uniform tissue by an applied magnetic field,

$$P = \pi^2 \frac{\mu^2 \mu_0^2 \sigma}{2} f^2 r^2 H_0^2, \quad (32)$$

where μ is the relative permeability of the tissue, σ the conductivity ($\Omega \text{ m}^{-1}$), f the applied magnetic field frequency, r the radius of the specimen (m), and H_0 the amplitude of the applied magnetic field.

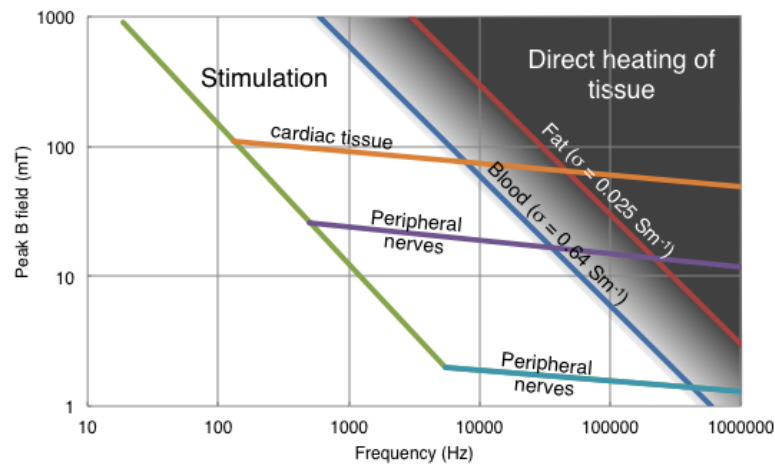


Figure 14 - Regions of the amplitude and frequency of an alternating magnetic field (AMF) applied to tissues that would generate direct eddy current heating at a power density of 0.025 W cm^{-3} or stimulate peripheral nerves and cardiac tissue. (Pankhurst, Thanh, Jones, & Dobson, 2009)

4.6 Comparing Nanoparticle Performance

The specific absorption rate (SAR) is a measure of power per mass of nanoparticle and is used to compare nanoparticle performances across current literature,

$$\text{SAR} = \frac{C\rho}{\varphi} \frac{\Delta T}{\Delta t}, \quad (33)$$

where C is the specific heat of the colloid, φ is the concentration per ml of solution, ρ the density of the colloid and $\frac{\Delta T}{\Delta t}$ represents the heating rate. Usually quoted in W/g, the SAR is not necessarily helpful in comparing performances of nanoparticles as different fields and frequencies are used to obtain these heating rates (SAR is proportional to P/ρ). Another method which gives a more accurate description of material performance is the Intrinsic Loss Parameter (ILP). This parameter is independent of the applied field amplitudes and frequencies (Kallimudil, et al., 2009),

$$\text{ILP} = \frac{\text{SAR}}{H^2 f} = \frac{P}{\rho H^2 f}. \quad (34)$$

These parameters are an easy way to compare nanoparticle performance values across literature and industry. A table is included below of some nanoparticle SAR values and their scaled values when the Atkinson-Bresovich limit of $H_0 \times f = 4.85 \times 10^8 \text{ Am}^{-1} \text{ s}^{-1}$ is applied.

As Table 1 shows, there is a tendency for researchers in this field to overestimate their nanoparticle performance or perhaps a lack of understanding for how these nanoparticles will be applied in medicine. After scaling to the Atkinson-Bresovich limit, it is clear that my predecessor, Atkas (2014), has produced the highest SAR values to date.

Nanoparticle	Size (nm)	Applied field Amplitude, H_0 (kA/m)	Frequency, f (kHz)	Reported SAR (W/g)	Scaled SAR (W/g)	Reference
Fe@Fe _x O _y	16	9.7	50	192	192	(Atkas S. , 2014)
Fe nanocube	16	52.5	300	1690	52	(Mehdaoui, et al., 2010)
Fe ₂ O ₃ maghemite	16.5	24.8	700	1650	48	(Fortin, et al., 2007)
Fe magnetosome	35	10	410	1000	118	(Hergt, Dutz, Muller, & Zeisberger, 2006)
CoFe ₂ O ₄ @MnFe ₂ O ₄	15	37.3	500	2280	59	(Lee, Jang, Choi, & Moon, 2011)
MnFe ₂ O ₄ @CoFe ₂ O ₄	15	37.3	500	3034	78	(Lee, Jang, Choi, & Moon, 2011)
Co@Co _x O _y	6	10	400	720	85	(Bonnemann, et al., 2003)
Zn _{0.4} Co _{0.6} Fe ₂ O ₄ @Zn _{0.4} Mn _{0.6} Fe ₂ O _{0.4}	15	37.3	500	3866	100	(Lee, Jang, Choi, & Moon, 2011)

Table 1 – Reported and scaled SAR values of nanoparticles with the AMF parameters and their references including one made from our own group previously.

4.7 The Optimal Nanoparticle for MNH

To summarise this section, an overview of the desired nanoparticle characteristics for magnetic hyperthermia is presented. Firstly, as can be seen from equation (32), a nanoparticle with a large magnetic moment and a high saturation magnetisation is desired. Iron is the obvious choice as the core material, due to its high magnetic moment and relative ease of synthesis with our experimental set up.

Secondly, the nanoparticle should preferably exhibit hysteresis heating, as this behaviour produces the most heat output out of the three states the nanoparticles can be in (Vallejo-Fernandez & Whear, 2013). This means the nanoparticles should not be superparamagnetic, rather, they need to be blocked and therefore of a larger diameter.

Thirdly, as Atkas, et al., (2015) investigated through MRI, the shape of the nanoparticle has an effect on its magnetic properties. This study showed that cubic nanoparticles performed best for MRI contrast agents, but this may not necessarily be true for hyperthermia. The shape of the nanoparticles is thoroughly investigated within this thesis in the following data chapters.

5. Magnetic Resonance Imaging

5.1 Introduction

This section explains the physics of nuclear magnetic resonance and how this phenomenon is manipulated in magnetic resonance imaging (MRI). At a basic level, MRI shows information an X-ray/CT cannot; it has the capability to image soft tissues. MRI not only gives information relating to proton density (of hydrogen atoms located within water molecules), but also information on the capacity of those hydrogen containing molecules to rotate. Furthermore, data on the proportion of water contained in the different tissues can also be extracted. From these pieces of information, a three-dimensional image can be produced of differing soft tissue contrasts with anatomical detail; a vital tool in diagnostic medicine. However, the contrast due to proton MRI is poor.

To improve MRI contrast, various MRI contrast agents have been developed. Contrast agents are in the form of an injectable fluid which contains material that either increases or decreases the MR signal in the tissue in which the fluid is up-taken. Current MRI contrast agents include Gd^{3+} which decreases the signal in T_2^* imaging – this is explained in more detail in the following section (Webb, 1988). A particular example is shown in Figure 15, where the breakdown of the blood-brain barrier is far clearer in the MR image with an added contrast agent than in the MR image without. From this, one can clearly see the benefits of using contrast agents within diagnostics.

Nanoparticles investigated in this project have the potential to be good MRI contrast agents, hence an explanation of MRI techniques and MRI contrast agents is given here.

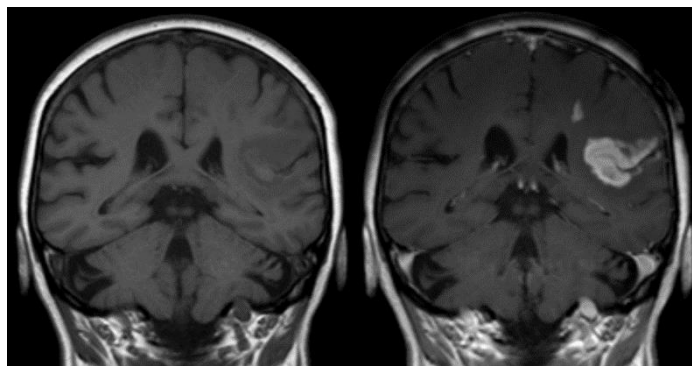


Figure 15 - MRI with (right) and without (left) a contrast agent added on a patient following a stroke where the blood-brain barrier has been broken down (Hellerhoff, 2010)

5.2 MRI Basics

When a homogenous magnetic field B_0 is applied to a body of protons, they respond by aligning in a low energy configuration: either parallel or anti-parallel to the applied magnetic field. The two populations differ in number (slightly more protons align parallel) inducing a net magnetisation in the body of protons (known as the longitudinal magnetisation, M_z). The energy separation between the two states is

$$\Delta E = \hbar\omega_0, \quad (35)$$

where \hbar is the reduced Planck constant and ω_0 is the Larmor frequency (the frequency at which the spins precess around the alignment). As

$$\omega_0 = \gamma B_0, \quad (36)$$

where γ is the proportionality constant between the magnetic moment and the angular momentum known as the gyromagnetic ratio, then,

$$\Delta E = \hbar\gamma B_0. \quad (37)$$

Transitions can then take place from the lower (spin down) to the upper (spin up) state if energy is supplied at the Larmor frequency. A radio frequency (RF) pulse at the Larmor frequency is applied to rotate M_z by 180° to reverse M_z or by 90° to remove M_z and produce a transverse magnetisation vector $M_{x,y}$.

Bloch (1946) introduced a set of equations to describe the behaviour of the nuclear magnetic moment of a non-interacting sample of spins. The equation of motion for a single proton under the influence of an applied field with a flux density B is given by,

$$\frac{d\mathbf{M}}{dt} = \gamma\mathbf{M} \times \mathbf{B} \quad (38)$$

Equation (38) can be separated into longitudinal and transverse magnetisations,

$$\frac{dM_z}{dt} = -\frac{M_z - M_0}{T_1},$$

$$\frac{dM_{x,y}}{dt} = -\frac{M_{x,y}}{T_2}, \quad (39)$$

where M_0 is the equilibrium value of the longitudinal magnetisation, T_1 the longitudinal relaxation time and T_2 the transverse relaxation time.

The longitudinal relaxation is often referred to as spin-lattice relaxation as it describes the transfer of energy to/from the spin system, inducing changes in spin-state. It gives valuable information on the vibrations within the lattice: a measure of the water molecules' ability to rotate. The transverse relaxation or spin-spin relaxation is caused by the loss of phase coherence in the xy-plane and because of longitudinal relaxation. Other than the T_2 relaxation, inhomogeneities in the magnetic field also affect the loss of transverse magnetisation; their combined effects are given as the effective transverse magnetisation, T_2^*

$$\frac{1}{T_2^*} = \frac{1}{T_2} + \frac{\gamma\Delta B}{2}. \quad (40)$$

The spin-echo sequence is the most common RF pulse sequence used in MRI and consists of a 90° pulse to force a transverse component of the magnetisation followed by an 180° pulse to re-align the spins as they instinctively de-phase. The signal is measured once to spins have fully re-aligned at the echo, see Figure 16.

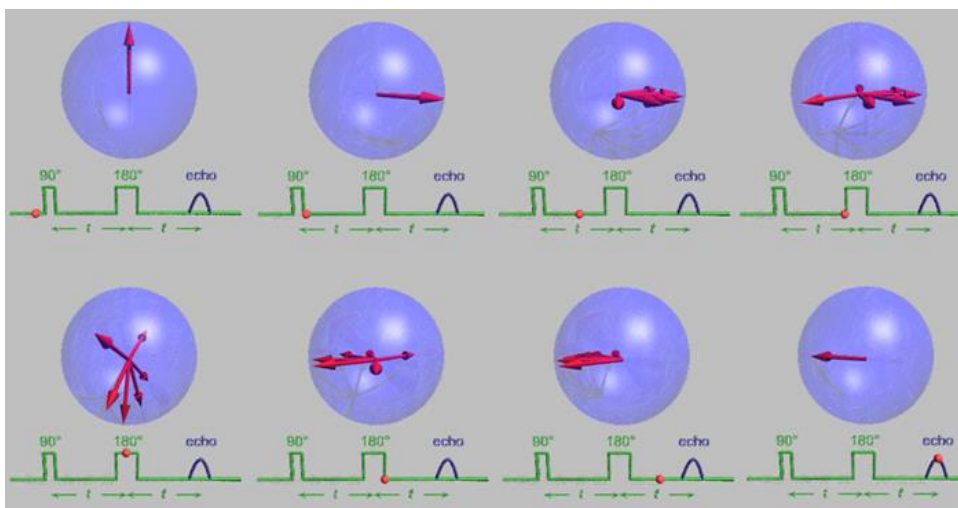


Figure 16 - The spin-echo sequence illustrated with red arrows to represent the proton spins within hydrogen. (Morley, 2011)

Characteristic T_1 , T_2 , and T_2^* values differ for various soft tissues and so after the pulse is applied, different tissues will relax at different times producing contrast in the image.

As the resonant frequency of the protons is proportional to the applied magnetic field, an application of a linear magnetic field gradient along the z-axis will cause the resonant frequencies of the protons to differ with z displacement;

$$\omega(z) = \gamma B_0 + \gamma z G_z, \quad (41)$$

where $\omega(z)$ is the resonant frequency and G_z (Tm^{-1}) is the applied z-field gradient. Therefore, once the signals have undergone Fourier transformations, the frequency axis will be equivalent to the z gradient and a spatial map can be produced.

5.3 Contrast Agents

The characteristic times for the longitudinal magnetisation to return to its pre-pulse value (T_1) and for the transverse magnetisation to return to zero (T_2) are highly sensitive to the local chemical environment and vary for different tissues. The introduction of magnetic fluids enhances the contrast in MRI by reducing local relaxation times; such contrast agents currently available are Gd chelates, superparamagnetic iron-oxide nanoparticles (SPIOs) ~ 100 nm in diameter and ultra-small superparamagnetic iron oxide (USPIOs) nanoparticles ~ 50 nm diameter (Na, Song, & Hyeon, 2009).

Magnetic nanoparticles with higher moments than those currently used in MRI will undoubtedly aid diagnosis as they will have a larger impact on the relaxation times, thus producing a larger contrast for the same amount of colloid (or possibly less material).

To compare nanoparticle contrast performance, the relaxivity is used:

$$R_{i(obs)} = \frac{1}{T_{i(obs)}} = \frac{1}{T_{i(diamag)}} + r_i C \quad (42)$$

where $i = 1$ or 2 , representing the longitudinal or transverse magnetisation respectively, $R_{i(obs)}$ is the observed relaxation rate of the system with the added contrast agent, $T_{i(diamag)}$ is the relaxation time of the system without the contrast agent added, r_i is the

relaxivity of the contrast agent in $s^{-1} \text{ mmol}^{-1}$, and C is the concentration of its active ions in mmol l^{-1} .

The relaxation rates are directly proportional to the square of saturation magnetisation, M_S , and the square of the particle diameter,

$$R_i \propto M_S^2 d^2 \quad (43)$$

Equation (43) demonstrates that a nanoparticle with a high saturation magnetisation and a large diameter, within the single domain size range, would give the highest relaxation rate, and thus be the optimum type of nanoparticle for contrast imaging in MRI.

5.4 The Optimal Nanoparticle for MRI contrast

To summarise, the nanoparticles ideal for MRI are those with high magnetic moments, a high saturation magnetisation, and those that exhibit superparamagnetism (and therefore are in the single domain range). This means the nanoparticles suited to MRI will generally be smaller than those optimal for MNH. The nanoparticle should be the largest physically possible within the superparamagnetic range to be the most efficient as an MRI contrast agent.

Using Fe gives a high magnetic moment and a high saturation magnetisation value and is relatively easy to synthesise with our experimental set-up.

6. Magnetic Particle Imaging

6.1 Introduction

Magnetic Particle Imaging (MPI) is a new diagnostic tool currently under development (Gleich & Weizenecker, 2005). This emergent imaging system uses the non-linearity of the magnetisation curves of ferromagnetic materials, as well as their saturation magnetisation at particular magnetic field strengths, to produce images of tracer density. The tracers may be targeted to a particular site through attachment of appropriate biological moieties or there may be natural processes that cause the nanoparticles to accumulate. One such example of natural accumulation is the enhanced permeability and retention (EPR) mechanisms observed in cancers.

MPI is very promising in terms of contrast and sensitivity as the bulk SPIO magnetisation is 107 times more intense than the nuclear paramagnetism of water detected with a 7 T MRI scanner (Goodwill, 2009).

6.2 Principles

An assembly of magnetic nanoparticles is excited by an external oscillating magnetic field ($\sim 10 - 100$ Hz) known as the modulation or drive field, H . The magnetisation of the nanoparticles, M , is detected and measured by the induced voltage in pick-up coils and it not only includes the drive frequency, but a series of harmonic frequencies,

$$M(H, T) = c\mu \left[\cosh\left(\frac{\mu\mu_0 H}{k_B T}\right) - \frac{k_B T}{\mu\mu_0 H} \right], \quad (44)$$

where c is the concentration of nanoparticles (number/m³), μ their magnetic moment, T their temperature and k_B , Boltzmann's constant. As this induced voltage signal is orders of magnitude lower than that of the modulation field, the non-linear dependence of M on H allows for it to be measured by detecting the harmonics of the applied field frequency. A study by Weaver, et al., (2008) has shown that the addition of a static magnetic field replaces the odd harmonics measured in the induced signal with even harmonics, significantly increasing the overall induced signal.

Including a time-independent magnetic field which is non-zero in all places bar one (the selection field) allows for spatial encoding. Application of the selection field saturates all the magnetic moments apart from those within the 'field-free point' (FFP). This means only the signals from the nanoparticles at this FFP are inductively measured as they easily align with the applied oscillating drive fields whereas all other nanoparticles are forced to align with the selection field. The FFP can be moved across the field of view with additional drive fields to give an image of nanoparticle density. The basic process of producing a signal is shown in Figure 17.

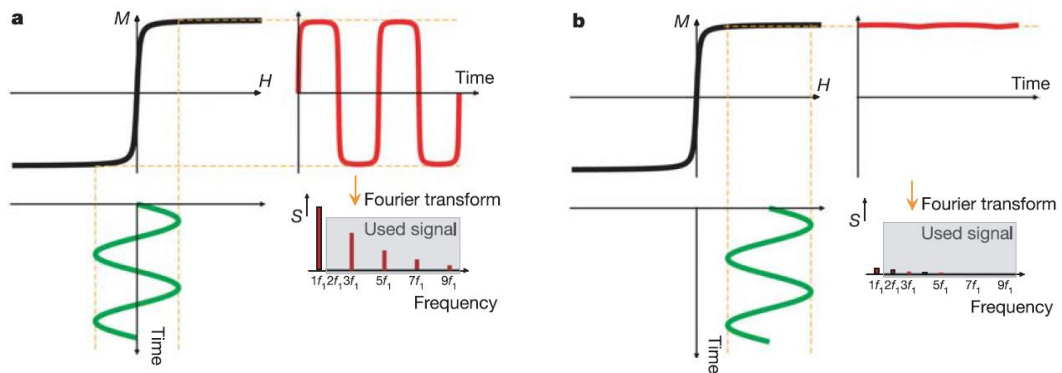


Figure 17 – **a** Manipulation of the nonlinearity of M-H curves gives a steady cyclic signal when an oscillating magnetic field is applied. Fourier analysis reveals the harmonic frequencies. When a static magnetic field is also applied to saturate the nanoparticles (as with **b**), the induced signal reveals no significant frequencies when put through Fourier analysis. (Gleich & Weizenecker, 2005)

6.3 Instrumental Design

Figure 18 shows the generic set-up of the selection coils, drive field coils and recording coils (Weizenecker, Gleich, Rahmer, Dahnke, & Borgert, 2009). Permanent magnets and a Helmholtz coil-style arrangement with opposing currents provide the selection field. The selection field produces the FFP, which can be moved using homogeneous oscillating fields (the Helmholtz-like set-up) to give 1-D spatial coding. To achieve 3-D imagery, an extra pair of orthogonal drive field coils is required and by differing the frequencies of these only slightly, a 3-D Lissajous trajectory can be produced. The use of drive field coils instead of mechanical movement significantly decreases scan time, an important factor when its applications in medical imaging are considered.

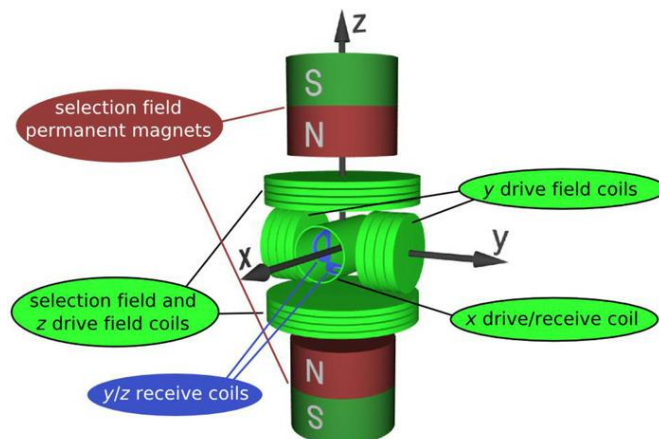


Figure 18 - Diagram of 3D MPI Scanner taken from (Weizenecker, Gleich, Rahmer, Dahnke, & Borgert, 2009)

A Lissajous trajectory (Weizenecker & Gleich, 2007; Knopp, et al., 2009) was found to yield the best image quality even with a low density of ions when compared with Cartesian, radial and spiral sampling patterns. The radial sampling pattern showed better results at the centre but was worse at the edges when compared with the Lissajous, so both could play a role in future MPI sequencing. However, Lissajous trajectories require only two dedicated frequencies (in the drive fields) meaning the signals from the drive fields can be band-pass filtered to compensate for harmonic distortions of available amplifiers; the radial pattern would require extra filters to eliminate such distortion. The two receiver coils are arranged perpendicular to the centre, and the solenoid drive field coil can also be used to receive signal.

The size of the bore has been increased to 120 mm (Gleich, et al., 2010) ever increasing the practicalities of MPI as a medical imaging device. Although simulations show scaling up the conventional scanner to fit humans is feasible, the practicalities of this have not yet been realised. A possible solution to this would be a single sided scanner negating the requirement of a bore large enough to encompass a patient; theoretically enabling any sized object be imaged. Figure 19 shows the basic setup of such a 2-D scanner (Sattel, et al., 2009) whereby two concentric transmit coils and a separate receive coil. The selection field is generated by DC currents in opposing directions as shown by the arrows.

There are obvious constraints on depth due to attenuation of the magnetic field but none set on object size. This advantage has been utilised in other imaging modalities such as ultrasound.

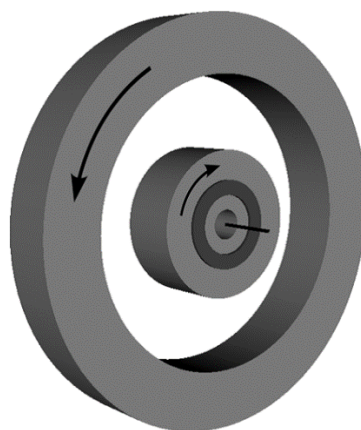


Figure 19 - Setup of a single-sided MPI scanner made up of two concentrically positioned transmit coils (light grey) and a separate receive coil (dark grey). The selection field is generated by direct currents of opposite direction (indicated by arrows). The 1-D field of view is indicated schematically as a black line (Sattel, et al., 2009)

6.4 The Optimal Nanoparticle for MPI

The most ideal nanoparticle for MPI is a large, single-domain magnetic nanoparticle. The larger the nanoparticle is, the better the sensitivity is for MPI, which will lead to the production of better images. As is clear from Figure 17, a high saturation magnetisation will allow for a clearer received signal, thus increasing the sensitivity.

7. Summary

To summarise, the nanoparticle characteristic desired for all three applications is a large magnetic moment. For MRI and MPI, superparamagnetic nanoparticles detailed here are the most suitable whereas blocked nanoparticles, i.e. those that produce heating through hysteresis, are more suitable for hyperthermia treatments. Therefore, a variety of nanoparticle sizes with a strong magnetic moment are required.

As Fe readily oxidises when exposed to air and/or water, a core shell nanoparticle, consisting of a protective shell surrounding a pure Fe core would allow the magnetic core to remain un-oxidised. It would therefore have a much higher magnetic moment than an Fe-oxide nanoparticle. The following chapters describe the evaluation of various core shell nanoparticles, with different shell materials surrounding an iron core. As previously mentioned, the shape and size of nanoparticle also has a great impact on the magnetic properties, and these characteristics are also investigated in the following chapters.

Chapter 4: Pure Fe Studies

1. Introduction

To produce the highest performing nanoparticles (i.e. the highest SAR values), the size of the nanoparticle, its constituent material, and also its shape must be intelligently designed and optimised. This is due to the nature of magnetic behaviour at the nanoscale as detailed in *Chapter 3: Magnetic Nanoparticle Theory and Medical Applications*. If the nanoparticles are too large, they no longer produce heat through superparamagnetic or hysteresis heating: only through friction due to physically stirring the nanoparticle. As is outlined in more detail in *Chapter 3: Magnetic Nanoparticle Theory and Medical Applications*, the main magnetic contribution to magnetic hyperthermia is hysteresis heating. This is produced by small single- or multi-domain nanoparticles, i.e. not superparamagnetic systems.

As described in *Chapter 3: Magnetic Nanoparticle Theory and Medical Applications*, the magnetic moment of the nanoparticle is proportional to the heating output. Therefore, it is paramount to select a material with a high atomic magnetic moment. Fe has a large atomic moment of $2.2\mu\text{B}$ in the bulk, with higher values recorded at the nanoscale. It has been shown, however, that FeCo nanoparticles currently have the highest magnetic moment (Heck, 1974) but this not easily synthesised within our laboratory. Fabrication of FeCo nanoparticles with our experimental set-up would possibly require the use of two sputter heads, one for Fe and the other for Co. This may well produce FeCo alloys, but also other combinations of nanoparticle including Fe@Co, Fe, Co, Co@Fe, plus various other core-shell systems and alloys (for example, a FeCo core and a Co shell). As some of these systems have not been studied in great detail, their magnetic properties are relatively unknown and untangling the contributions of a large number of different species would be difficult. Fe nanoparticles are also relatively easy to synthesise with our experimental setup, and so Fe was chosen as the main constituent of our nanoparticles.

Once Fe was decided to be the core material, its limitations were investigated; the main issue being that iron oxidises readily when exposed to air and/or water. Fe-oxide has a lower atomic magnetic moment than Fe, therefore the oxidation reaction badly affects our nanoparticle performance. This oxidation cannot be avoided as our nanoparticles

must be dispersed in aqueous solution for medical applications. One solution to this problem is to produce a protective shell to physically prevent oxygen from coming into direct contact with the iron core. As detailed in *Chapter 2: Experimental Methods*, we used a heated crucible to add a shell to the Fe cores. This involves the insertion of a shell material into the crucible, and heating the crucible to a suitable temperature for the shell material to vaporise. The Fe nanoparticles are then forced through this (metallic) vapour and are coated as they pass through.

However, this process of shell addition involves heating the pure Fe cores and as shown previously by Atkas, et al., (2015), heating nanoparticles anneals them and causes a change in their shape from mostly cube/truncated cubes into predominantly cuboctahedrals. This chapter not only investigates the magnetic properties of iron nanoparticles but also investigates how the ratio of cubic to cuboctahedral shape varies with increasing crucible temperature. The effect that this shape change has on the nanoparticles' magnetic behaviour is also examined, through magnetometry measurements of samples of differing numbers of cubes, cuboctahedrals, and spheres. More specifically, the saturation magnetisation values are obtained from hysteresis curves produced from nanoparticle samples in magnetometry experiments. These shape changes are investigated with TEM imaging (at the University of Leicester and the University of York), and the correlating magnetic properties are explored with SQUID magnetometry via our collaborators in Barcelona, Spain, and through VSM with our collaborators at the University of Warwick. 12 TEM samples and 7 magnetometry samples have been investigated here, prepared with the (empty) core shell evaporator operating at varying powers, and therefore at various temperatures. Ultimately, this chapter aims to investigate the effect of heating Fe nanoparticles in terms of the shape, size and magnetic characteristics as these are paramount in determining the nanoparticles' ability to produce heat.

All 19 (12 TEM and 7 magnetometry) samples in this chapter have been produced in SLUMPS under the same conditions as outlined in *Chapter 2: Experimental Methods*. That is, the sputter magnetron operates between 10 W and 20 W, with Ar gas inputted into the system at the sputter head giving pressures of $P_1 \sim 30$ mbar and $P_3 \sim 2 \times 10^{-4}$ mbar. The core shell evaporator is operated between 2.0 A and 6.0 A without any material

present (i.e. a clean crucible), and the pure iron nanoparticles are deposited onto TEM grids or Si wafers.

As the TEM grids must be removed from our vacuum system to be transported into the JEOL 2100 at Leicester or into the JEOL 2200 TEM at the University of York, there is some inevitable oxidation of our nanoparticles. This is easily shown in the TEM images in Figure 20 where a thin shell of Fe-oxide is visible. Hence, strictly speaking, the Fe nanoparticles in this study should be considered as core-shell nanoparticles with a thin oxide shell, rather than pure Fe particles. All analysis undertaken on such images will include this oxide shell as well as the pure Fe core. For example, the area and diameter measurements encompass the whole nanoparticle, including this thin oxide shell.

The nanoparticle samples made for SQUID and VSM magnetometry are produced in an Ag matrix and can be assumed to be pure iron with no oxidation as they are adequately capped with Ag (> 50 nm cap). In addition, magnetometry samples of Fe in SiO₂ and Ge matrices were also prepared. All samples have a similar buffer (> 20 nm) and cap (> 50 nm).

Samples were also prepared for R.F. heating experiments with an infrared detection camera. These included similar buffers and caps to the magnetometry samples (i.e. > 20 nm buffer and > 50 nm cap) but were deposited on glass slides of 24 mm x 24 mm x 1 mm in size rather than on Si wafers. This is a requirement of the experimental set-up in Toulouse. The matrix materials used for these experiments include Ag, SiO₂, and Ge as mentioned in the previous paragraph.

2. TEM Data

2.1 Introduction

All samples in this section were created using the sputter source outlined in *Chapter 2: Experimental Methods* and deposited on Cu TEM grids within the vacuum system. The nanoparticles were deposited on S160, lacey, and holey carbon films depending on whether they were intended for HRTEM or TEM. Generally, lacey or holey grids are better for higher resolution images as they allow for more nanoparticles to be deposited at the edge of the carbon film. This then means there is less background imaged, and a clearer picture can be obtained.

As described above, the TEM samples were unavoidably exposed to air in transit between the deposition source and the JEOL 2100 TEM at Leicester, or the JEOL 2200 TEM at York; this therefore means they all have a thin oxide shell. The TEMs were utilised to obtain 2-D images of our nanoparticles and some example images are shown in Figure 20.

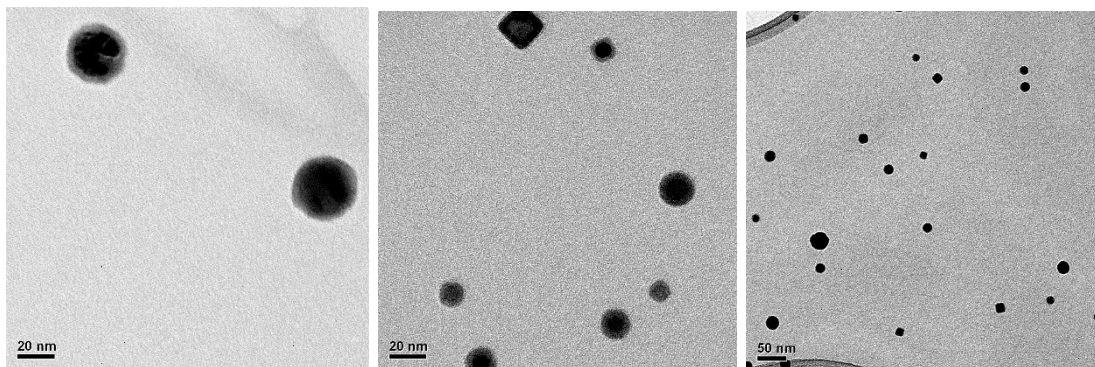


Figure 20 - TEM images of the pure Fe nanoparticles. Scale bar for each image shown in bottom left.

One can get a feel for the shape differences between the nanoparticles in a sample. There are obvious cubes (top nanoparticles in the centre image) and multiple spherical but also some cuboctahedra-types (top nanoparticle, left image). The coverage across the TEM grid is achieved by depositing approximately 2 - 3 Å of Fe. To measure such a thickness, the crystal thickness monitor (XTM – see *Chapter 2: Experimental Methods* for details on its workings) is employed before and after deposition, and an average rate taken over the total deposition time. This is then converted into an approximate amount of Fe deposited onto the TEM grid. For example, if the rate was measured to be 2.2 Å/min before deposition, and 1.8 Å/min afterwards, then the total Fe deposited onto the grid in 1 minute is estimated to be 2.0 Å or 0.2 nm. This would correspond to approximately 1 % of the TEM grid being coated in nanoparticles, if we assume their diameter is of the order 20 nm.

2.2 Analysis Methods

To analyse the shape of the nanoparticle, a geometry factor was utilized, which is extracted from the 2-D TEM image of the nanoparticle form. The geometry factor is calculated by dividing the true area of the nanoparticle measured from the TEM image by the maximum area possible if the nanoparticle were a perfect circle. For example, in

a square you would take the diameter from corner to corner, through the centre of the square, and use this diameter to calculate the area of a circle of the same diameter and then divide it into the actual area of the original square. To obtain this information, the analysis package ImageJ was utilised as it has the capability to measure the Feret diameter.

The Feret diameter of the nanoparticle, the measured maximum diameter, is used to calculate an area of a perfect circle with this diameter. This area is then divided into the true area of the nanoparticle from the 2D TEM image. The ratio is 0.63 for a perfect square and 1.0 for a perfect sphere and allows for good judgement of the 2-D shape of the nanoparticle. This method was chosen due to its ease of implementation and removal of user subjectivity, as previous approaches by the group (Atkas, et al., 2015) were to view each nanoparticle individually and note down the shape based on their appearance. This is incredibly time consuming and heavily biased. The Feret diameter and true area measurement were obtained through ImageJ – an open source image processing software developed at the National Institutes of Health. ImageJ can edit, analyse, process images, and includes processing functions such as edge detection, smoothing, contrast manipulation and much more.

In the following plots, any geometry factor between 0.4 and 0.7 is classed as a square or a truncated square, and the particle assumed to be cubic. Between 0.7 and 0.8 the particle is categorised as a cuboctahedral and above 0.8, the nanoparticle is assumed spherical. Any area measurements quoted below refer to the true area of the nanoparticle from TEM images, as measured with ImageJ. A cubic nanoparticle is assumed to look like a square in 2-D, although it could be at an angle – this is one of the obvious drawbacks of using 2-D images to assume a 3-D structure and cannot be avoided with this technique. A cuboctahedral/cuboctahedron is a polyhedron with 8 triangular faces and 6 square faces and although can be projected orthogonally to look like a square, it is more likely that it will give either a hexagon or something with more sides than a square. This means its geometry factor will most likely be higher than a square, but lower than that of a sphere.

Figure 21 shows a snapshot of the process in which data is extracted from a TEM image. The image contrast is altered and binarised and then analysed. ImageJ uses a Sobel operator for edge detection as this highlights sharp changes in intensity in the image. This operator uses two 3×3 convolution kernels to calculate approximations of the

derivatives: one for the vertical and another for the horizontal (often denoted as G_x and G_y). Using this information, the gradient magnitude can be produced by calculating the square root of the sum of the squares of the two derivatives. If this value is above a certain threshold, it is deemed to be an edge. From these two derivatives, the gradient direction can also be calculated (arctan of their ratio).

These nanoparticles are then numbered and the edge outlined as shown in the final image of Figure 21 so that they may be checked for any erroneous measurements. Note the thin Fe-oxide shell clearly visible in the first image.

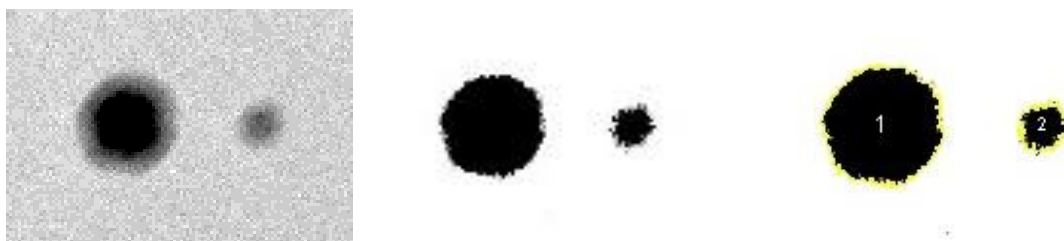


Figure 21 – A snapshot of the process in which data is extracted from a TEM image. From left to right: the raw TEM image, the binarised image and the edge tracking from ImageJ.

The data represented here encompasses 12 samples made at differing temperatures of the core shell evaporator and are given in Table 2. This is solely dependent on the quality of the TEM images, the number of images obtained, and the number density of nanoparticles on the grid. These temperatures encompass the entire range of the shell evaporator, from room temperature up to the temperature corresponding to the maximum input power to the heater. The maximum temperature achieved heavily relies on the number of shielding elements we are physically able to install in the shell evaporator. Too many, and the evaporator would not fit in the space available inside water cooling tank within the vacuum system; too few, and the heating would warm the whole system, affecting the electronics and operation.

Core Shell Temperature (°C)	Number of Nanoparticles Analysed
21 ± 2 °C	135
145.8 ± 45.2 °C	129
149.7 ± 45.1 °C	266
191.9 ± 45.0 °C	163
197.9 ± 45.0 °C	167
263.8 ± 44.7 °C	100
356.0 ± 44.4 °C	119
418.1 ± 44.3 °C	151
452.1 ± 44.2 °C	179
687.4 ± 43.6 °C	40
702.6 ± 43.6 °C	93
1137.1 ± 43.2 °C	85

Table 2 – 12 samples analysed here in this chapter, made at varying core-shell evaporator temperatures, and the corresponding number of nanoparticles analysed.

2.3 Results

Each dataset's geometry factor was separated into bins and plotted in a histogram and a distribution fitted. For these data-sets, the Weibull distribution (2-parameter) was best suited due to the nature of the data. Two examples of such histograms and their Weibull distributions are shown in Figure 22 where one can easily see that the data follows a skewed normal curve, to the right of the centre of dataset. This is due to the upper limit of this dataset being 1.00, and the majority of this data generally falling between 0.60 and 1.00 due to how the geometry factor is defined and the nature of the nanoparticle shapes.

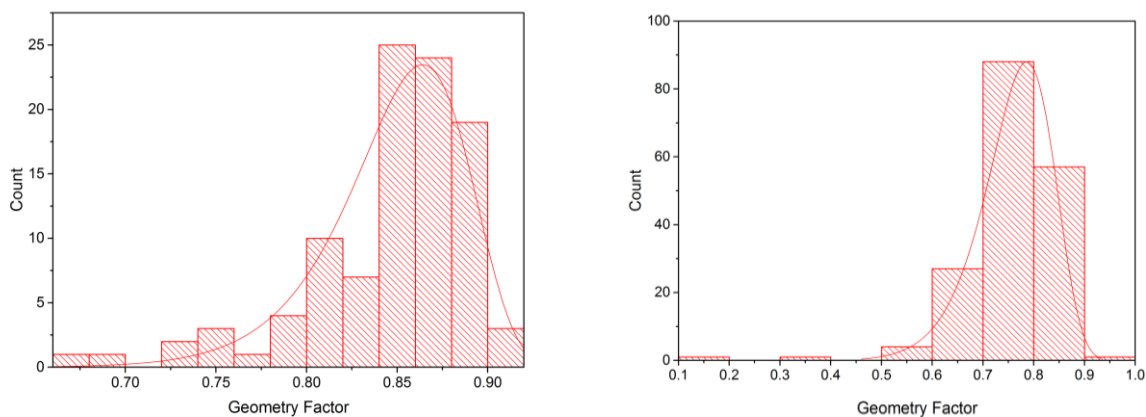


Figure 22 - Geometry Factor Histograms with Weibull distributions overlotted for pure Fe samples synthesised with the core shell evaporator operating at 263.8 ± 44.7 °C, (left) and 702.6 ± 43.6 °C (right).

The Weibull distribution is very useful for fitting data that follow an atypical normal distribution, with a skew in either direction. Mainly, it is used for right-skewed data as that shown in Figure 22 and it follows a stretched exponential distribution. The probability function of a Weibull is as follows,

$$P(x|a,b) = ba^{-b} x^{b-1} e^{-\left(\frac{x}{a}\right)^b},$$

where a is the scale parameter and b the shape parameter. The scale parameter indicates the spread of the distribution, where a large number indicates a large spread. The shape parameter gives an indication on the shape of the distribution. For example, a b value between 3 and 4 gives a bell-shaped curve, similar to a normal distribution. A value below this gives a left-skewed plot, much like a lognormal, whereas a value above 4 gives a right-skewed dataset, as is observed in the data presented in Figure 22.

Fitting the measured distributions to the Weibull distributions allows one to assign a mean value for the geometry factor, along with a \pm one sigma value, for each annealing temperature. This then gives an indication of the correlation between nanoparticle shape and annealing temperature (that is, the temperature of the core shell evaporator). Figure 23 shows the results of this analysis.

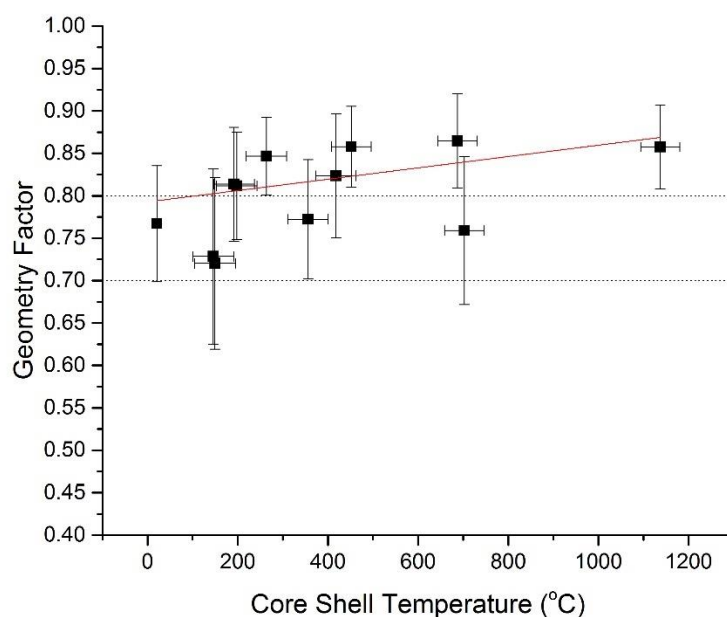


Figure 23- The geometry factor vs the temperature of the core shell evaporator for the pure Fe samples. The plotted values are the means of Weibull distributions fits plus a one sigma error bar. The dotted lines indicate the separation of the cubic (0.4 – 0.7), cuboctahedral (0.7 – 0.8), and spherical (0.8 – 1.0) regions

A linear regression was added to Figure 23 to illustrate the increase in geometry factor with a temperature rise. This suggests an increase in the number of spherical/cuboctahedral populations with an increased shell evaporator temperature.

By separating the data into number of cubic (geometry factor of 0.4 – 0.7), cuboctahedral (0.7 – 0.8) and spherical nanoparticles (0.8 – 1.0), it can be investigated how the proportion of each of these changes with temperature. Figure 24 illustrates this change.

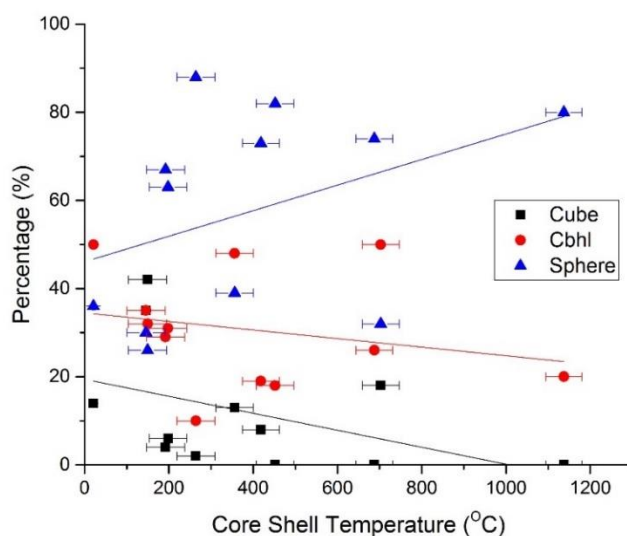


Figure 24 - The percentage of cubes (black squares), cuboctahedrals (red circles), and spheres (blue triangles) for each of the pure Fe samples.

The data in Figure 24 indicate that the increase in geometry factor seen in Figure 23 is most likely due to the increase in spherical proportions and a decrease in not only cubic, but also in cuboctahedral nanoparticles at higher temperatures.

Not only does the temperature affect the nanoparticle shape, it has been found that the size of the nanoparticles also increases with a rising temperature. Comparing the true area measured from TEM images through ImageJ, the area was seen to increase with the temperature of the shell evaporator. As with the geometry factor distributions, the area measurements were binned into histograms and the appropriate distributions fitted.

Figure 25 shows the histogram and lognormal fit over plotted for the sample produced with the core shell evaporator operating at 702.6 ± 43.6 °C. Although a Weibull distribution could be fitted to this distribution, we have followed convention in using a lognormal distribution. Similar graphs were produced for all 12 samples and their mean and one sigma value obtained from the lognormal distribution. These were then plotted versus the temperature of the shell evaporator as shown in Figure 26.

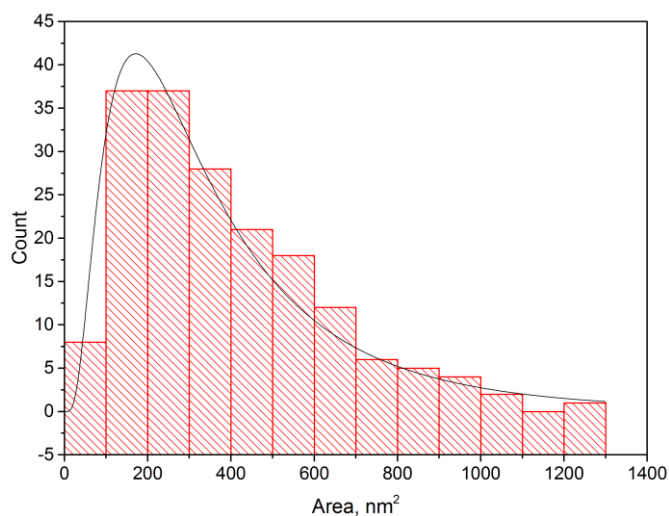


Figure 25 - An example histogram plus lognormal fit for the pure Fe sample made at 702.6 ± 43.6 °C. The means and one sigma values (error bars) plotted in Figure 26 are taken from this lognormal plot and others like it from the other samples.

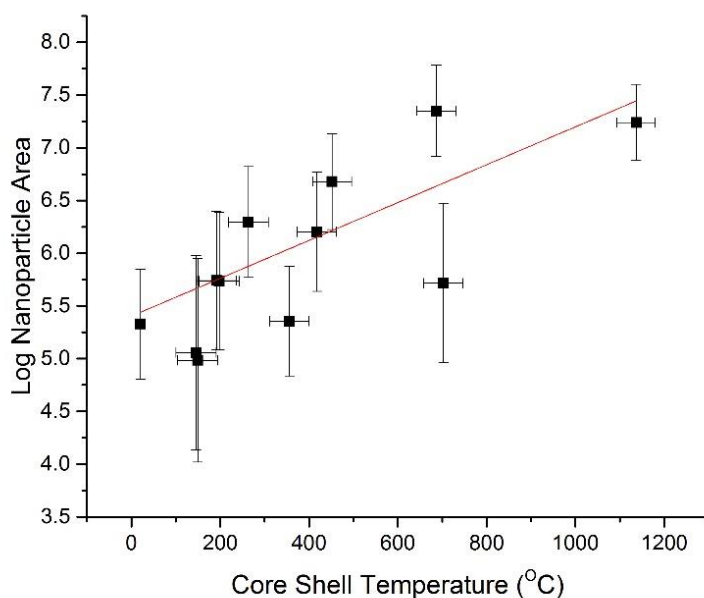


Figure 26 - The area of each pure Fe 2-D nanoparticle vs the temperature of the shell evaporator. Plotted values are the means of the sample from lognormal fitting with one sigma error bars. A linear fit has been added.

Figure 26 shows the surprising result that the nanoparticles increase in size when subjected to higher temperatures in the shell evaporator. From the true area measurements of the 2-D images of nanoparticles, the diameter can be inferred. The diameter measurements were calculated assuming spherical and cubic shapes, with the average of the two taken. These were then plotted into a histogram and fitted with lognormal

distributions. The mean and standard deviations (plotted as error bars) of these are plotted in Figure 27. This graph gives vital information on the spread of the nanoparticle diameters and their average size as a function of annealing temperature. For example, this linear relationship suggests that the nanoparticles are originally approximately 18 nm in diameter when no heat is subjected to them. This drastically increases to approximately 40 nm in diameter at around 1200 °C.

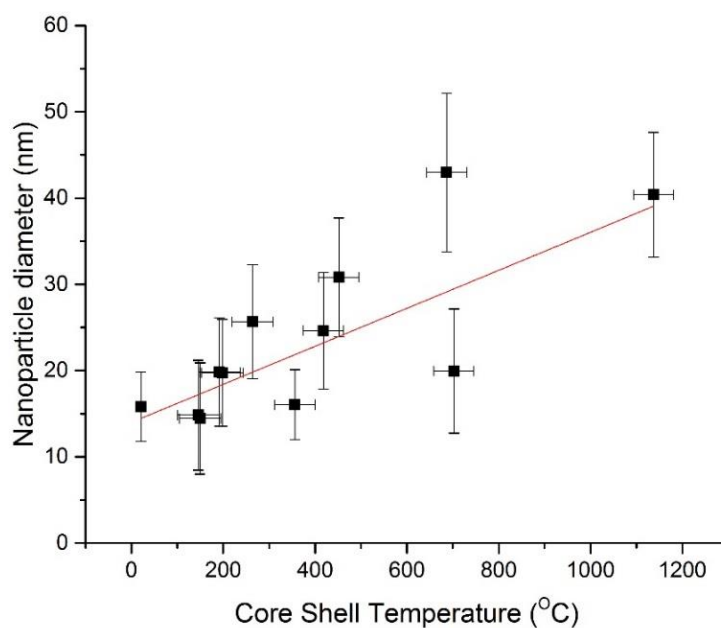


Figure 27- The diameter of each pure Fe 2-D nanoparticle vs the temperature of the core shell evaporator. Plotted values are the means of the sample from lognormal fitting with one sigma error bars.

In Figure 26 and Figure 27, only 3 samples suggest that an increase in core shell evaporator temperature gives a larger nanoparticle area. This is even less convincing when you consider the two samples synthesised at 687.4 ± 43.6 °C and 702.6 ± 43.6 °C, vary so widely even though their temperature may well be the same (within error). This argument holds even less weight when you consider that all of the other samples have at least 100 nanoparticles analysed, whereas these 3 samples have 40, 90, and 83, respectively. These 3 samples were also produced at a later stage than the other 9, which may well cause an increase in size due to technical issues, which are discussed in detail in the conclusions of this chapter.

Following on from the that there is possibly an increase in nanoparticle area/size and an increase in geometry factor with higher evaporator temperatures, it was decided to

investigate if these two observations were interlinked. That is, with a large nanoparticle is it likely to also have a high geometry factor?

The numbers from all of the nanoparticles in the dataset were plotted in Figure 28 where the true area of the 2D nanoparticles from the TEM images were plotted versus the geometry factor. It is clear from the cluster of points in the top-left of the plot that the vast majority of the nanoparticles are within an area range of 0 - 1000 nm² and a geometry factor ranging from 0.6 - 0.9, with very few nanoparticles with areas outside this range. Note there are almost zero with large areas (> 1500 nm²) and a low (< 0.7) geometry factor, indicating that large cubic nanoparticles are uncommon. This is further supported by the plots in Figure 29.

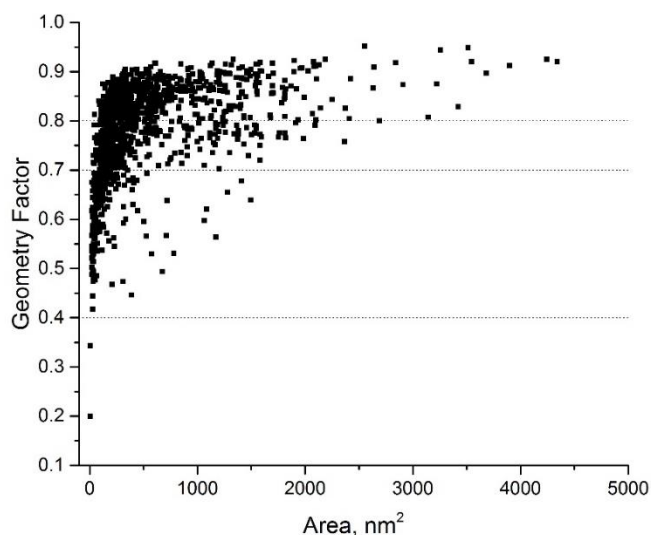


Figure 28- Geometry factor versus area for all 1929 pure Fe nanoparticles analysed in this dataset. The dotted lines indicate the separation of the cubic (0.4 – 0.7), cuboctahedral (0.7 – 0.8), and spherical (0.8 – 1.0) regions

Figure 29 a) shows the number of cubic (black), cuboctahedrons (red) and spherical (blue) vs. size for all of the samples (i.e. all 1810 nanoparticles within the 12 temperature ranges). This shows that the smallest nanoparticles contain a significant number of cubic shapes whilst the larger sizes are dominated by spherical shapes. This is further illustrated in Figure 29 b). These are separated into area bins of 200 nm².

Figure 29 a) shows that the majority of the nanoparticles are within the two lowest area bins 0 - 200 nm² and 200 - 400 nm² corresponding to 32 % and 30 % respectively. This equates to nanoparticles of approximately 0 – 22 nm in diameter (assuming spherical, 0

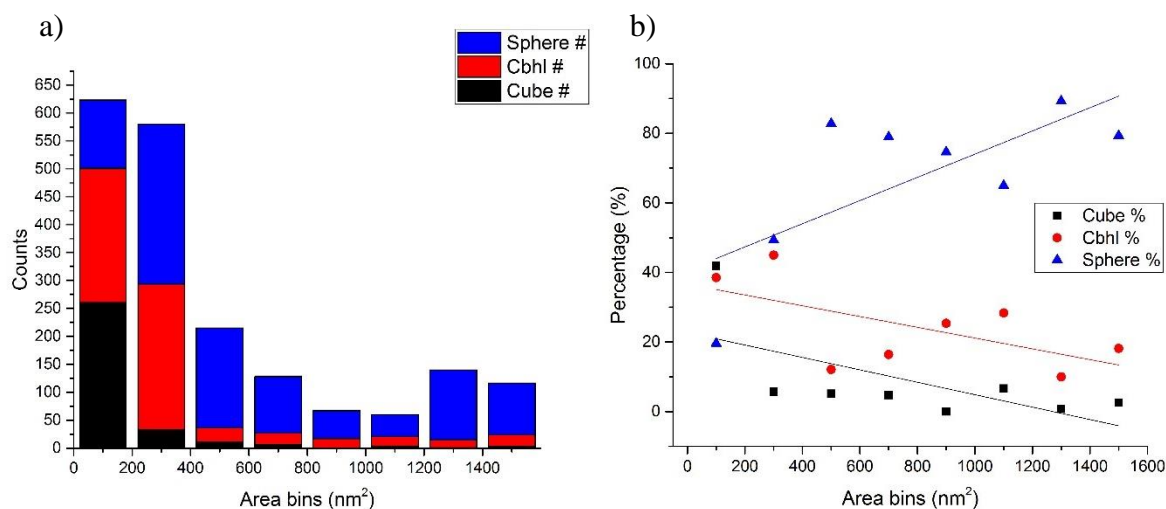


Figure 29 - Number of spheres (blue), cuboctahedrals/cbhl (red) and cubic nanoparticles in each area bin (200 nm² in size) for the pure Fe samples.

– 20 nm if cubic). From Figure 29 b), it can be seen the percentage of cubes are roughly equal across all the nanoparticle sizes apart from those with an area between 0 - 200 nm²: 42 % compared with 1 % - 6 % for all the nanoparticles larger than this. The cuboctahedrals, on the other hand, tend to decrease in number with increasing area, and those classed as spherical slowly increase in numbers in the larger area bins (20 % to 80 % from 0 – 200 nm² to >1400 nm², respectively). It is clear from Figure 29 a) and from Table 3 that for nanoparticle areas of 400 nm² or more, spherical shapes dominate.

Area bins, nm ²	Cube counts	Cuboctahedral (cbhl) counts	Sphere counts	Total Nanoparticles per area bin
0-200	261 (41.9 %)	240 (38.5 %)	122 (19.6 %)	623
200-400	33 (5.69 %)	261 (45.0 %)	286 (49.3 %)	580
400-600	11 (5.11 %)	26 (12.1 %)	178 (82.8 %)	215
600-800	6 (4.69 %)	21 (16.4 %)	101 (78.9 %)	128
800-1000	0 (0.00 %)	17 (25.4 %)	50 (74.6 %)	67
1000-1200	4 (6.67 %)	17 (28.3 %)	39 (65.0 %)	60
1200-1400	1 (0.71 %)	14 (10.0 %)	125 (89.3 %)	140
>1400	3 (2.59 %)	21 (18.1 %)	92 (79.3 %)	116

Table 3- Percentages of cubic, cuboctahedral, and spherical pure Fe nanoparticles per each area bin. Rounded to 3 significant figures. This data is plotted in Figure 29.

2.4 Discussion

Figure 23 shows that the geometry factor of our nanoparticles increases with an increased temperature in the core shell evaporator. This, alongside Figure 24, indicates that the numbers of cubic and cuboctahedral nanoparticle shapes decreases with an increase in temperature, and the percentage of spherical nanoparticles increases. This would suggest that a higher temperature in the evaporator has the ability to anneal our nanoparticles into spherical shapes.

Surface energy is a key property in material science. When a material is described as having a high surface energy, it is implied that strong interactions are present within the surface. Those with a low surface energy, like plastics for example, are difficult to coat, and therefore lack adequate wetting and adhesion. Surface energy can also be described as the work per unit area done by the force that creates the new surface.

As the temperature of a particle is increased, the cohesive force binding the atoms can be reduced due to vibrations. However, the surface energy can be altered by the addition of other elements or contaminants. The addition of such changes the balance of such forces and can possibly reduce the net inward force.

If the surface energy per unit area of the different shaped nanoparticles is compared (assumed the same volume), the reason for shape changes through heating can be uncovered. If we assume the cubic nanoparticle surface energy per unit area is 2123 J/m^2 (Fe bulk value), then the surface energies of cuboctahedral and spherical nanoparticles can be calculated as 1761 J/m^2 and 1714 J/m^2 , respectively (Atkas, et al., 2015). This suggests that the cubic and cuboctahedral nanoparticles are overcoming an internal energy barrier by heating, and this enables them to transform into a shape with a lower surface energy, i.e. a sphere.

Figure 26 and Figure 27 show the increase in nanoparticle size as the temperature of the core shell evaporator is increased. There are two possible reasons for this increase in nanoparticle area/diameter. One is that the heating is increasing the oxygen content of the nanoparticles, perhaps by components in the core shell evaporator outgassing but there is no evidence to support this from the TEM images, which show similar size ratios of the pure Fe core and thin oxide shell for all samples. Another explanation more fundamental to the deposition process is that some of the core nanoparticles coat the inner part of the

end of the shell evaporator and that this material is re-evaporated onto the free nanoparticles passing through. This has also been found in previous studies by the group for Au-coated Fe nanoparticles imaged by the super-STEM at Daresbury laboratory. In these samples a second shell of Fe was detected outside the Au shell and was ascribed to Fe nanoparticles hitting the end of the shell oven and re-evaporating material onto the core nanoparticles. In this case the effect is easier to see as the second Fe shell is deposited onto nanoparticles already coated in Au. One interesting aspect of those results is that it demonstrates that multiple shells can, in principle, be produced by subsequent evaporators. In order for the thermal deposition of shells to be more controllable, the unwanted deposition effect needs to be removed and this could be achieved by a “cold collimator” near the end of the shell evaporator, for example a heat shielded tube.

Comparing the geometry factor directly with the size/area of the nanoparticles also yielded interesting results. Figure 28 plots the area of the 2D nanoparticles from the raw TEM images versus their geometry factor. It is clear that the vast majority of the nanoparticles are within an area range of 0 - 1000 nm² and have a geometry factor ranging from 0.6 - 0.9 with very few nanoparticles with areas outside this range. Note that there are almost zero with large areas (>1500 nm²) with a low (< 0.7) geometry factor, indicating that large cubic nanoparticles are uncommon. This supports the previous discoveries that heating the nanoparticles increases their size and radically decreases the percentage of cubic nanoparticles (Atkas, et al., 2015). This is further supported by the plots in Figure 29 where the percentage of cubic and cuboctahedral nanoparticles are much lower in the higher area bins.

To conclude, an increase in the core shell evaporator temperature not only increases the percentage of spherical nanoparticles in the dataset, but also increases the nanoparticle size, from 18 nm at room temperature up to 40 nm at 1200 °C.

3. Magnetometry Data

3.1 Introduction

As outlined in the *Chapter 2: Experimental Methods*, samples were prepared for measurement in a SQUID magnetometer. These samples consisted of ~ 20 nm buffer layer of Ag, ~ 100 - 150 nm of 5 – 10 % Fe to Ag volume fraction, and a minimum cap of 50 nm Ag. The samples were deposited on Si (100) substrates of 7 mm x 5 mm, and stored in gelatine capsules for ease of transportation and analysis. Seven samples were produced at varying core-shell temperatures: 21 ± 1 °C, 225.9 ± 44.9 °C, 273.5 ± 44.7 °C, 346.5 ± 44.5 °C, 439 ± 44.2 °C, 783.9 ± 43.5 °C, and 1137.7 ± 43.2 °C. For all samples, the total sample moment was measured as a fraction of applied magnetic field, at 5 K and 300 K. The field was varied between ± 5 T.

The measurements enabled us to determine whether the nanoparticles were superparamagnetic or magnetically blocked. Saturation magnetisations and estimates for the heating that the particles could produce, were also obtained from the data.

3.2 Analysis Methods

The raw data was recorded in the format of total sample moment (in emu) versus the applied magnetic field when at 5 K, and at 300 K. The moment was then converted into Am^2 from emu and divided by the mass of Fe in the sample. The mass of Fe was estimated from XTM measurements before, during and after the sample deposition and an average coverage was taken for each time period. For example, if the deposition rate was measured to be 2 Å/s to start and then measured as 1.8 Å/s 15 minutes later, the average coverage for the 15 minutes was 1.9 Å/s, giving a total thickness of 1710 Å of nanoparticles deposited. Given that the silicon slides are 5×7 mm in size, and approximately 1 mm was covered by the mask holding them in place, an area of 4×6 mm was assumed to be coated. From this, the mass of Fe could be calculated.

Plotting the moment per gram of Fe (Am^2/g) values versus the magnetic field (T) yields the magnetisation curve, which characterises the magnetic behaviour of the nanoparticle sample. This can be in the form of a hysteresis loop, dependent on the size of the

nanoparticles produced and on the measurement temperature (see *Chapter 3: Magnetic Nanoparticle Theory and Medical Applications* for more information).

3.3 Results

Figure 30 a) shows the magnetisation curves for the 7 samples over the full field range ± 5 T at 5 K for an easy comparison of the saturation magnetisation values at each core shell temperature, whereas Figure 30 b) shows an expanded view of the hysteresis behaviour in the field range ± 1 T. Figure 31 a) shows the corresponding information but at 300 K for ± 5 T with b) showing this information between ± 0.5 T to highlight the hysteresis behaviour of the nanoparticles more clearly.

Figure 30 shows that the magnetisation curves for all samples have the same general shape. However, it can be noted that there is some interesting behaviour in particular for the sample produced at 21 °C. The curves for this sample do not show the regular smooth shapes of the others: the “bulging” between ± 0.5 T suggests that more than one different magnetic behaviours may be present. This could be due to the different magnetic responses of the cubic, cuboctahedral and spherical nanoparticles present within the samples. It is also worth noting that all the samples produced exhibit some form of hysteresis as is evident in the M-H curves in Figure 30 b). The graphs in Figure 31 show the exact same samples but measured at 300 K within the magnetometer Figure 30 and Figure 31 b) focussing on the expanded magnetic field range ± 0.5 T.

By fitting Langevin functions to the plots in Figure 30 and Figure 31, saturation magnetisation values were calculated and plotted against temperature, as shown in Figure 33. The error bars are \pm one sigma taken from the Langevin fits. The Langevin function describes the classical limit of the Brillouin function. Both can be used in studying paramagnetic materials.

The Brillouin function describes the dependency of the magnetisation, M , on the applied magnetic field, B , and the total angular quantum number, J , of the microscopic magnetic moments for an ensemble of non-interacting paramagnetic atoms or ions. Nanoparticles of magnetic materials such as Fe contain hundreds to thousands of atoms and can also behave paramagnetically. The exchange interaction locks the atomic moments together,

so the nanoparticle behaves as if it has a single giant moment. It therefore behaves like a classical magnetic dipole moment. This is why a classical description via the Langevin function is justified in this context. The Langevin function takes the form of,

$$L(x) = \coth(x) - \frac{1}{x}.$$

In the plots in Figure 30 and Figure 31, the magnetisation curves for our nanoparticles do not fit to a simple Langevin function, since they are modified by the hysteresis but the lower and upper saturation limits of the magnetisation do converge to a Langevin. The saturation magnetisations obtained from these fits are used to give a value for the saturation magnetisation for each of our nanoparticle samples. An example of such a fit is shown in Figure 32 - , with the sample produced at 225.9 ± 44.9 °C and measured at 5 K in the SQUID magnetometer. These fits (\pm one sigma) are plotted in Figure 33. It is clear from Figure 33 that an increase in evaporator temperature decreases the saturation magnetisation of the nanoparticles.

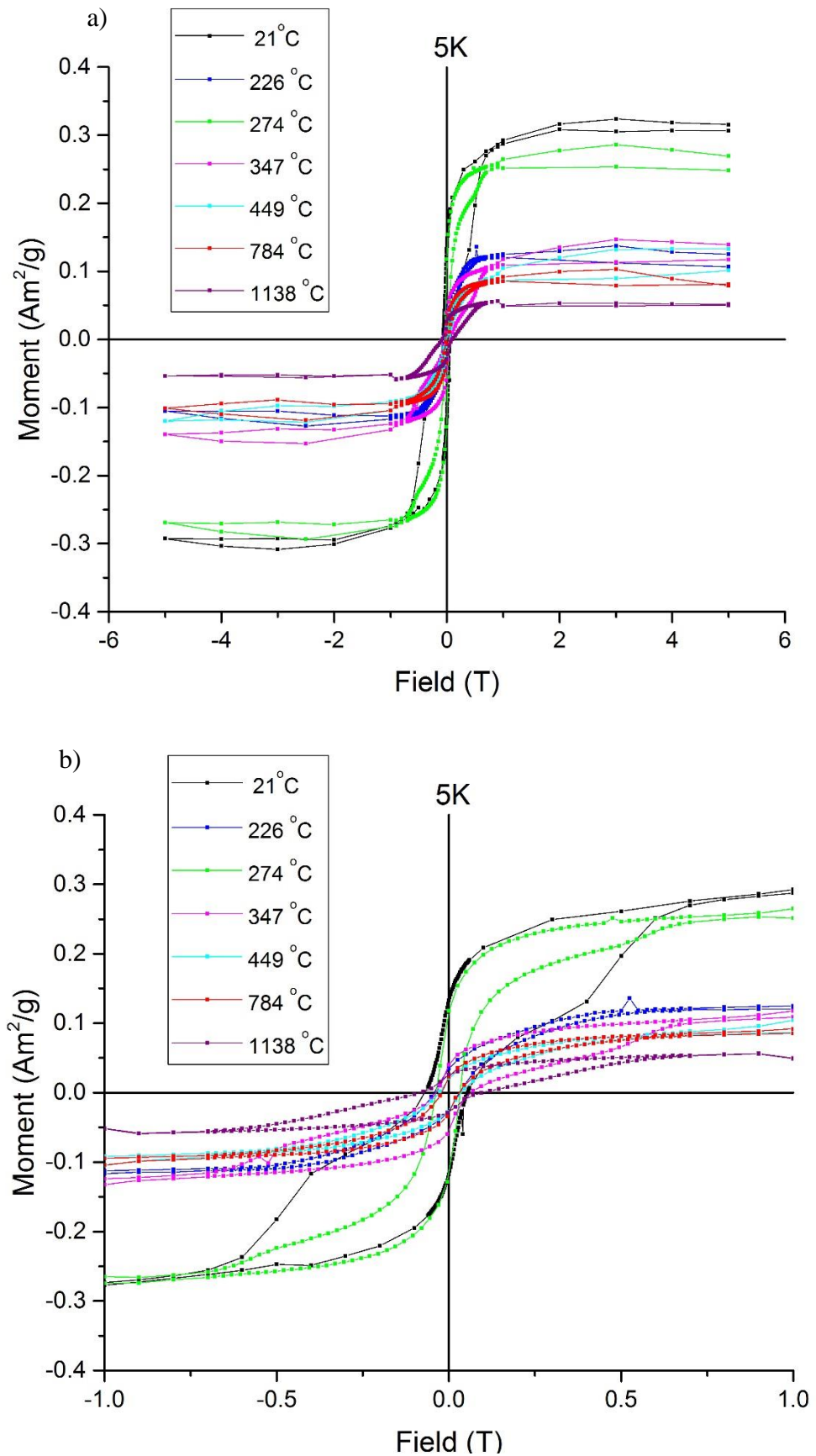


Figure 30 - Raw magnetometry data of the pure Fe samples in the SQUID at 5 K. a) shows the full data range obtained from ± 5 T, and b) shows the same data but between ± 1 T to show the hysteresis behaviour in more detail.

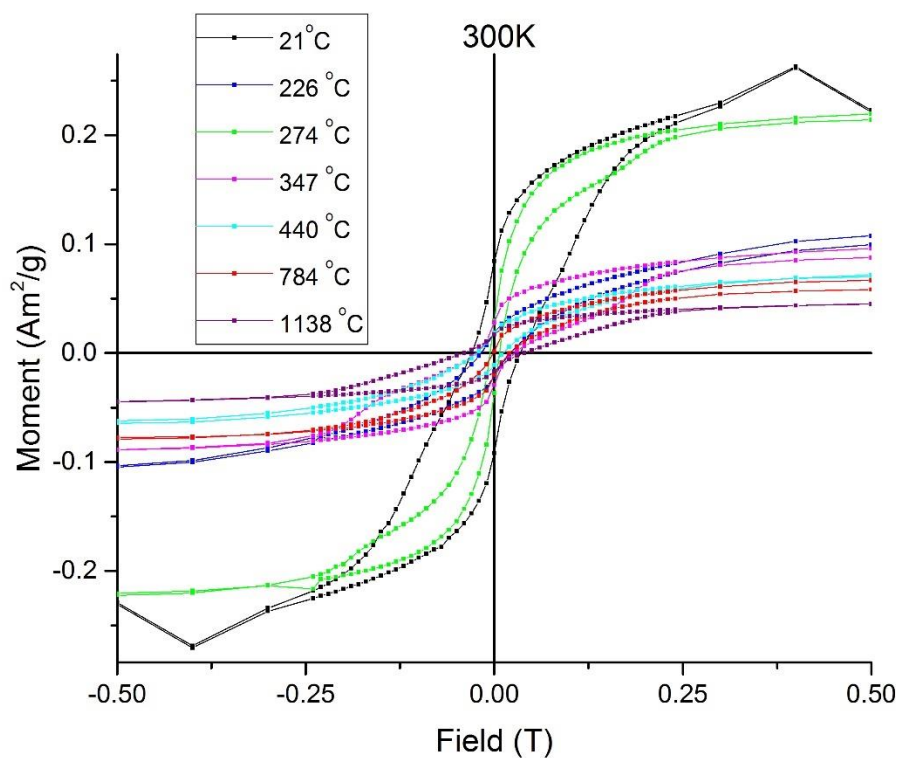
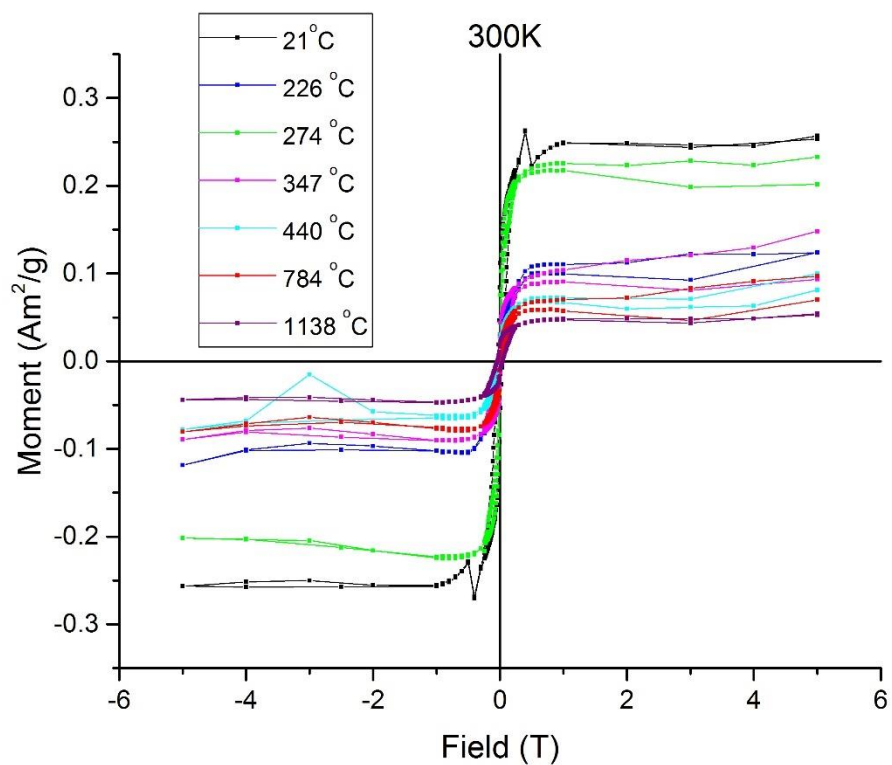


Figure 31- Raw magnetometry data of the pure Fe samples in the SQUID at 300 K. a) shows the full data range obtained from ± 5 T, and b) shows the same data but between ± 1 T to show the hysteresis behaviour in more detail.

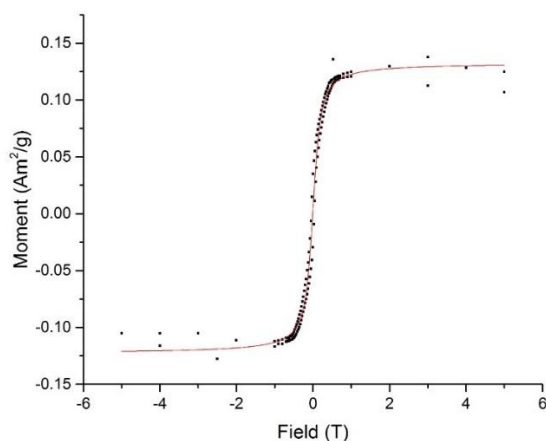


Figure 32 - An example of the Langevin fit applied to the pure Fe sample produced with the core shell evaporator operating at 225.9 ± 44.9 °C at 5 K in the SQUID magnetometer.

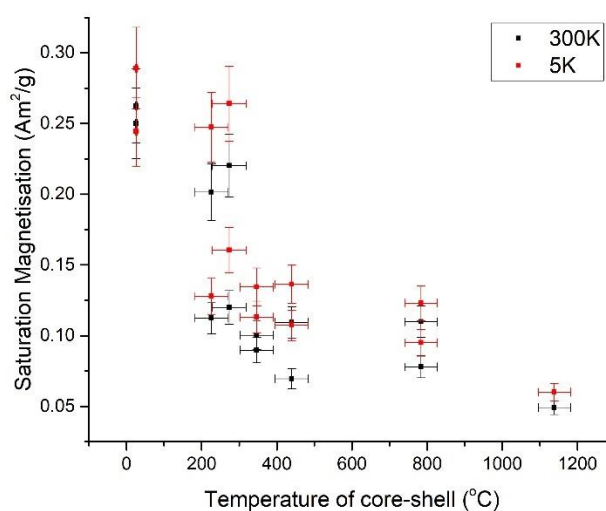


Figure 33 - Saturation Magnetisation from Langevin fits of the raw hysteresis curves shown in Figure 30 and Figure 31, plotted against the temperature of the core shell evaporator the pure Fe nanoparticles were subjected to.

As is explained in detail in *Chapter 3: Magnetic Nanoparticle Theory and Medical Applications*, not only is the saturation magnetisation of the nanoparticles important, but also the area enclosed by the hysteresis curve – this directly relates to the heat output of the nanoparticles. From the raw data displayed in in Figure 30 and in Figure 31 the areas of the hysteresis loops have been obtained and plotted against the temperature of the evaporator to investigate the effect that the evaporator temperature may have on the hysteresis heating produced by our nanoparticles. Figure 34 shows an example of the polygon area measured from the 1137.7 ± 43.2 °C sample at 300 K. However, this cannot be assumed to equate directly to the Specific Absorption Rate (SAR) usually measured

in W/g, as these measurements have been taken with a DC magnetometer, not an AC instrument. As shown by Carrey, et al., (2011), DC and AC values are not exactly equal to one another. However, in spite of this, the DC values presented here will give an indication of the heating produced by our nanoparticles, and how it is affected by the temperature of the shell evaporator. This comparison is plotted in Figure 35.

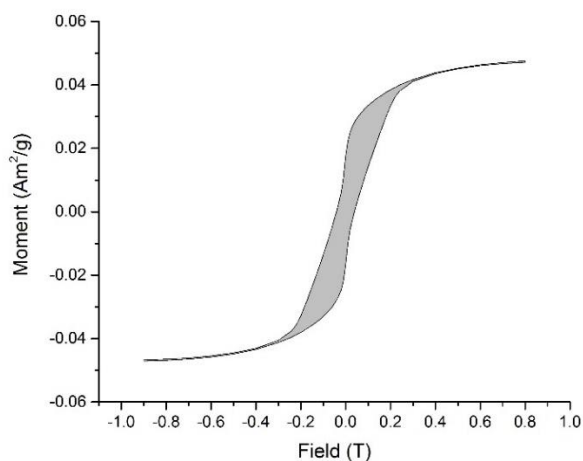


Figure 34 – Example polygon area measurement for the 1137.7 ± 43.2 °C pure Fe sample at 300 K. The grey shaded section indicates the absolute measured area of the polygon and what is plotted in Figure 35.

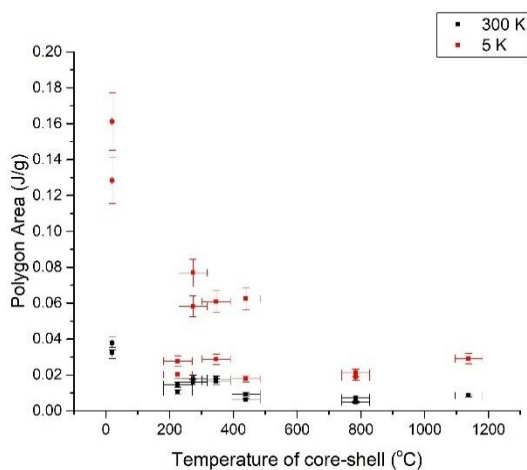


Figure 35 – Polygon areas of the hysteresis curves from the pure Fe samples plotted in Figure 30 and Figure 31.

As with the saturation magnetisation values, the area of the hysteresis curves, decreases with increasing evaporator temperature. This relationship is more drastic with samples measured at 5 K than those at 300 K, although both data-sets rapidly converge to low values with an increase in core shell evaporator temperature.

3.4 Discussion

From the M-H curves in Figure 30 and Figure 31, it is clear that the pure Fe nanoparticles produced within our system are not superparamagnetic, but “blocked.” This is evidenced from the hysteresis curves shown in these plots. It is also important to note that the behaviour does not drastically change in this respect from 5 K to 300 K.

The bulk value for the atomic moment in Fe is $2.2\mu\text{B}/\text{atom}$, which equates to a saturation magnetisation of $0.22 \text{ Am}^2/\text{g}$, which is below the value measured for the room temperature sample ($0.262 \pm 0.026 \text{ Am}^2/\text{g}$). At higher core shell evaporator temperatures, the magnetisation saturation values of our nanoparticles drop and could be due to partial oxidation. However, it is known that partial oxidation in Fe nanoparticles can lead to exchange bias. This would affect the hysteresis curves by shifting them along in the x-axis, which is not observed in Figure 30 or in Figure 31, suggesting that this may not be the case. This, however, does not rule out the possibility of a magnetic Fe-oxide, with a lower magnetic moment than that of pure Fe.

This decrease in saturation magnetisation could also be due to particle shape, as we have discovered in the first part of this chapter that heating significantly alters the geometry factor of the nanoparticle samples. This is further supported by Atkas, et al., (2015) who found heating nanoparticles decreased the MRI relaxivity.

It is also true that anisotropy, which is shape dependent, does affect the shape of M-H curves between remanence and saturation magnetization and therefore could directly affect the particle heating. This suggests that further studies are needed to clarify these points, however it is clear that the room temperature nanoparticles have saturation magnetisations that are at least as good as bulk Fe.

An interesting extra experiment would be to use an AC magnetometer to give hysteresis loops with varying maximum magnetic field applied, as the nanoparticles may well have higher SAR values with a lower magnetic field since this allows the frequency of the applied magnetic field to be increased, as long as the product of field and frequency remains below the Atkinson-Brezovich limit, $H_o \times f, = 4.85 \times 10^8 \text{ Am}^{-1} \text{ s}^{-1}$ (Atkinson, Brezovich, & Chakraborty, 1984) - see *Chapter 3: Magnetic Nanoparticle Theory and Applications* for more information.

4. Heating Data

4.1 Introduction

A third technique for analysing our nanoparticles is to use an RF field to stimulate the production of heat, then to measure this heating directly with an infrared camera. This is a novel method of analysis, giving information on the heat output of the sample in a manner not investigated previously. We prepared samples consisting of Fe nanoparticles within a matrix of Ag, a buffer of 20 nm Ag and a cap of > 50 nm Ag. The samples, as with the magnetometry samples, were prepared with 10 % volume fraction of Fe to Ag. Additionally, samples of Fe nanoparticles in SiO and Ge matrices were also prepared. Finally, the Ag containing samples were then sprayed with black paint to improve the emissivity as Ag is notorious for a mirror-like shine – thus making any infrared measurements almost impossible.

To prepare these samples, the glass substrates (size 24 mm x 24 mm x 1 mm) were positioned in line with the Fe beam as well as the thermal evaporator so that both Fe and matrix material co-deposited onto the glass (see *Chapter 2: Experimental Methods*). The thermal evaporator crucible was loaded with the material of choice, and the crucible was warmed until the material evaporated into an atomic vapour. The beam from the evaporator was aimed at the sample holder below the horizontal Fe beam, angled 45° upwards.

4.2 Results

The initial heating tests were carried out on: a pure Ag sample (of 254.0 nm thickness), a sample consisting of 4 % volume fraction (VF) Fe in an Ag matrix (of 107.1 nm Ag, 4.2 nm Fe, with a 20.1 nm buffer, and 24.8 nm cap), plus a sample consisting of an 8 % VF Fe in an Ag matrix (of 150.2 nm Ag, 12.2 nm Fe, with a 22.0 nm buffer, and 21.0 nm cap). These samples were then spray-coated with black paint as described above.

An alternating magnetic field with a frequency of 300 kHz and a magnitude in the range 10 mT to 80 mT was applied to each of the samples individually, and their temperatures allowed to stabilise for 20 seconds before an infrared measurement of their temperature

was taken. Figure 36 shows the temperature as a function of field amplitude for the three samples described above.

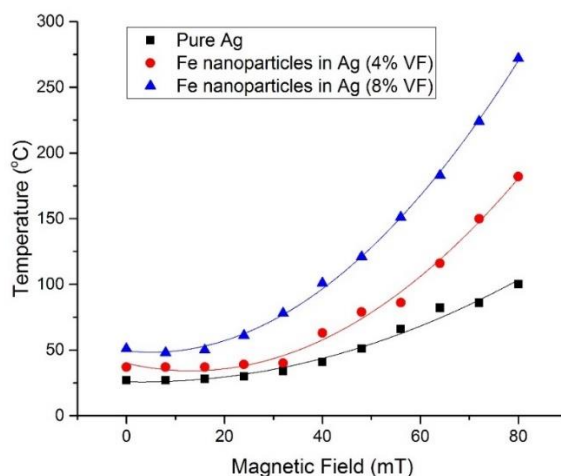


Figure 36 – Preliminary data from the pure Ag sample, 4 % volume fraction Fe in an Ag matrix, and an 8 % volume fraction Fe in an Ag matrix sample, achieved using an RF field to stimulate the production of heat, and measuring this directly with an infrared camera.

4.3 Discussion

Initial inspection of the data in Figure 36 looks promising. There certainly is an increase in the sample heating when a higher volume fraction of Fe nanoparticles is introduced. The pure Ag sample, however, also has a significant heating component due to its conducting nature, and therefore the eddy current heating that directly results from the application of an alternating magnetic field. Further to this, the pure Fe nanoparticles are more resistive than Ag, and so it cannot be said with certainty that the heating increase illustrated in Figure 36 is not just due to an increase in the eddy current heating. This means a simple subtraction of the temperature measurement of the pure Ag sample from the Fe nanoparticles in Ag sample might be inaccurate and misleading as to the nature of our nanoparticle performance.

These initial experiments were then followed by similar measurements but with SiO as the matrix material in the samples. This was chosen mainly due to its insulating properties, and therefore a potential lack of eddy current heating, but also its ease of evaporation with a thermal evaporator. Although we fully expect the oxygen within this matrix material to react with our samples and produce Fe nanoparticles with an oxide

shell (or possibly complete Fe-oxide nanoparticles), if this temperature rise can be measured, a core shell nanoparticle deposited directly from the gas phase would protect the Fe from this oxidation and therefore negate this issue.

In fact, there was almost no heating detected from the SiO matrix sample. This is probably due to the reaction of the oxygen with the iron within the sample, and/or the porous nature of SiO potentially not capping the sample effectively.

Following this, we used a matrix of germanium (Ge) to embed our Fe nanoparticles. This is also relatively easy to produce in our experimental setup and removes any interaction for our nanoparticles with oxygen from within the matrix (unlike the SiO samples). However, only rather small temperature increases were measured for this sample with the highest alternating applied magnetic field possible for over 3.5 minutes, an increase of ~ 3 °C was measured for the sample temperature. Given the error on measurement for temperature of $\sim \pm 1$ °C, this is hardly a significant heating. This heating may in fact be residual eddy current heating, and therefore not indicative of our nanoparticle behaviour.

Samples analogous to those used in the RF heating tests were also prepared for magnetometry measurements i.e., three samples consisting of Fe nanoparticles where when dispersed in a matrix of Ag, SiO, and Ge. Any changes to the embedded nanoparticles, due to alloying for example, might lead to lower saturation magnetisations, and hence reduced heating. Plots of Fe moment per g in a matrix of Ag, SiO, and Ge are

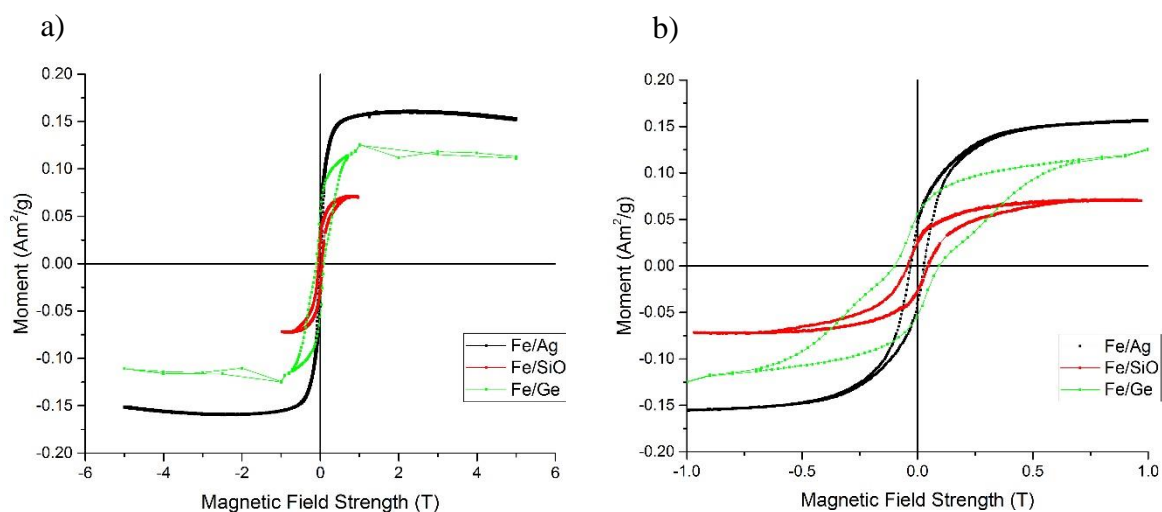


Figure 37 - Magnetometry measurements of Fe in Ag (black), SiO (red), and Ge (green). Plots in b) is the same data shown in a) but within the magnetic field range ± 1 T to illustrate the hysteresis loops more clearly.

shown in Figure 37. Figure 37 b) shows these plots within the range of ± 1.0 T to highlight the hysteresis behaviour in more detail.

As is evident from Figure 37, the Fe nanoparticles dispersed in the Ag matrix produced the largest saturation magnetisation values. Comparing the pure Ag sample with the Fe in Ag sample, there is a discrepancy in the amount of Ag present; the pure Ag sample is 254 nm thick, whereas the Fe in Ag sample has approximately half of the amount of Ag, and a low volume fraction. Hence, despite the explanation given earlier relating to the Eddy current heating, it may be possible that the temperature rise observed is partly due to nanoparticle heating in these samples.

The Fe in SiO and Fe in Ge samples were observed to have smaller saturation magnetisation values and are probably due to oxidation or alloying, respectively, of the Fe nanoparticles. As mentioned previously in section 3 of this chapter (*3. Magnetometry Data*), exchange bias produces along a shift in the x-axis. This is not observed here and therefore could indicate the creation of a magnetic (rather than anti-ferromagnetic) Fe-oxide within these samples due to the oxygen present in the SiO and perhaps a porous matrix. It also cannot be disregarded that an alloy of Fe-Ge or Fe-SiO/Fe-Si-O (or other combinations) could also have been created, thus decreasing the saturation magnetisation of our samples. This, of course, requires further investigation to determine the cause.

5. Conclusions

From the data presented here, it could be concluded that an increase of core shell temperature not only increases the particles' geometry factor by increasing the percentage of spherical nanoparticles, but an increase in core shell temperature also increases the nanoparticle overall size. It was found also to decrease their saturation magnetisation. Atkas, et al., (2015) reported the cubic nanoparticles decreased, the cuboctahedral shapes increased and the spherical shapes remained roughly unchanged as the temperature in the core shell evaporator is increased. In Figure 24, we show the cubic and cuboctahedral shapes *both* decrease in numbers, and that the spherical percentage increases as the temperature of the core shell evaporator is increased.

It has been suggested that a possible reason for the increase in core shell diameter with an increased core shell temperature, is due to Fe re-evaporating from the cru/cible ends.

This hypothesis is supported by the samples created at the hottest three temperatures and subsequently measured through TEM, as these were created at a later time than the first 9 samples, and subsequent samples were synthesised in between. This would allow for a build-up of Fe at the crucible ends, for then to be re-evaporated at these high temperature samples.

Our best performing Fe nanoparticles have a saturation magnetisation of 0.262 ± 0.026 Am²/g at 300 K and were produced at room temperature ($21 \text{ }^\circ\text{C} \pm 2 \text{ }^\circ\text{C}$) in SLUMPS. These nanoparticles have a mean diameter of ~ 18 nm, and a geometry factor of ~ 0.8 , indicating they are likely to contain mostly cuboctahedral shapes. The observation of hysteresis at 300 K shows that they are magnetically blocked. Hence any heating that they produce in an AC magnetic field should arise from hysteresis heating (which is more efficient than superparamagnetic heating - see *Chapter 3: Magnetic Nanoparticle Theory and Applications*). As mentioned previously, these nanoparticles created at room temperature and measured at 300 K within the magnetometer have a higher magnetic moment than that of bulk pure Fe (0.22 Am²/g).

Another method of investigating our nanoparticle performance, with regards to heating output, would be with AC magnetometry. This would yield hysteresis plots for our samples at differing magnitudes of applied magnetic field. From this an appropriate frequency could be selected (ensuring their combination remains below the Atkinson-Brezovich limit, $H_o \times f, = 4.85 \times 10^8$ Am⁻¹ s⁻¹ (Atkinson, Brezovich, & Chakraborty, 1984), see *Chapter 3: Magnetic Nanoparticle Theory and Applications*), and the maximum heat output, or the SAR value, for each sample could be calculated.

Chapter 5: Fe@Cu Studies

1. Introduction

As the previous chapters have outlined, the aim of this research is to produce the highest performing nanoparticles for use in magnetic nanoparticle hyperthermia (MNH), MRI, and magnetic particle imaging (MPI). For MNH, nanoparticles with high saturation magnetisation, and the ability to produce heat through hysteresis curves are the most suitable. This means small single- or multi-domain nanoparticles with a core of Fe is appropriate (for further information see *Chapter 3: Magnetic Nanoparticles Theory and Medical Applications*).

Fe was chosen as the main core material of the nanoparticles, and the reasons are outlined previously in *Chapter 4: Pure Fe Studies*. To briefly summarise: ease of creation within our laboratory, high magnetic moment, and ability to produce heating through hysteresis. Due to the inevitable oxidation of Fe in various ambient conditions, and the negative affect this has on nanoparticle performance, the need for a protective shell is apparent. This chapter details the investigations undertaken for a Cu shelled, Fe core nanoparticle (notation: Fe@Cu).

Cu was chosen as a possible shell material due to its previous success as a shell material by this research group for Fe particles prepared using LUMPS, another particle source in the research group which produces smaller nanoparticles than synthesised in SLUMPS (Baker, et al., 2000). However, Cu-oxide is not biocompatible and so another outer layer must be present before this can be realised in vitro. This may seem counter-intuitive, but previous investigations with other biocompatible materials for the shell have met with little success and are detailed in the following chapter, *Chapter 6: Other Core Shell Studies* which includes information on Ag, Al, and Mg as shell materials.

To prepare Fe@Cu samples, SLUMPS is set up as outlined in *Chapter 2: Experimental Methods* and *Chapter 4: Pure Fe Studies*, but instead of an empty crucible, the core shell evaporator is loaded with ~ 1 g of Cu. The power supplied to the crucible can be increased up to a maximum of ~ 300 W, producing a temperature from ~ 21 °C (room temperature) up to ~ 1200 °C. The vapour pressure of Cu within the crucible can be estimated from its temperature (Leicester University, 1990). A Cu vapour pressure of 10^{-5} mbar is achieved

at a temperature of ≥ 900 °C. Pressures P_3 and P_4 in SLUMPS are $\sim 10^{-4}$ and 10^{-5} mbar, respectively. The temperatures used in this chapter encompasses Cu vapour pressures from $< 10^{-11}$ mbar to $\sim 10^{-3}$ mbar. The samples produced are at varying powers, and therefore temperatures, to investigate the relationship between crucible temperature and Cu coverage of the Fe nanoparticles in the sample.

This chapter investigates the size, shape, composition, and magnetic properties of the Fe@Cu samples produced at various core shell evaporator temperatures. The effect that the shape change has on the nanoparticles' magnetic behaviour is also examined. More specifically, the saturation magnetisation values are obtained from hysteresis curves measured from nanoparticle samples in magnetometry experiments. The shape changes are investigated with TEM imaging, and the correlating magnetic properties are explored with SQUID magnetometry via our collaborators at Ciudad, Spain. 9 TEM samples and 3 magnetometry samples have been investigated here, prepared with the core shell evaporator operating at various temperatures.

Ultimately, this chapter investigates whether an addition of a Cu shell in our experimental set-up is feasible, and if so, how this Cu shell affects the size, shape, and magnetic properties of our samples, and how these characteristics are altered with a change in crucible temperature.

All 12 (9 TEM and 3 magnetometry) samples in this chapter have been produced in SLUMPS under the same conditions as outlined in *Chapter 2: Experimental Methods*. That is, with the sputter magnetron operating between 10 W and 20 W, and with Ar gas inputted into the system at the sputter head giving pressures of P_1 30 mbar and $P_3 \sim 2 \times 10^{-4}$ mbar. The core shell evaporator was operated between 2.0 A and 6.0 A, with Cu pellets inserted into the crucible, and the Fe@Cu nanoparticles were deposited onto TEM grids or Si wafers.

The nanoparticle samples made for SQUID magnetometry were produced in an Ag matrix and can be assumed to be oxidation free as they are adequately capped with Ag (> 50 nm cap).

2. TEM Data

2.1 Introduction

All samples in this section were created using the sputter source outlined in *Chapter 2: Experimental Methods* and deposited on Cu TEM grids within the vacuum system. As described previously, the TEM samples were unavoidably exposed to air in transit between the deposition source and the JEOL 2100 TEM at Leicester, or the JEOL 2200 TEM at York; this therefore means they all have a thin oxide shell, potentially a Cu-oxide shell. The TEMs were utilised to obtain 2-D images of our nanoparticles and some example images are shown in Figure 38.

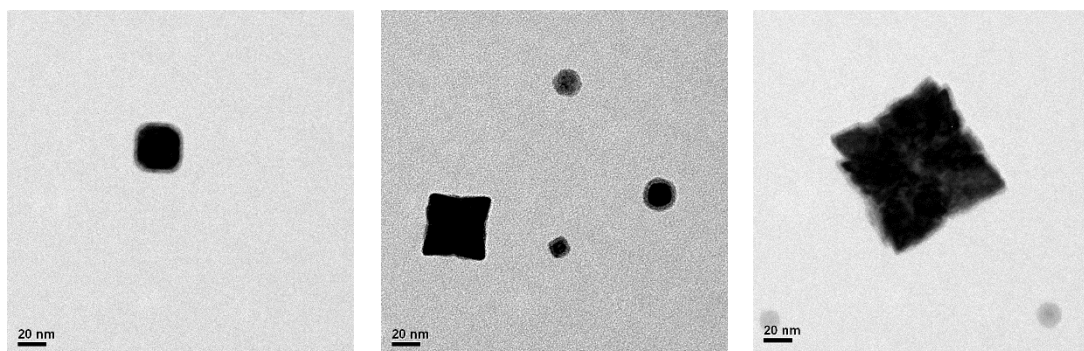


Figure 38 - TEM images of the Fe@Cu nanoparticles. Scale bar for each image is shown in the bottom left of the images.

Figure 38 shows TEM images of the pure Fe@Cu nanoparticles. The scale bar for each image is shown in the bottom left of the images. The coverage across the TEM grid is achieved by depositing approximately 2 - 3 Å of Fe@Cu, as per the pure Fe samples outlined in *Chapter 4: Pure Fe Studies*.

In this section, TEM images are utilised to produce frequency plots for the nanoparticle shapes and, overall sizes for each sample produced at the varying core shell evaporator temperatures. The following section (*4. EDX Data*) explains the EDX measurements and maps the 2-D spread of Cu across the nanoparticle surface.

2.2 Analysis Methods

As in *Chapter 4: Pure Fe Studies*, analysing the shape of the nanoparticle was achieved by utilising a geometry factor, which is extracted from the 2-D TEM image of the nanoparticle. The geometry factor is calculated by dividing the true area of the

nanoparticle measured from the TEM image, by the maximum area possible if the nanoparticle were a perfect circle. To obtain this information, the analysis package ImageJ was utilised as it has the capability to measure the Feret diameter. The same analysis method as used in *Chapter 4: Pure Fe Studies* has been applied here. To reiterate, this measurement gives 0.63 for a perfect square and 1.0 for a perfect sphere and allows for good judgement of the 2D shape of the nanoparticle. More information on the Feret diameter, the geometry factor, and how ImageJ measures the area of the nanoparticles is given in the section 3.2 *Analysis Methods* of *Chapter 4: Pure Fe Studies*.

As before, any geometry factor between 0.4 and 0.7 is classed as a square or a truncated square, and the particle assumed to be cubic. Between 0.7 and 0.8 the particle is categorised as a cuboctahedral and above 0.8, the nanoparticle is assumed spherical. Any area measurements quoted below refer to the true area of the nanoparticle from TEM images, as measured with ImageJ. A cubic nanoparticle is assumed to look like a square in a 2D. A cuboctahedral/cuboctahedron is a polyhedron with 8 triangular faces and 6 square. This means its geometry factor will be above 0.63, and below 1.0. To account for truncated squares, the value assigned to cuboctahedral nanoparticles is given between 0.7 and 0.8, with spherical shapes obtaining a geometry factor of > 0.8 .

This chapter starts with data obtained from TEM imagery, outlining the overall size and shape distributions of the nanoparticles. The temperatures that the Fe nanoparticles were subjected to in the Cu-coating cell during deposition are included in Table 4. Alongside bright-field TEM imagery, EDX was also utilised to verify the percentage of copper in each sample, and to pinpoint where this copper is localised. This is detailed in *Section 4. EDX Data*.

Core Shell Temperature (°C)	Number of Nanoparticles Analysed
218.0 ± 44.9 °C	100
316.8 ± 44.6 °C	111
441.6 ± 44.2 °C,	100
704.9 ± 43.6 °C	76
777.4 ± 43.5 °C	248
895.4 ± 43.3 °C	98
994.1 ± 43.1 °C	80
1052.4 ± 43.2 °C	96
1130.6 ± 43.2 °C	239

Table 4 – The temperatures that the Fe nanoparticles were subjected to in the Cu-coating cell during deposition and the number of nanoparticles analysed per dataset.

2.3 Results

As in *Chapter 4: Pure Fe Studies*, the geometry factor for each sample was separated into appropriate bins and plotted into a histogram. These histograms were then fitted with a 2-parameter Weibull distribution. An example of this fitting is provided in Figure 39, for the sample produced at 1130.6 ± 43.2 °C.

The Weibull distribution is very useful for fitting data that follow an atypical normal distribution, with a skew in either direction. Mainly, it is used for right-skewed data, such as that shown in Figure 39 and it follows a stretched exponential distribution. The probability function of a Weibull is as follows,

$$P(x|a,b) = ba^{-b} x^{b-1} e^{-\left(\frac{x}{a}\right)^b},$$

where a is the scale parameter and b the shape parameter. The scale parameter indicates the spread of the distribution, where a large number indicates a large spread. The shape parameter gives an indication on the shape of the distribution. For example, a b value between 3 and 4 gives a bell-shaped curve, not dissimilar to a normal distribution. A value below this gives a left-skewed plot, much like a lognormal, whereas a value above 4 gives a right-skewed dataset, as is observed in the data presented in Figure 39, which has a shape parameter value of 9.48.

Fitting the measured distributions to the Weibull distributions allows one to assign a mean value for the geometry factor, along with a \pm one sigma value, for each core shell temperature.

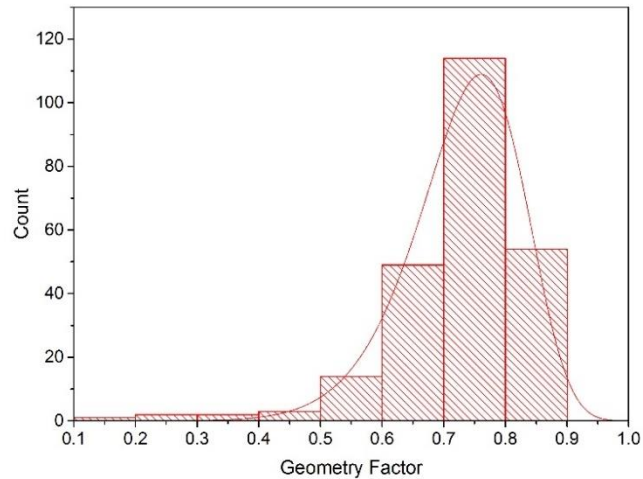


Figure 39 - Fe@Cu sample produced at 1130.6 ± 43.2 °C with a mean geometry factor of 0.730 ± 0.009 (1 standard deviation) with a scale parameter value of 0.770 and a shape parameter of 9.48 from the Weibull fitting (red line).

Figure 40 plots this geometry factor (\pm one sigma) from the Weibull fits for each of the 9 samples produced for TEM imagery and includes dotted lines to indicate the separation of the 3 regions of interest: cubic, cuboctahedral, and spherical.

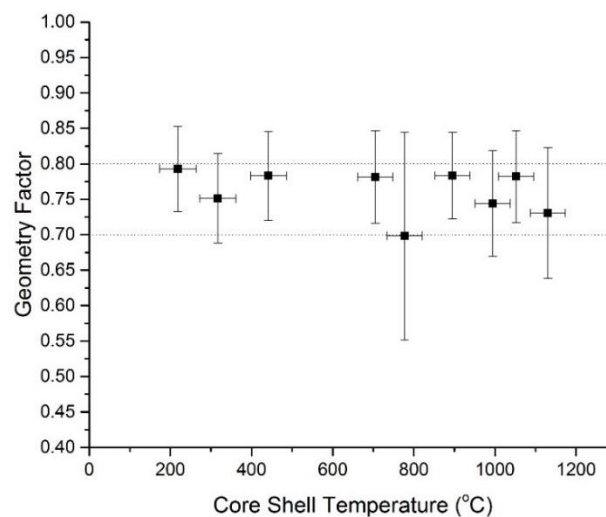


Figure 40 – Geometry factor for the 9 TEM samples produced with the core shell evaporator loaded with ~ 1 g Cu. The dotted lines indicate the separation of the cubic (0.4 – 0.7), cuboctahedral (0.7 – 0.8), and spherical (0.8 – 1.0) regions. The values come from Weibull fits of the raw data with \pm one sigma error bars.

Figure 40 implies there is not a significant shift in geometry factor, and therefore shape change, as the temperature of the core shell evaporator is increased. All the mean values

plotted here lie within the cuboctahedral range, with the one sigma errors often extending out into the cubic and spherical regions. This implies that most of the nanoparticles produced in these samples had a roughly hexagonal appearance when viewed as 2-D shapes in the TEM images. Comparison of the Fe@Cu samples and the pure Fe samples (more information is included on the pure Fe sample set in *Chapter 4: Pure Fe Studies*), is in Figure 41.

As mentioned in the previous chapter (*Chapter 4: Pure Fe Studies*), the geometry factor of the pure Fe samples was found to increase into the spherical regime with increasing temperature of the core shell evaporator. Here, however, the geometry factor of the Fe@Cu samples remains within the cuboctahedral range. This indicates that the addition of Cu into the core shell evaporator impacts the relationship between geometry factor and temperature. The possible reasons for this are investigated in more detail within the EDX and magnetometry sections of this chapter.

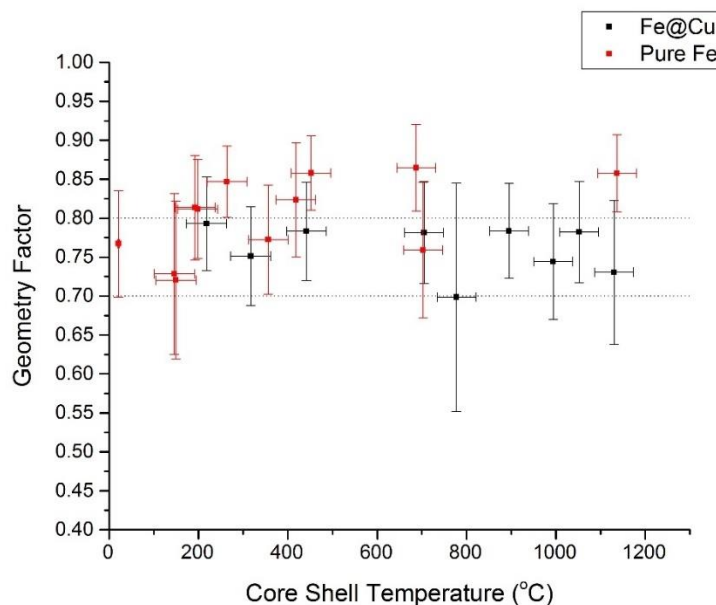


Figure 41 - Geometry factor for the 9 Fe@Cu TEM samples (black) and the 12 pure Fe TEM samples (red) produced with the core shell evaporator. The dotted lines indicate the separation of the cubic (0.4 – 0.7), cuboctahedral (0.7 – 0.8), and spherical (0.8 – 1.0) regions. The values come from Weibull fits of the raw data with \pm one sigma error bars.

Figure 42 plots the percentage of cubic, cuboctrahedral, and spherical shaped nanoparticles against the core shell temperature to investigate the trends in the shape change that may be overlooked when plotting only the mean geometry factor (\pm one sigma error bars) as in Figure 40. Figure 42 shows is an increase in the percentage of cubic nanoparticles, a decrease in the percentage of cuboctrahedral nanoparticles, as well

as a decrease in the spherical percentage, as the core shell evaporator temperature is increased. These trends differ from those of the pure Fe samples (see Figure 24 in *Chapter 4: Pure Fe Studies*) where the percentage of cubic nanoparticles drastically decreases, and the spherical percentage increases with increased core shell temperature. In both cases, the cubo-octahedral percentage decreases at a similar rate within the temperature ranges but starts at higher values within the Fe@Cu samples (~ 70% to ~ 45% for the Fe@Cu samples vs ~ 40 % to ~ 20% for the pure Fe samples).

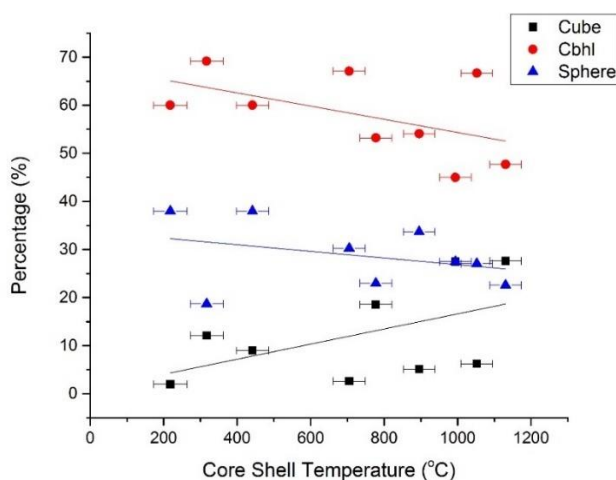


Figure 42 – The percentage of cubes (geometry factor 0.4 -0.7, black squares), cubo-octahedrals (0.7 – 0.8, red circles) and spheres (0.8 - 1.0, blue triangles) versus the core shell temperature when loaded with ~ 1 g of Cu.

Figure 43 illustrates the nanoparticle diameter (\pm one sigma error bars) from lognormal distributions of the raw area measurements of the ImageJ images from TEM images. This is from histogram plots such as in Figure 44. Similar plots and distributions were fitted to all 9 TEM samples analysed in this section and plotted in Figure 43. This plot does not indicate any particular trend between the nanoparticle diameter and the core shell evaporator temperature. Comparison with the pure Fe samples is given in Figure 45.

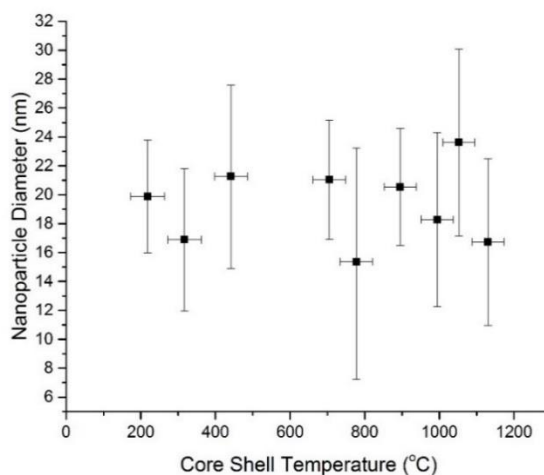


Figure 43 - The diameter of each Fe@Cu 2-D nanoparticle vs the temperature of the core shell evaporator. Plotted values are the means for the sample obtained from lognormal fitting with one sigma error bars.

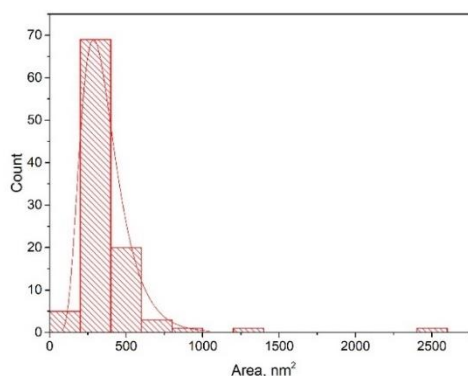


Figure 44 – Example histogram and lognormal fitting for the 218.0 ± 44.9 °C Fe@Cu sample.

In Figure 45, there is no discernible difference between the pure Fe samples and the Fe@Cu samples up to a core shell evaporator temperature of ~ 700 °C. Above this temperature, the two sample sets' behaviour bifurcates. The pure Fe samples increase in diameter up to ~ 40 nm, whereas the Fe@Cu samples do not change to any discernible degree. This is surprising as previous experiments within our laboratory indicated that an increase in core shell evaporator temperature (when loaded with a material of choice), increased nanoparticle size, probably due to an increase in shell thickness. As with the geometry factor, the addition of Cu into the core shell evaporator appears to directly impact the nanoparticle properties with regards to an increasing core shell evaporator temperature.

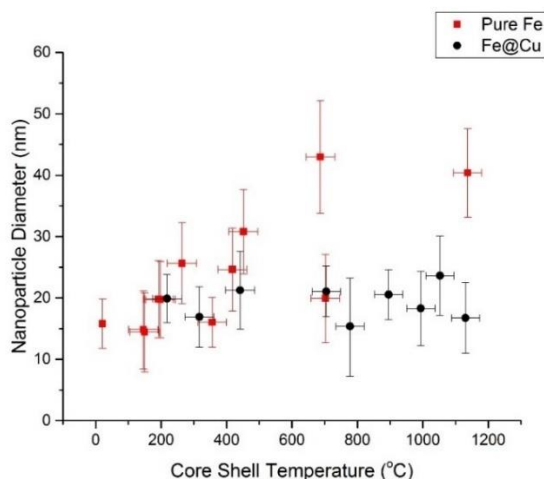


Figure 45 – Comparison of nanoparticle diameter for the 12 pure Fe TEM samples (red squares) and the 9 Fe@Cu TEM samples (black circles).

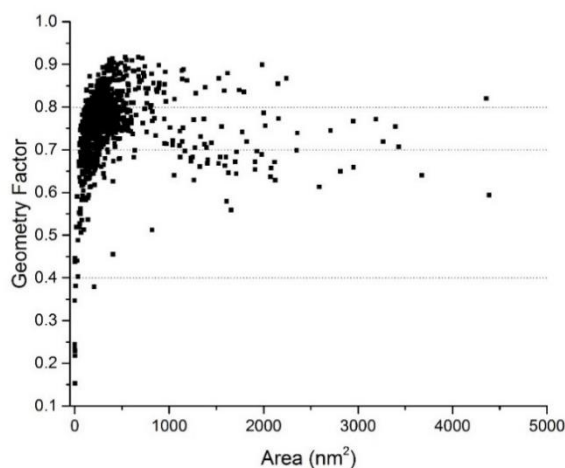


Figure 46 – Geometry factor versus area for all 1148 Fe@Cu nanoparticles analysed in this dataset. The dotted lines indicate the separation of the cubic (0.4 – 0.7), cuboctahedral (0.7 – 0.8), and spherical (0.8 – 1.0) regions.

After investigating the effect of core shell evaporator temperature on nanoparticle size, the link between geometry factor and 2D nanoparticle area (nm^2) was investigated.

Figure 46 shows the true area values from the 2D TEM images plotted against the geometry factor for these Fe@Cu samples. As with the pure Fe nanoparticles, the Fe@Cu nanoparticles appear to cluster in the top-left of the plot. The vast majority are within an area range of 0 – 600 nm^2 and a geometry factor between 0.6 – 0.9, with few nanoparticles residing outside of this range. There are very few large (> 1000 nm^2) nanoparticles with low geometry factor (< 0.8), suggesting not only that large cubic nanoparticles are uncommon, but also large cuboctahedral nanoparticles

Figure 47 investigates the area and geometry factor relationship in more detail by splitting each of the area bins into its corresponding shape categories. Figure 47 a) shows the majority of the nanoparticles are within the two lowest area bins 0 – 200 nm² and 200 – 400 nm² corresponding to 30.3% and 46.3% respectively, and are heavily dominated by cuboctahedral shapes: 61.3% and 60.7%, respectively. The number of nanoparticles with a 2D area above 600 nm² drops considerably when compared with the pure Fe samples in *Chapter 4: Pure Fe Studies*, Figure 29, and Table 3 (26.5% to 11.5%).

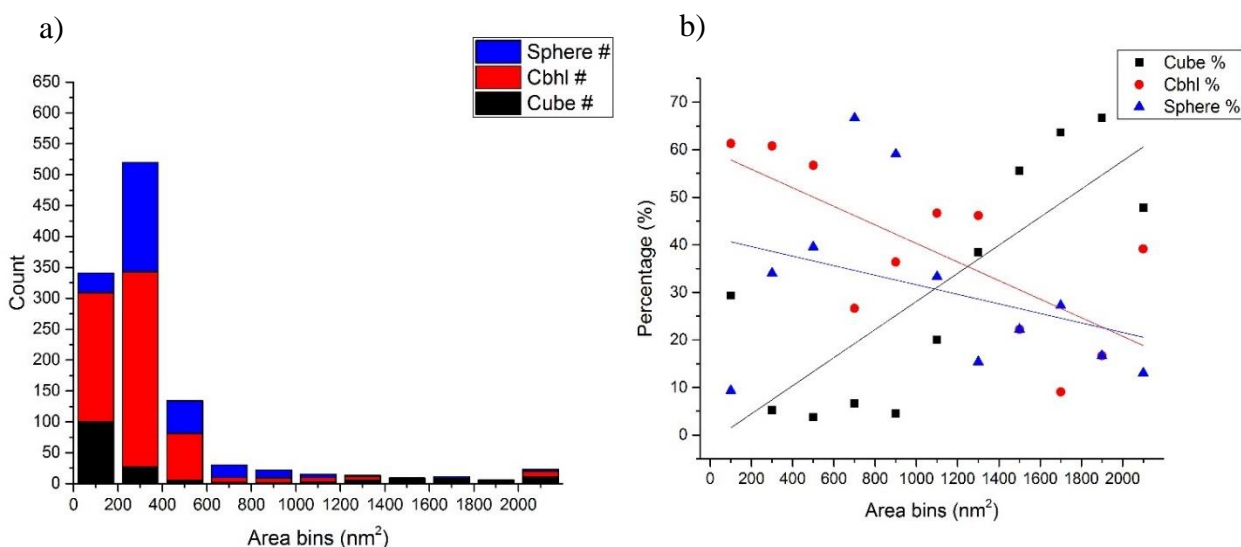


Figure 47 – Number of spheres (blue), cuboctahedrals/cbhl (red), and cubic (black) Fe@Cu nanoparticles in each area bin (200 nm²) in size.

Figure 47 b) shows the percentage of cubes, cuboctahedrals, and spheres for each area bin. This plot is in stark contrast with the corresponding plot for the pure Fe samples in *Chapter 4: Pure Fe Studies* (Figure 29). For the Fe@Cu samples presented here, the percentage of cubic nanoparticles significantly increases in the higher area bins, with the percentage of cuboctahedrals and spheres decreasing for larger areas. The full breakdown of the counts and percentages are included in Table 5, below.

For nanoparticles of 1400 nm² or more in area, cubic nanoparticles tend to dominate: 27 out of a total of 49 nanoparticles, or 55.1 %. This is in stark contrast to the pure Fe sample where above 1400 nm² there are only 3 cubic nanoparticles out of a total of 116 nanoparticles, corresponding to 2.6 %.

Area bins, nm ²	Cube counts	Cuboctahedral (cbhl) counts	Sphere counts	Total number of Nanoparticles per area bin
0-200	100 (29.3%)	209 (61.3%)	32 (9.4%)	341
200-400	27 (5.2%)	316 (60.7%)	177 (34.0%)	520
400-600	5 (3.7%)	76 (56.7%)	53 (39.6%)	134
600-800	2 (6.7%)	8 (26.7%)	20 (66.7%)	30
800-1000	1 (4.5%)	8 (36.4%)	13 (59.1%)	22
1000-1200	3 (20.0%)	7 (46.7%)	5 (33.3%)	15
1200-1400	5 (38.5%)	6 (46.2%)	2 (15.4%)	13
1400-1600	5 (55.6%)	2 (22.2%)	2 (22.2%)	9
1600-1800	7 (63.6%)	1 (9.1%)	3 (27.3%)	11
1800-2000	4 (66.7 %)	1 (16.7%)	1 (16.7%)	6
>2000	11 (47.8%)	9 (39.1%)	3 (13.0%)	23

Table 5 - Percentages of cubic, cuboctahedral, and spherical Fe@Cu nanoparticles in each area bin, plus the total counts per area bin. This data is plotted in Figure 47.

2.4 Discussion

Figure 40 shows there is no clear change in geometry factor with an increasing core shell evaporator temperature for the Fe@Cu samples. As can be seen in Figure 41, where the geometry factor of the Fe@Cu samples and the pure Fe samples is compared, the geometry factor of the pure Fe samples tends to increase into the spherical regime with an increased temperature of the core shell evaporator. The Fe@Cu samples' geometry factor, however, remains within the cuboctahedral range.

This suggests that the addition of Cu into the core shell evaporator alters the nanoparticles when subjected to the higher temperatures. As is investigated in the EDX section of this chapter, the possibility of both Cu shell formations and of alloying between Fe and Cu need to be considered.

As mentioned in the previous chapter, surface energy is a key consideration in material science. When the temperature of a particle is increased, the cohesive force binding the atoms can be reduced due to vibrations. However, the surface energy can be altered by the addition of other elements or contaminants. The addition of such changes the balance

of such forces and can possibly reduce the net inward force. A contaminant, such as copper which has a lower surface energy could also have a similar impact.

This would ultimately change the surface energy of the nanoparticles and could mean that a higher temperature is now required to overcome the energy barrier to produce more spherical nanoparticles than with the pure Fe alone. This is supported by Figure 42, where the percentage of cubes does not decrease as with increasing temperature with the pure Fe samples in the previous chapter. Rather, they actually increase with an increased core shell temperature, perhaps due to the higher percentage of Cu present. The surface energy of bulk fcc Cu (111) is 1409 J/m^2 (Zhang, Ma, & Xu, 2004), far below that of bulk Fe (2123 J/m^2), thus the addition of Cu to the surface will decrease the surface energy of the nanoparticle. This may explain why there are far fewer cuboctahedral and spherical nanoparticles at higher core shell temperatures, and higher numbers of cubic nanoparticles in this Fe@Cu sample set, in comparison to the pure Fe samples, as the surface energy has been drastically reduced with the addition of Cu, whether as a shell or as an alloy with the Fe. These possibilities are investigated further in the following section, *EDX data*.

The nanoparticle diameter and temperature relationship presented in this chapter again differs to what was observed in the previous chapter, *Chapter 4: Pure Fe Studies*. The two datasets were plotted together in Figure 45 to clearly show any differences. The two datasets do not appear to differ greatly until $\sim 700 \text{ }^\circ\text{C}$ where the two bifurcate with the pure Fe nanoparticles increasing in diameter up to $\sim 40 \text{ nm}$ and the Fe@Cu samples remaining below 30 nm . It should be noted that only 2 samples of pure Fe are above these values, and further samples should be synthesised and their relationships investigated before assuming that this is always the case. As was seen in Figure 47, where the nanoparticle area and geometry factor relationship were investigated by splitting each area bin into its corresponding shape categories across all temperatures, the majority of the nanoparticles are within the two lowest area bins $0 - 200 \text{ nm}^2$ and $200 - 400 \text{ nm}^2$ with 30.3% and 46.3% respectively of the total nanoparticle count. These are heavily dominated by cuboctahedral shapes with 61.3% and 60.7% , respectively. The number of nanoparticles with a 2D area above 600 nm^2 drops considerably when compared with the pure Fe samples in *Chapter 4: Pure Fe* from 26.5% to 11.5% .

The pure Fe samples suggested that size increase at high core shell evaporator temperatures could be due to Fe at the end of the core shell re-evaporating. This originates from previous deposition use. Here, however, with the crucible loaded with Cu, samples produced at high temperatures would give a Cu vapour pressure much higher than the Fe vapour from each end of the evaporator. Any Fe vapour evaporating from the end of the core shell crucible is not likely to penetrate the length of the crucible. From the EDX data detailed in the following section, it was also seen that there is a small amount of Cu present in the deposition chamber, supporting this hypothesis that the size increase from this re-evaporating Fe is small.

The following section investigates the Cu content in the nanoparticle samples and whether a clear Cu shell is present (or a Cu_xO_y shell as the samples are inevitably exposed to air in these investigations), or perhaps some Fe-Cu alloy.

3. EDX Data

3.1 Introduction

EDX data is invaluable in determining the material composition of our samples, including whether or not a complete shell has been formed around the pure Fe core. Here, the data presented gives the atomic percentage of Cu, Fe, O, and Ni present in the samples. The TEM grids used for this analysis are made of Ni rather than Cu as used in the previous chapter, *Chapter 4: Pure Fe Studies*. This is because signal from the nanoparticles would be completely masked by a large background from a Cu grid.

3.2 Analysis Methods

As outlined in *Chapter 2: Experimental Methods*, EDX measures the characteristic x-rays emitted from the nanoparticles within the TEM. These x-rays are indicative of the elements present within the sample and are used here to investigate the presence of Cu on our nanoparticles, and, in particular, if a complete shell of Cu has been formed.

“Point-and-shoot,” line scans, and mapping are utilised in this section to give information on the elemental composition of our samples. Point-and-shoot EDX allows the user to select an area of the sample and yields the weight percentage plus the atomic percentage

of each of the characteristic x-ray lines. The user can also select which elements they expect to be the most likely to aid the program to select which peaks correspond to which element line.

Line scans, as one might expect, allow the user to draw a line across the sample to give information on the characteristic x-rays originating along this line. This is particularly useful here when investigating the possibility of a complete Cu shell, as the percentage of Cu at the edges of the 2D image would be much larger than at the centre of the nanoparticle if a solid shell was formed, with hardly any Fe signal expected from the edge of the nanoparticle in the TEM image.

Mapping allows the user to select an area of the sample and produce a 2-D map of the emitted x-rays associated with a particular element. A map of the distribution of Cu on and surrounding our nanoparticles will ultimately aid our conclusions as to whether or not the Cu material has indeed formed a complete shell around the Fe core.

Four of the samples analysed in the previous section were studied using EDX: 316.8 ± 44.6 °C, 777.4 ± 43.5 °C, 994.1 ± 43.1 °C, and 1130.6 ± 43.2 °C. Due to the time-consuming nature of EDX data collection and analysis, only one nanoparticle for each of these temperatures has been analysed in detail with point-and-shoot EDX, bar the 316.8 ± 44.6 °C sample, which has data on 4 separate nanoparticles.

The point-and-shoot EDX atomic percentage values given in this section are scaled as if the only signals are from Fe and Cu, to investigate their percentages relative to one another.

3.3 Results

Firstly, the 316.8 ± 44.6 °C sample was analysed within the TEM, and a dark field TEM image produced as in Figure 48. Indicated here are regions of interest where point-and-shoot analysis was undertaken, with the x-ray spectra for region 1 and 2 included in Figure 49. Figure 49 also identifies the elements of interest above their respective spectral lines. Dark field TEM is implemented here instead of bright field TEM due to its greater contrast.

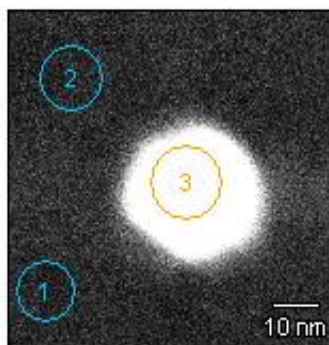


Figure 48 – Dark field TEM image of an example Fe@Cu nanoparticle created with the shell evaporator operating at 316.8 ± 44.6 °C. The numbers represent three of the areas measured with point-and-shoot EDX.

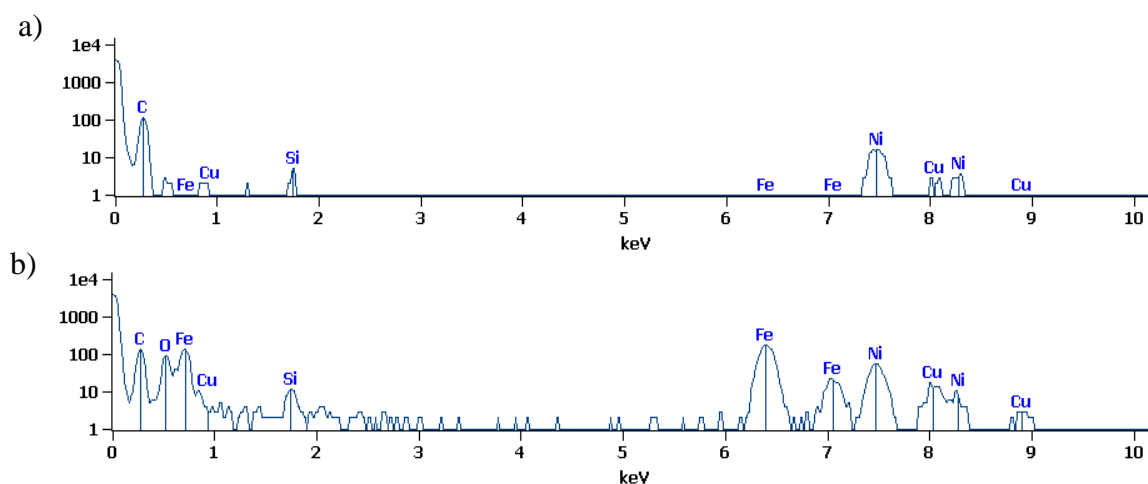


Figure 49 - 2 regions of EDX spectra (EDXS) TEM analysis of the Fe@Cu nanoparticle in Figure 48, with a) referring to the background, point 1, and b) the area within the particle, denoted with the number 3 in Figure 48.

Figure 49 shows lines for C, O, Fe, Cu, Ni and Si. The Si is present due to the sample holder used in the TEM, the C and Ni are abundant within the TEM grid, and the Fe and Cu spectral lines are due to the nanoparticles. O is of course present due to the necessity to remove the TEM grid from our chamber to transport into the TEM, inevitably exposing it to air, and therefore O. These scans show there is definitely Cu present on the TEM grid. Comparing only the Fe and Cu atomic percentages within region 3 gives 79.04 ± 2.18 % Fe and 20.96 ± 2.38 % Cu. This indicates that a complete shell of Cu is unlikely.

This possibility of a Cu shell was investigated further with line-scans across a nanoparticle within the 316.8 ± 44.6 °C sample. These scans are given in Figure 50.

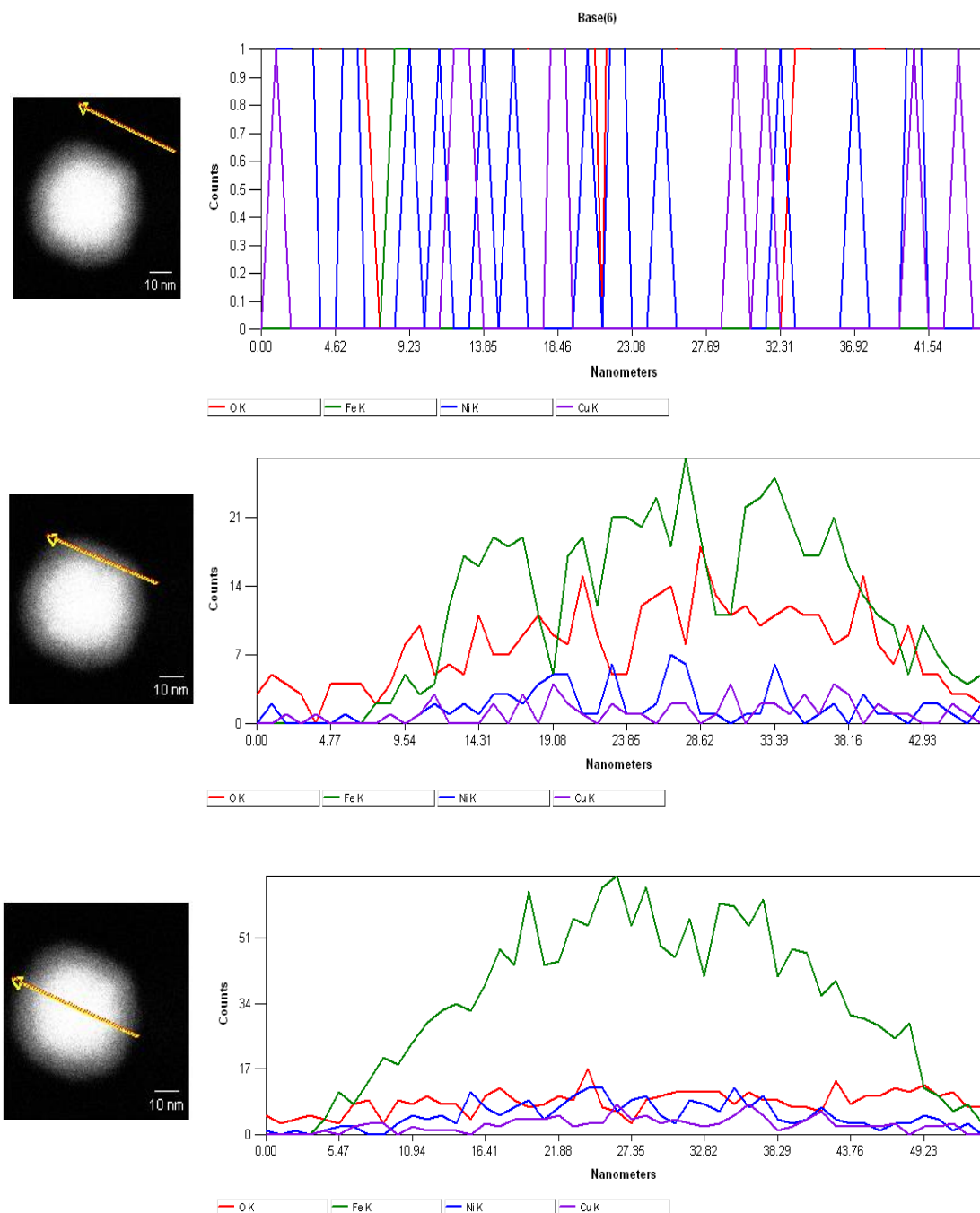


Figure 50 – Three line-scans of a Fe@Cu nanoparticle from the 316.4 ± 44.6 °C sample. Notice the increase in Fe as the line crosses the centre of the nanoparticle and the abundance of O at the surface.

Figure 50 shows 3 line-scans of a nanoparticle within the 316.4 ± 44.6 °C sample. The first line-scan is of the background, the second crosses the edge of the nanoparticle, and the third line scan crosses through the centre of the nanoparticle. The four elements shown here are O, Fe, Ni, and Cu. The Ni signal originates from the TEM grids. The line scans indicate a large increase in Fe at the edges and the centre of the particle, with more O at the edge. The Cu counts are much less than those for Fe. However, in the second and

third line scans, the Cu signal peaks in the middle of the line scan, particularly for the third scan. To investigate the Cu coverage further, EDX maps were produced.

Figure 52 shows the results of 2-D mapping for 3 nanoparticles from the 316.8 ± 44.6 °C sample, with maps of both the Fe and Cu signals. Scale bars are included in the figures.

The EDX mapping in Figure 52 shows that there is Cu largely distributed, albeit lightly, across the entire sample. This indicates that there could be some leakage of Cu from our core shell evaporator into the deposition chamber. However, the increase in Cu signal within the particle regions can be clearly seen. This may be attributed either to alloying of the Fe and Cu or a thin coating of Cu on the surface of the particle. An Fe-Cu phase diagram is included in Figure 51.

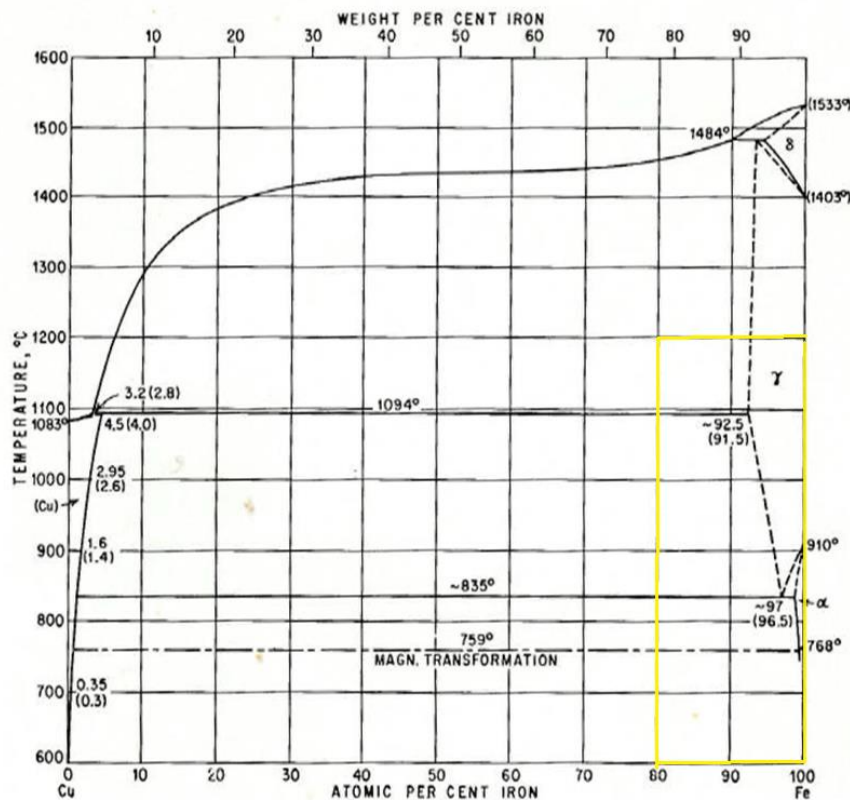


Figure 51 - Phase diagram for Fe-Cu binary alloy, with the bottom right section highlighted as this is the appropriate temperature range and percentage of Fe/Cu for these experiments. Figure from (Hansen, 1958).

Within Figure 51, a section has been highlighted as this temperature range and percentage of iron is the most relevant to the following data. As the temperature increases pure iron changes from a body centred cubic (BCC) structure (α -Fe), to a face centred cubic (FCC) structure (β -Fe), and finally back to a BCC structure (δ -Fe). When Cu is added at these temperatures, Figure 51 shows alloys of Fe-Cu can be formed.

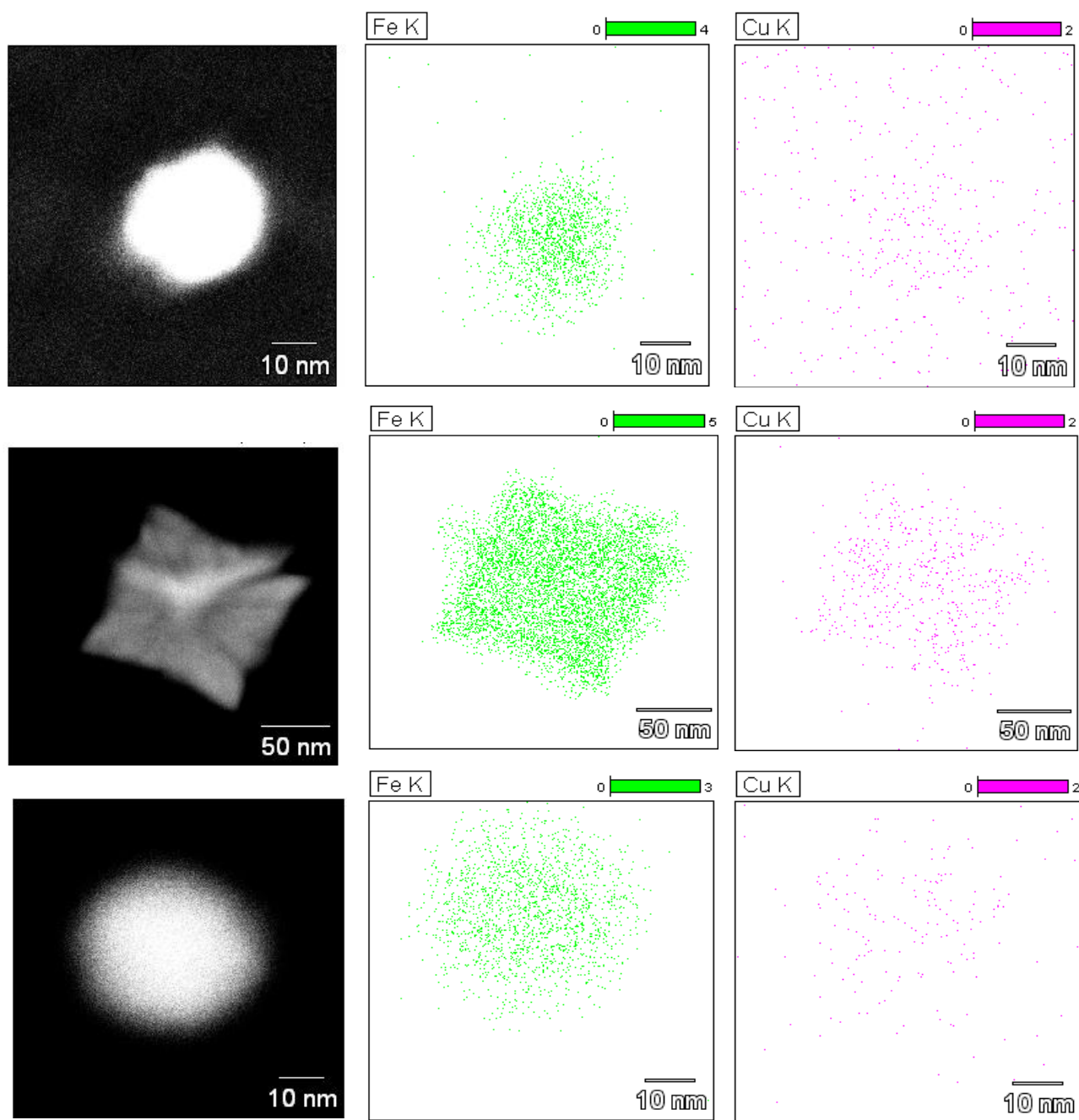


Figure 52 – EDX mapping of Cu and Fe for 3 nanoparticles in the 316.8 ± 44.6 °C sample.

Figure 54 gives the dark field TEM image of a nanoparticle from the 777.4 ± 43.5 °C sample, with Figure 53 showing the EDX spectra for regions 1 and 3, respectively.

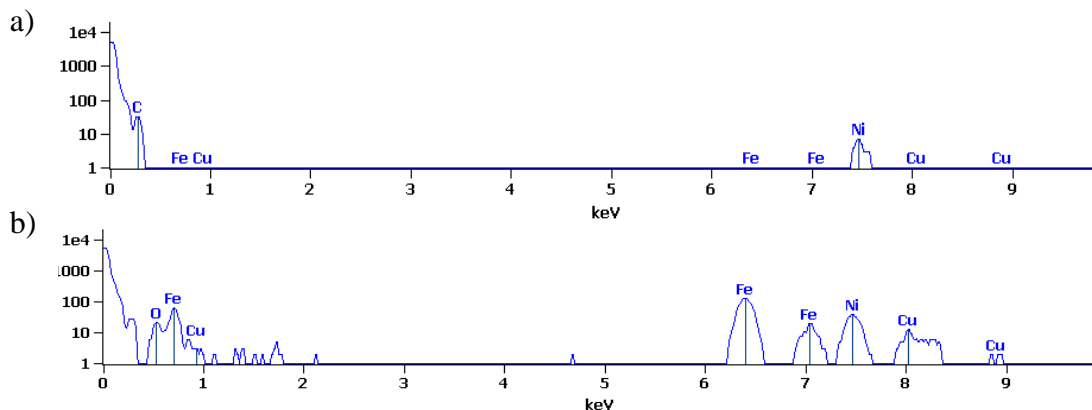


Figure 53 - 2 regions of EDXS TEM analysis of the Fe@Cu nanoparticle in Figure 54, with a) referring to the background, point 1, and b) the area within the particle, denoted by the number 3 in Figure 54.

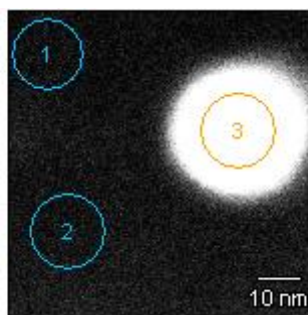


Figure 54 - Dark field TEM image of an example Fe@Cu nanoparticle created with the shell evaporator at 777.4 ± 43.5 °C. The numbers represent three of the areas measured with point-and-shoot EDX.

From the point and click EDX spectra in region 3, the atomic percentage of Fe to Cu (K lines) was measured as 92.92 ± 2.88 % Fe, 7.08 ± 1.07 % Cu. As with the previous sample, EDX maps of Fe and Cu were produced and are displayed in Figure 55.

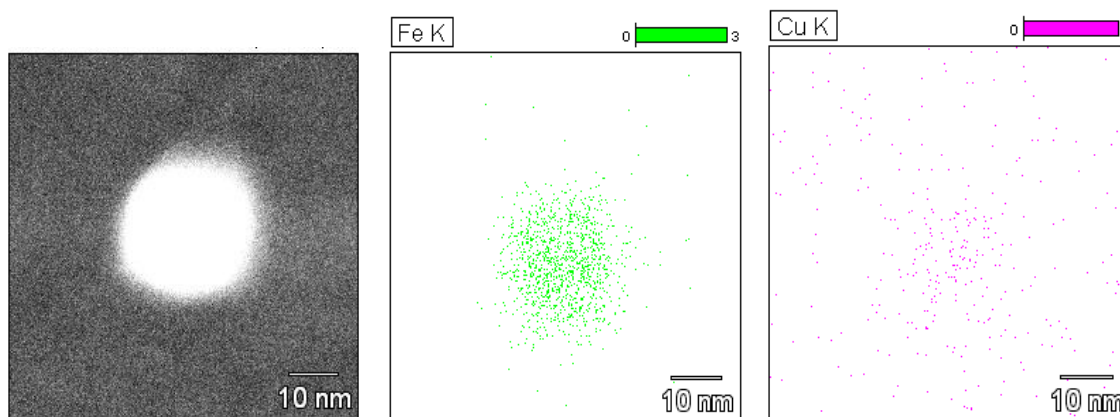


Figure 55 – EDX mapping of a nanoparticle from the 777.4 ± 43.5 °C sample. The abundance of Cu, and Fe have been highlighted in the two panels, middle and right, respectively, with the far-left panel showing the original dark field TEM image

The maps in Figure 55 once again show a presence of Cu across the whole TEM grid, but with a slightly higher density of Cu K lines originating from the region containing the nanoparticle, indicating some alloying/ thin shell of Cu.

Point and click EDX and maps were also produced for the 994.1 ± 43.1 °C sample and their results shown in Figure 56, Figure 57, and Figure 58. This sample produced atomic percentages of 91.77 ± 2.53 % Fe and 8.23 ± 0.98 % Cu from region 3 in Figure 56.

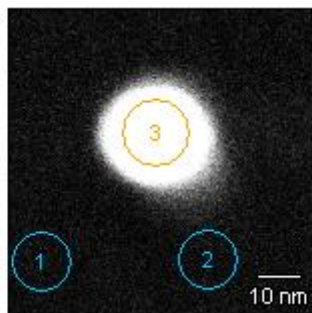


Figure 56 - Dark field TEM image of an example Fe@Cu nanoparticle created with the shell evaporator at 994.1 ± 43.1 °C. The numbers represent three of the areas measured with point-and-shoot EDX.

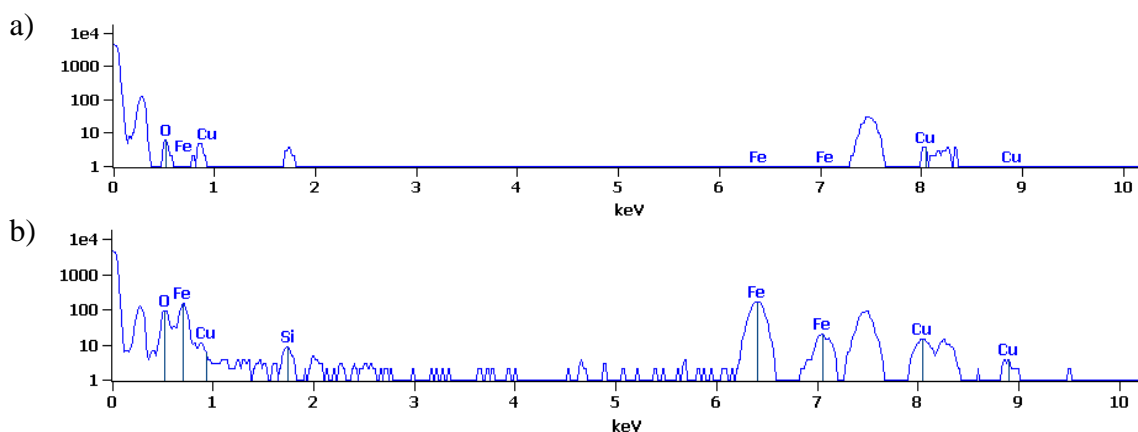


Figure 57 - 2 regions of EDXS TEM analysis of the Fe@Cu nanoparticle in Figure 56 with a) referring to the background, point 1, and b) the area within the particle, denoted with the number 3 in Figure 56.

Again, there is Cu present across the whole TEM grid, shown by the maps in Figure 58 but with a higher density where the nanoparticle is located.

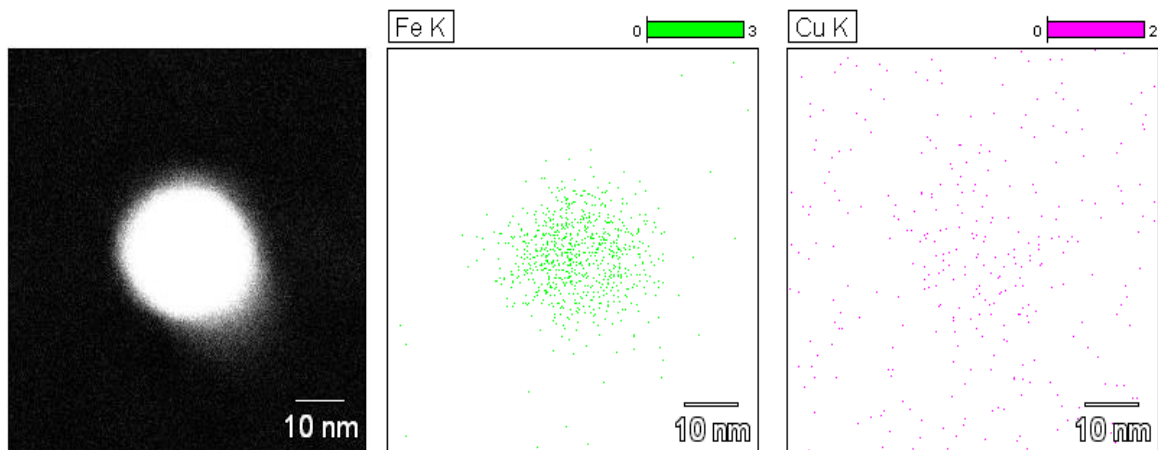


Figure 58 - EDX mapping of a Fe@Cu nanoparticle from the 994.1 ± 43.1 °C sample. The abundance of Fe and Cu have been highlighted in the two panels, middle and right, respectively, with far-left the original dark field TEM image.

The final sample analysed with EDX was the 1130.6 ± 43.2 °C sample, with its results presented in Figure 59, Figure 60, and Figure 61. Two regions were analysed with the Fe and Cu content, as shown in the two dark field TEM images in Figure 59. The region analysed encompassing the whole nanoparticle gave the atomic fraction as 16.40 ± 4.23 % Cu, and the region analysed at the edge as 24.52 ± 7.93 % Cu. This is expected due to the region including some of the background where there is a distinct lack of Fe signal, and there is some background Cu deposited.

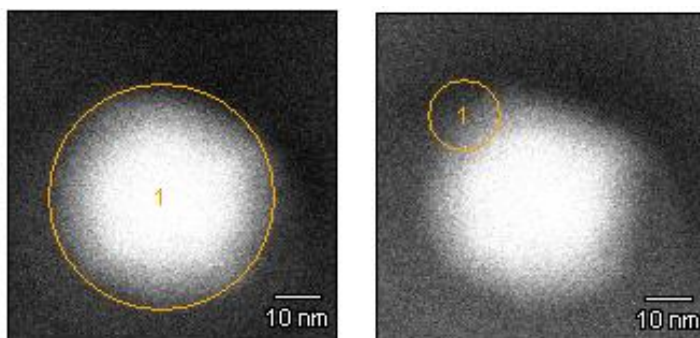


Figure 59 - Dark field TEM image of an Fe@Cu nanoparticle created with the shell evaporator at 1130.6 ± 43.2 °C. The circled area represents the two areas measured with Point and Shoot EDXS.

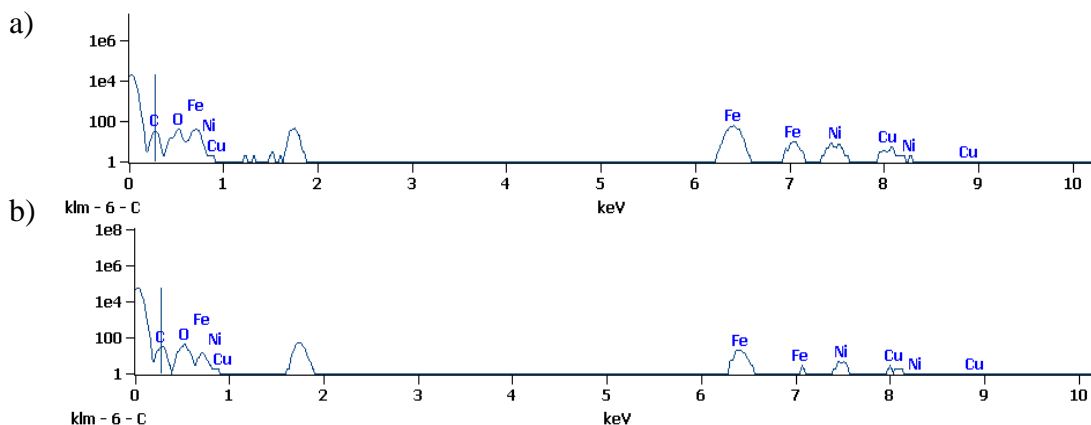


Figure 60 - A region of EDXS TEM analysis of the Fe@Cu nanoparticle in Figure 59. The top spectrum is from the whole particle, (left image in Figure 59), and the bottom spectra is from the edge of the nanoparticle (right image in Figure 59).

Figure 62 compares the atomic Cu percentage across each of the four temperatures measured with point-and-shoot EDX. These values only take into account the Cu and Fe signals. The values plotted Figure 62 are from regions within the nanoparticles themselves.

Figure 62 shows, relative to the Fe content, that there is a significant amount of Cu present on our nanoparticles. There is not, however, an obvious relationship between a higher core shell temperature and the percentage of Cu, which previous work by the group suggested.

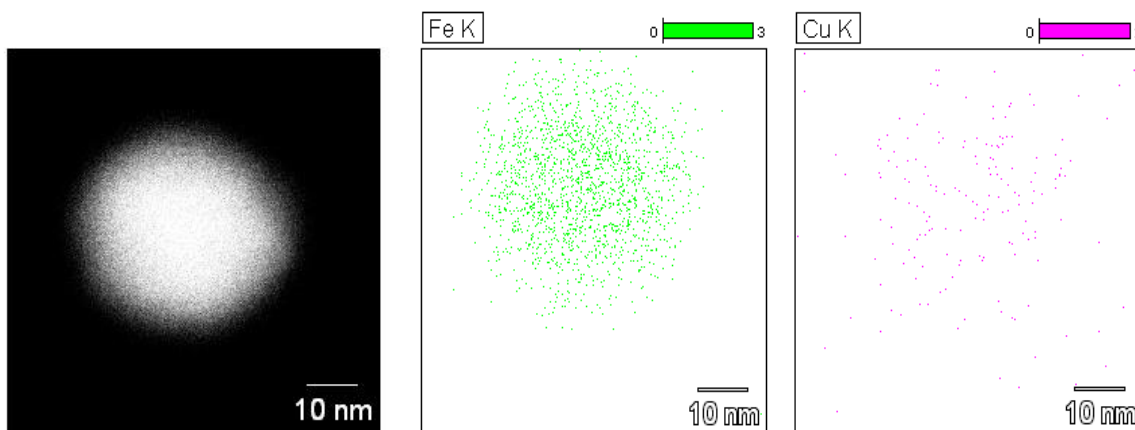


Figure 61 - EDX mapping of a nanoparticle from the 1130.6 ± 43.2 °C sample. The abundance of Fe and Cu have been highlighted in the two panels, middle, and right, respectively, with the far-left panel the original dark field TEM.

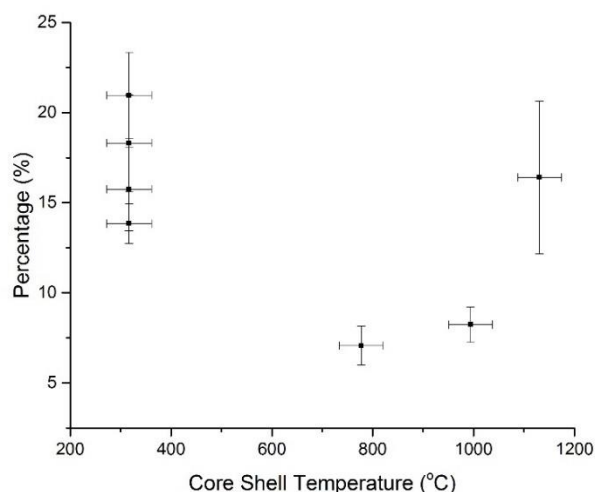


Figure 62 - Cu atomic percentage across the four core shell temperatures measured with point-and-shoot EDX.

3.4 Discussion

Comparison of the EDX spectra from all background regions across all the samples show no Fe signal outside of the particle region, as expected, suggesting that the Fe particles are being deposited with little to no extra molecular Fe in the beam. For the Cu there is some coverage across the whole TEM grid as indicated in the maps in Figure 52, Figure 55, Figure 58, and Figure 61, plus the line scans in Figure 50. This is consistent with a small amount of leakage of Cu from the crucible into the deposition chamber.

However, the EDX data do show an increase in the Cu signal in the particle region. This indicates that there some coating of the Fe nanoparticles with Cu or some alloying between the Fe and Cu. It was seen that the line-scan across the particle in the sample deposited at 316.8 ± 44.6 °C (see Figure 50) indicates that the Cu-content is highest in the centre of the particle. This is more consistent with alloying than shell formation.

The atomic percentage of Cu, when considering only the Fe and Cu spectral counts, yields values of ~ 15 % with no clear relationship between the core shell evaporator temperature and the Cu atomic percentage. One possible reason for the lack of an increase in Cu content at higher temperature is that the Fe nanoparticles passing through the coating cell are hot enough for some of the Cu landing on them to re-evaporate. Although further data is required for definitive conclusions, the data presented here does indicate that there is a degree of alloying in the Fe@Cu nanoparticles. The fact that Cu is incorporated into the Fe nanoparticles should mean that the surface energy is lowered (relative to the pure Fe

nanoparticles) as suggested in section 2 of this chapter; it is therefore consistent with the particle shape change as described in section 2.

4. Magnetometry Data

4.1 Introduction

As outlined in the *Chapter 2: Experimental Methods*, samples were prepared for measurement in a SQUID magnetometer. These samples consisted of ~ 20 nm buffer layer of Ag, ~ 100 - 150 nm of 5 – 10 % Fe@Cu to Ag volume fraction, and a minimum cap of 50 nm Ag. The samples were deposited on Si (100) substrates of 7 mm x 5 mm and stored in gelatine capsules for ease of transportation and analysis. Three samples were produced at varying core shell temperatures: 441.6 ± 44.2 °C, 773.6 ± 43.5 °C, and 1136.5 ± 43.2 °C.

The measurements enabled us to determine whether the nanoparticles were superparamagnetic or magnetically blocked. Saturation magnetisations and estimates for the heating that the particles could produce, were also obtained from the data.

4.2 Analysis Methods

The raw data is recorded in the format of total sample moment (in emu) versus the applied magnetic field when at 5 K, and at 300 K. The moment is then converted into Am^2 from emu and divided by the mass of Fe in the sample. The mass of Fe is estimated from XTM measurements before, during and after the sample deposition and an average coverage is taken for each time period. Given that the silicon slides are 5×7 mm in size, and approximately 1 mm was covered by the mask holding them in place, an area of 4×6 mm was assumed to be coated. From this, the mass of Fe could be calculated.

Plotting the moment per gram of iron (Am^2/g) values versus the magnetic field (T) yields the magnetisation curve, which characterises the magnetic behaviour of the nanoparticle sample. This can be in the form of a hysteresis loop, dependent on the size of the nanoparticles produced and on the measurement temperature (see *Chapter 3: Magnetic Nanoparticle Theory and Medical Applications* for more information).

4.3 Results

The plots in Figure 64 and Figure 65 show the magnetisation curves for the three core samples at 300 K and 5 K, respectively. The top plot in each show the magnetisation curves across the full range of the SQUID magnetometer, from - 5 T to + 5 T, whereas the bottom plots in each shows the same information but between ± 1 T to highlight the hysteresis behaviour of the nanoparticles in these samples more clearly. It can be seen in these magnetometry plots that the moment values often spike around 0.5 – 1 T which is not indicative of the properties of the nanoparticles, rather an artefact of the equipment.

Figure 64 and Figure 65 illustrate the magnetic behaviour of the three samples. The graphs suggest that all 3 show similar magnetic responses and hysteresis, with no significant “bulging” as was seen in the pure Fe sample created at 21 °C in *Chapter 4: Fe Studies*, Figure 30.

As in *Chapter 4: Fe Studies*, Langevin functions were fitted to these curves to give the saturation magnetisation for each core shell temperature, such as that in Figure 63. The values from these fits (\pm one sigma error) were then plotted versus the core shell temperature in Figure 66.

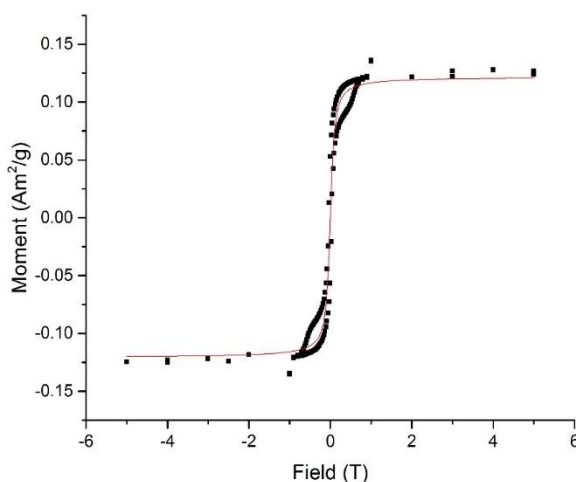


Figure 63 - Example Langevin fitting for the Fe@Cu 773.6 ± 43.5 °C sample

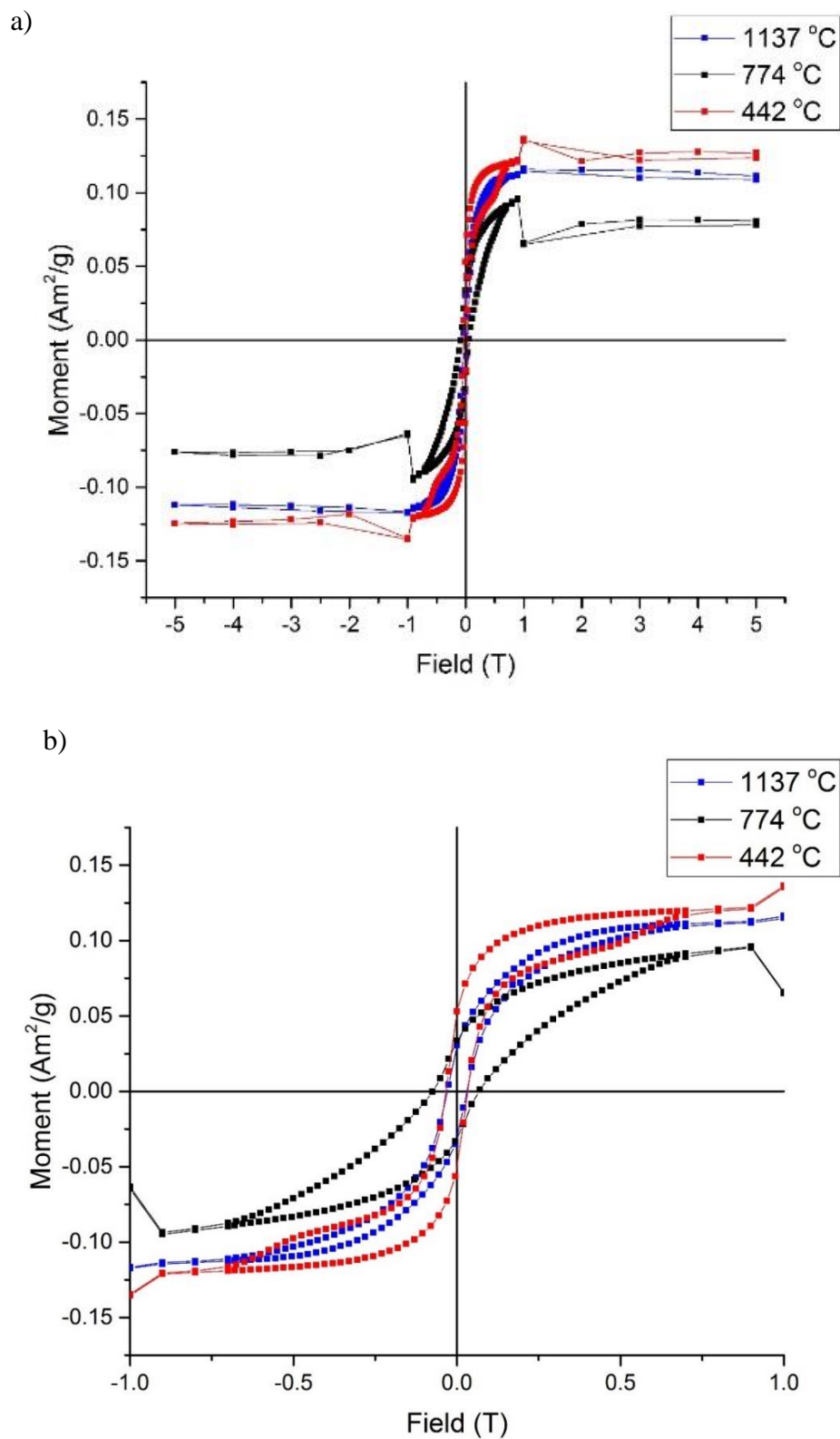


Figure 64 - Magnetometry data from the Fe@Cu sample measured in the SQUID at 5 K. a) shows the full data range obtained from ± 5 T and b) shows the same data but between ± 1 T to show the hysteresis behaviour of the nanoparticles in more detail.

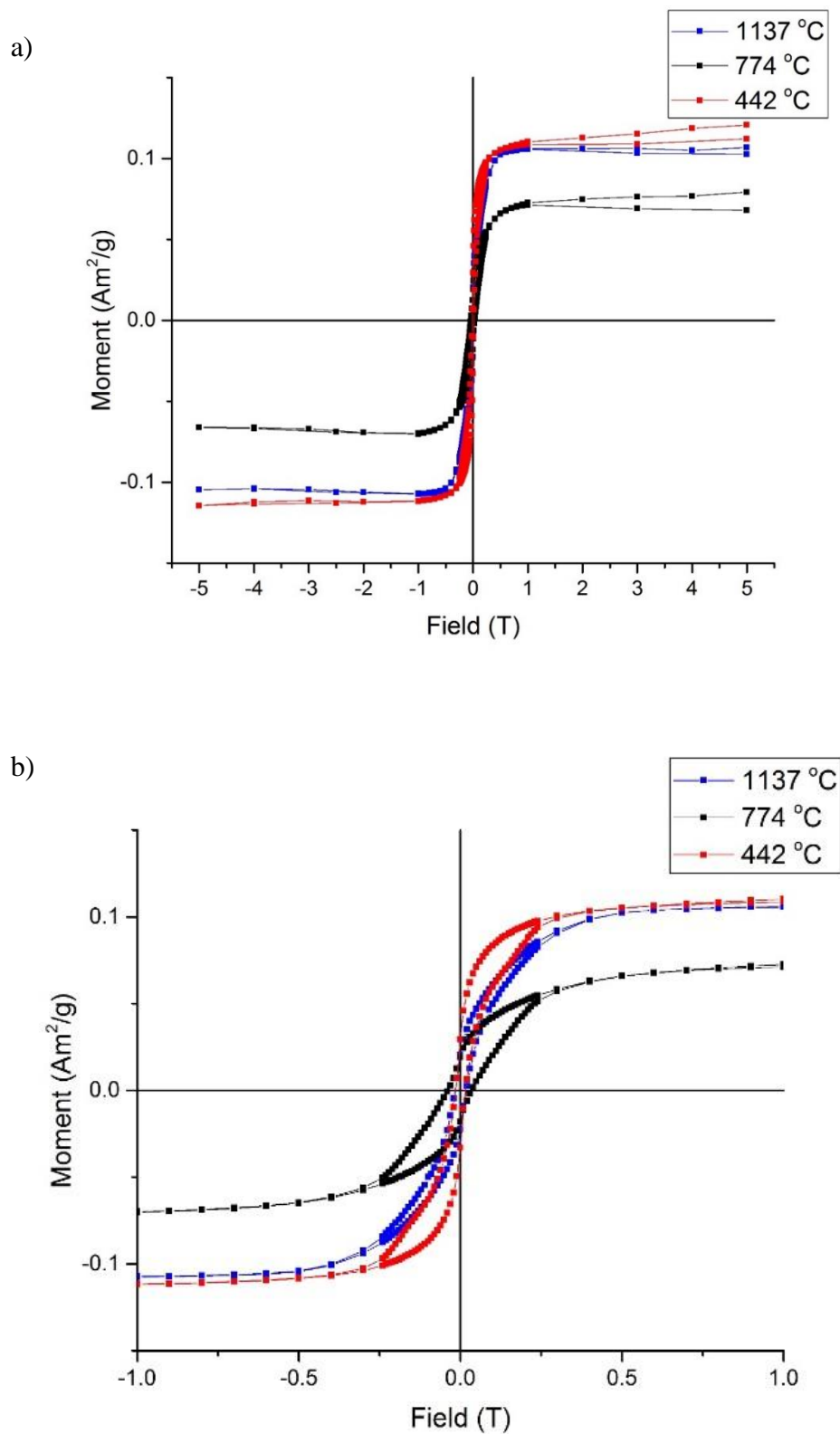


Figure 65 – Magnetometry data from the Fe@Cu samples measured in the SQUID at 300 K. a) shows the full data range obtained from ± 5 T and b) shows the same data but between ± 1 T to show the hysteresis behaviour of the nanoparticles in more detail.

As mentioned in the previous chapter (*Chapter 4: Pure Fe Studies*), the Langevin function takes the form of,

$$L(x) = \coth(x) - \frac{1}{x},$$

The Langevin function describes the classical limit of the Brillouin function which describes the dependency of the magnetisation, M , on the applied magnetic field, B , and the total angular quantum number, J , of the microscopic magnetic moments for an ensemble of non-interacting paramagnetic atoms or ions. Nanoparticles of magnetic materials such as Fe contain hundreds to thousands of atoms, and can also behave paramagnetically. The exchange interaction locks the atomic moments together, so the nanoparticle behaves as if it has a single giant moment. It therefore behaves like a classical magnetic dipole moment. This is why a classical description via the Langevin function is justified in this context.

In the plots in Figure 64 and Figure 65 the magnetisation curves for our nanoparticles do not fit to a simple Langevin function, since they are modified by hysteresis, but the lower and upper saturation limits of the magnetisation do converge to a Langevin. The saturation magnetisations obtained from these fits are used to give a value for the saturation magnetisation for each of our nanoparticle samples and are plotted with \pm one sigma error bars from these fits in Figure 66.

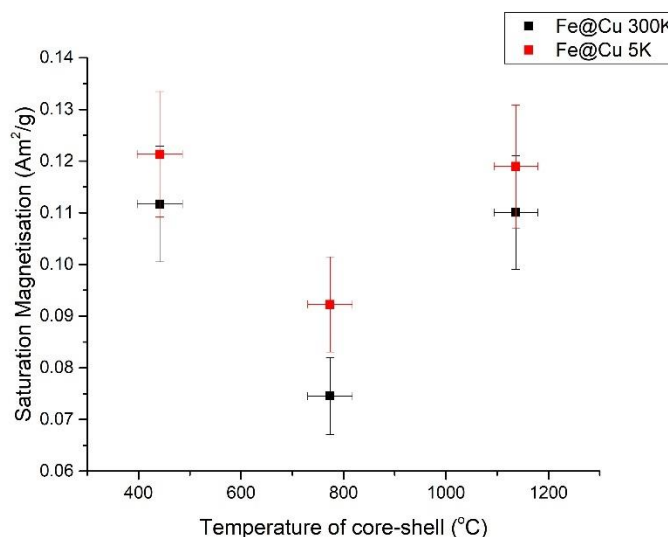


Figure 66 – Saturation magnetisation of Fe@Cu samples from Langevin fits of the raw hysteresis curves shown in Figure 64 and Figure 65, plotted against the temperature of the core shell evaporator the nanoparticles were subjected to.

With only data from only 3 samples, it is difficult to come to any significant conclusions on the effect of core shell temperature on the saturation magnetisation of the Fe@Cu nanoparticles. However, comparing these to the corresponding data for the pure Fe samples, as in Figure 67 and Figure 68, does show that there is no apparent difference between the pure Fe samples and the Fe@Cu samples at 300 K or at 5 K. Some argument could be made that the Fe@Cu samples have a higher saturation magnetisation at temperatures >1100 °C (at both 300 K and 5 K) compared to the corresponding Fe nanoparticles, although further data should be obtained to check if this is consistently so.

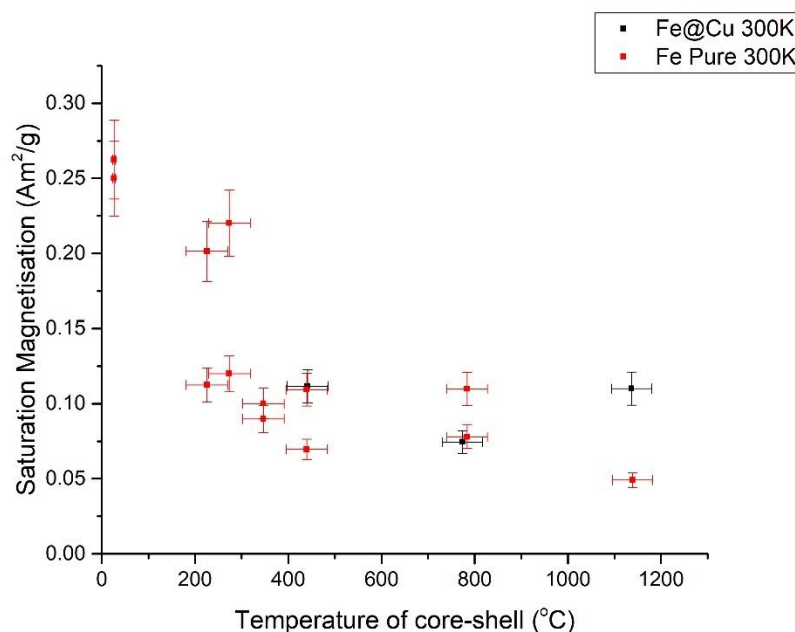


Figure 67 – Comparison of the saturation magnetisation of Fe@Cu and Fe samples from Langevin fits of the raw magnetometry data of samples measured at 300 K in the SQUID magnetometer.

As with the pure Fe samples, the polygon area of each of the hysteresis loops was measured with an example of such given in Figure 69 for the sample produced with the core shell evaporator operating at 773.6 ± 43.5 °C. The heating output of the nanoparticles is not only dependent on the saturation magnetisation, but also the area enclosed by the hysteresis loop. Further information on this relationship is discussed in *Chapter 3: Magnetic Nanoparticle Theory and Medical Applications*.

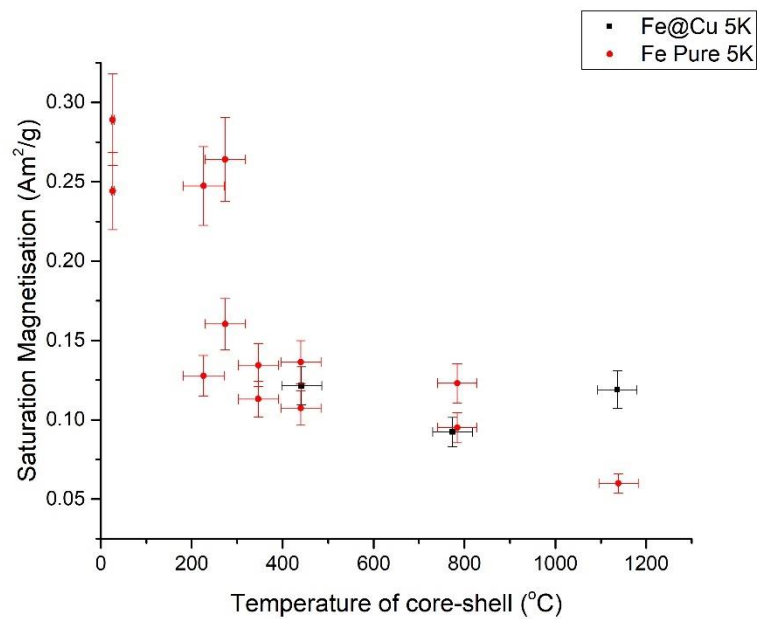


Figure 68 – Comparison of the saturation magnetisation of Fe@Cu and Fe samples from Langevin fits of the raw magnetometry data of samples measured at 5 K in the SQUID magnetometer.

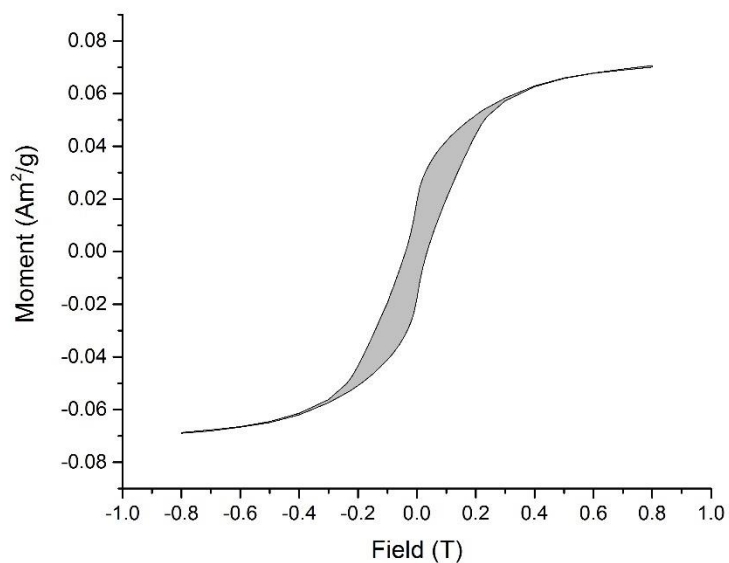


Figure 69 - Example hysteresis curve from the sample produced with the core shell evaporator operating at 773.6 ± 43.5 $^{\circ}\text{C}$ with the grey shaded section representing the area enclosed by the loop, plotted in Figure 70.

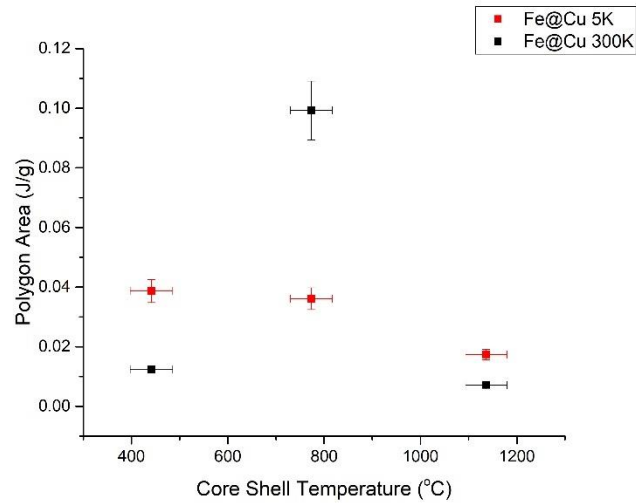


Figure 70 -The polygon areas from the three Fe@Cu samples, measured at 5 K and 300 K in the SQUID magnetometer. The values plotted arise from plots such as Figure 69.

Figure 70 shows the sample produced the core shell evaporator operating at 773.6 ± 43.5 °C at 300 K having a higher polygon area than that of its counterparts. The data in Figure 70 have also been plotted alongside the pure Fe samples' polygon areas in Figure 71. Figure 72 shows the corresponding data for measurements taken at 5K.

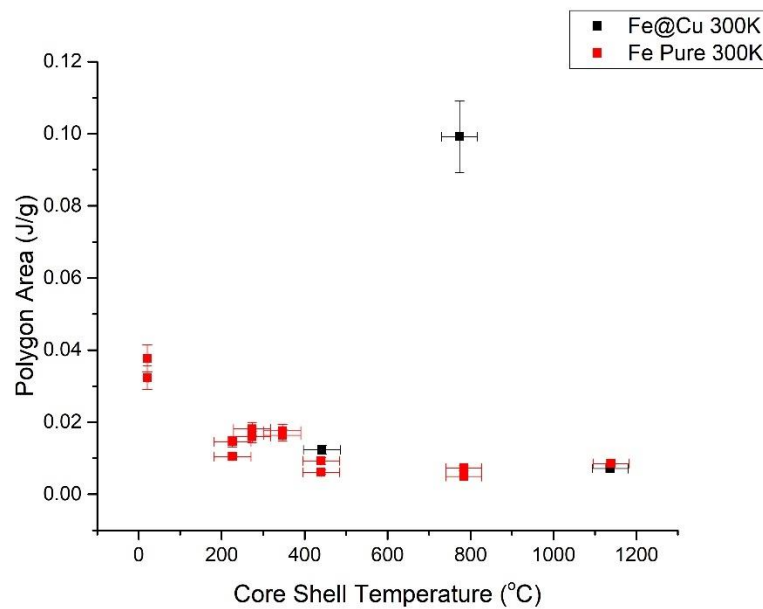


Figure 71 - The polygon areas of hysteresis from the three Fe@Cu samples (black) and the 13 pure Fe samples (red) measured at 300 K in the SQUID magnetometer.

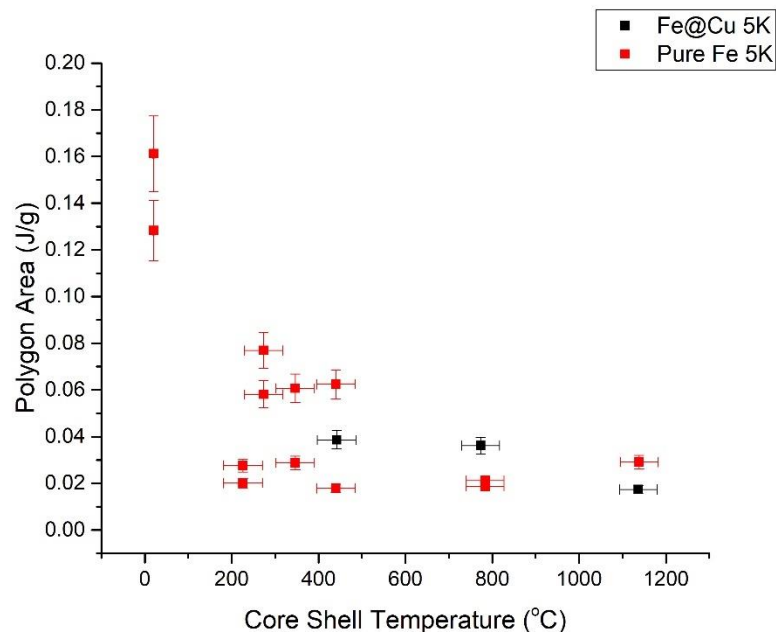


Figure 72 - The polygon areas of hysteresis loops from the Fe@Cu samples (black) and the pure Fe samples (red) measured at 5 K in the SQUID magnetometer.

Figure 72 indicates that the areas of the hysteresis loops measured at 5 K are not strongly affected by the introduction of Cu into the core shell evaporator; there is no significant change between the values for pure Fe samples and the Fe@Cu samples. This contrasts with the data collected at 300 K (albeit there are only 3 data points) which indicate a potential optimum core shell evaporator temperature. As described previously, the area enclosed by the hysteresis loops does not give a direct measurement of the SAR of the nanoparticles but does give a good indication that these nanoparticles may be better performing than those synthesised at other temperatures. Also as discussed previously, an AC magnetometer would be required to measure hysteresis loops with varying maximum magnetic fields applied; the nanoparticles may well have higher SAR values with a lower magnetic field since this allows the frequency of the applied magnetic field to be increased (as long as the Atkinson-Brezovich limit is not exceeded of course: $H_o \times f, = 4.85 \times 10^8 \text{ Am}^{-1} \text{ s}^{-1}$ (Atkinson, Brezovich, & Chakraborty, 1984) - see *Chapter 3: Magnetic Nanoparticle Theory and Applications* for more information).

4.4 Discussion

The M-H curves in Figure 64 and Figure 65 show that the Fe@Cu nanoparticles are not superparamagnetic but blocked. This is apparent from the clear hysteresis exhibited in the two plots that have been enlarged between ± 1 T. This behaviour is not drastically different between the 5 K and the 300 K measurements within the SQUID magnetometer.

Fitting a Langevin distribution to these curves allows for calculation of the saturation magnetisation for each sample, and these values (\pm one sigma) are plotted in Figure 66. These values are compared with the 5 K and 300 K values from the pure Fe samples (see *Chapter 4: Pure Fe Studies* for further information on these samples) in Figure 67 and Figure 68, respectively. There does not appear to be a significant difference between the saturation magnetisation values for the pure Fe samples in comparison to those for the Fe@Cu. Further samples created with the core shell evaporator operating at temperatures above 1100 °C will indicate if Fe@Cu samples perform better than pure Fe samples, as hinted at by the sample created at 1136.5 ± 43.2 °C in Figure 67 and Figure 68. This sample has a saturation magnetisation value of 0.119 ± 0.001 Am²/g at 5 K, and 0.110 ± 0.001 Am²/g at 300 K. However, it should be pointed out that the 441.6 ± 44.2 °C sample has very similar values of 0.121 ± 0.002 Am²/g, and 0.112 ± 0.002 Am²/g for the 5 K and 300 K measurements, respectively. This potentially hints at an increase in saturation magnetisation values above the 1136.5 ± 43.2 °C sample.

Data for the pure Fe nanoparticles (see *Chapter 4: Pure Fe Studies*) showed a decrease in saturation magnetisation with an increased core shell temperature, which could be attributed to the shape change of the particles from mostly cubic to mostly spherical. Here, however, the Fe@Cu samples do not show an increased geometry factor with increasing core shell temperature, and the saturation magnetisation of these samples appears to remain stable also. This raises the question as to whether perhaps the Fe@Cu nanoparticles would perform more favourably in MRI relaxivity. Atkas, et al., (2015) observed that heated Fe nanoparticles (with increased geometry factor) showed a decrease in the MRI relaxivity. Here, however, the geometry factor of the Fe@Cu samples remains constant as the core shell evaporator temperature is increased.

The polygon areas of the Fe@Cu samples measured at 5 K within the SQUID magnetometer do not differ significantly from those for the pure Fe samples, as shown in

Figure 72. Figure 71, however, hints at potential optimum temperature for the core shell evaporator in the case of the Fe@Cu nanoparticles.

It is important, however, to point out that these conclusions are based solely on three magnetometry samples and, although promising, further samples should be synthesised and analysed to extend the observations discussed in this section.

5. Conclusions

This chapter reports on whether the addition of a Cu shell to the Fe nanoparticle in our experimental set-up is feasible, and if so, how this Cu shell affects the size, shape, and magnetic properties of our samples, and how these characteristics are altered with a change in crucible temperature. This was investigated by analysis data collected in TEM, EDX, and magnetometry measurements.

The EDX data shows Cu coverage on all sample investigated, but with low proportions of Cu. The maps in Figure 52, Figure 55, Figure 58, and Figure 61 show Cu signals originating from areas other than the nanoparticle, indicating that there is some Cu leakage from the core shell evaporator into the deposition chamber. However, the density of Cu signal is higher at the nanoparticle locations, indicating that the inclusion of Cu on the Fe nanoparticles is significant. The fact that the Cu signal is strongest from the centre of the nanoparticles is more suggestive of alloying rather than shell formation.

The TEM data shows the nanoparticles produced with Cu in the evaporator have a lower diameter than those without Cu present when the temperature is over 700 °C, as can be seen in Figure 45. The geometry factor dependence on temperature is also different between the sets of samples; the geometry factor for the pure Fe samples increased with increasing core shell temperature, whereas for the Fe@Cu nanoparticles it remained within the cuboctahedral range (0.7 – 0.8). This indicates that the addition of Cu has a significant effect on the shape of nanoparticles produced in the source.

As discussed in section 2.4 of this chapter, addition of Cu should ultimately change the surface energy of the nanoparticles, meaning that perhaps they now require a higher temperature to overcome the energy barrier to produce more spherical nanoparticles, than for pure Fe alone. This is supported by Figure 42, where the percentage of cubes does not decrease, as for the pure Fe samples in the previous chapter. Rather, they actually increase

with an increased core shell temperature, perhaps due to the higher percentage of Cu present. The surface energy of bulk fcc Cu (111) is 1409 J/m^2 (Zhang, Ma, & Xu, 2004), below that of bulk Fe (2123 J/m^2); thus the addition of Cu to the nanoparticle will decrease the surface energy of the nanoparticle. This may explain why there are fewer cuboctahedral and spherical nanoparticles at higher core shell temperatures in this Fe@Cu sample set in comparison to the pure Fe samples, as the surface energy has been drastically altered with the addition of Cu, whether as a shell or as an alloy with the Fe.

The magnetometry curves in Figure 64 and Figure 65 indicate that the nanoparticles here are most likely “blocked” like the pure Fe nanoparticles in the previous chapter. The saturation magnetisations measured for both sets of samples are also similar, as seen in Figure 67 and Figure 68 (these compare the two datasets and show no obvious deviation between the two sets of samples). Considering the change in geometry factor between the higher temperature ranges (between 0.7 - 0.8 for the Fe@Cu samples and > 0.8 for the pure Fe samples), this indicates that the shape of the nanoparticle does not drastically affect its saturation magnetisation.

Figure 42 shows an increase in the production of cubic nanoparticles as the temperature of the core shell is increased. This is not what was observed for the pure Fe nanoparticles in the previous chapter whereby the percentages of cubic nanoparticles drastically decreased with an increased evaporator temperature. This is particularly interesting for MRI relaxivity as Atkas, et al., (2015) reported that samples with a higher cubic content performed better.

Future work includes producing more Fe@Cu samples for TEM and magnetometry to investigate the relationship between temperature and magnetic moment more closely. As with the pure Fe samples, magnetometry measurements using an AC magnetometer would enable a more direct measurement of SAR values to be obtained.

Chapter 6: Other Core Shell Studies

1. Introduction

In the previous chapter, it was described how Cu pellets were added to the empty crucible with the aim of producing Fe@Cu nanoparticles, with a complete Cu shell surrounding the pure Fe core. The EDX data did not confirm an even shell encompassing the Fe core, instead indicating that the Cu had probably alloyed with the Fe. Following on from this, other core shell nanoparticle configurations were attempted, including the use of Al, Mg, and Ag as shell materials. As before, SLUMPS was set up as outlined in *Chapter 2: Experimental Methods*, but instead of an empty crucible, the core shell evaporator was loaded with ~ 1 g of Mg, Al, and Ag. As before, the power supplied to the crucible was varied up to a maximum of ~ 300 W, producing a temperature from ~ 21 °C (room temperature) to ~ 1200 °C.

EDX analysis was unable to determine the presence of Al, or Mg on or around the nanoparticles within the Fe@Al or Fe@Mg sample sets. Samples were produced throughout the full temperature range of the shell evaporator. From this, it can only be concluded that the Al and Mg did not bind to the surface of the Fe nanoparticles, as there was evidence of both Mg and Al vaporisation. Data from the Fe@Ag samples is included in the following section, with information on size, shape, and elemental composition through TEM and EDX analysis.

Previous in-house studies by the group have indicated that the size of the Fe nanoparticles could be changed by removal of the water coolant to the sputter head. It was suggested that the nanoparticles synthesised without water coolant were smaller, of < 10 nm in diameter, rather than the 10 – 35 nm sizes seen in the previous two chapters. This hypothesis is investigated as smaller sized nanoparticles are more likely to be superparamagnetic, and therefore better performers for MRI contrast agents and in MPI (see *Chapter 3: Magnetic Nanoparticle Theory and Medical Applications* for more information on these imaging techniques). Data from pure Fe samples (no coolant), and Fe@Cu samples (no coolant) were investigated and their results included within this chapter, including data from TEM and magnetometry analysis.

2. Fe@Ag

2.1 Introduction

Previous studies have produced interesting Fe@Ag nanoparticles, as published in Pratt A., et al (2014), whereby the Ag did not produce complete shells but formed clusters at the Fe core surface. These small amounts of Ag at the surface lead to a significant change in the formation of the oxide shell, with Fe-oxide protrusions at the cuboid corners with Ag nanoclusters acting as catalysts for the oxidation process.

Following on from this work, Fe@Ag samples were produced in order to carry out further investigations into such samples. The magnetic properties of the samples in Pratt A., et al (2014) were not investigated, nor were the shapes or sizes of such samples studied in detail.

All samples in this section were created using the sputter source outlined in *Chapter 2: Experimental Methods* and deposited on Cu TEM grids. As the TEM samples are unavoidably exposed to air in transit between the cluster source and the TEM, it is expected that some O will be present.

2.2 Analysis Methods

To analyse the shape of the nanoparticle, a geometry factor was utilized, which is extracted from the 2-D TEM image of the nanoparticle. The geometry factor is calculated by dividing the true area of the nanoparticle measured from the TEM image by the maximum area possible if the nanoparticle were a perfect circle. For example, in a square you would take the diameter from corner to corner, through the centre of the square, and use this diameter to calculate the area of a circle of the same diameter and then divide it into the actual area of the original square. To obtain this information, the analysis package ImageJ was utilised as it has the capability to measure the Feret diameter.

The ratio is 0.63 for a perfect square and 1.0 for a perfect sphere and allows for good judgement of the 2-D shape of the nanoparticle. This method was chosen due to its ease of implementation and removal of user subjectivity, since previous approaches by the group (Atkas, et al., 2015) were to view each nanoparticle individually and note down

the shape based on their appearance. This is not only very time consuming but can also be heavily biased.

In the following plots, any geometry factor between 0.4 and 0.7 is classed as a square or a truncated square, and the particle assumed to be cubic. Between 0.7 and 0.8 the particle is categorised as a cuboctahedral and above 0.8, the nanoparticle is assumed spherical. Any area measurements quoted below refer to the true area of the nanoparticle from TEM images, as measured with ImageJ. A cubic nanoparticle is assumed to look like a square in a 2-D image. A cuboctahedral/cuboctahedron is a polyhedron with 8 triangular faces and 6 square faces. This means its geometry factor will most likely be higher than a square, but lower than that of a sphere.

The data here encompasses 5 samples made at differing temperatures of the core shell evaporator and is included in Table 6. This is solely dependent on the quality of the TEM images, the number of images obtained, and the number density of nanoparticles on the grid.

Core Shell Temperature (°C)	Number of Nanoparticles Analysed
440.8 ± 43.6	79
609.4 ± 43.8	84
800.7 ± 43.4	92
1010.9 ± 43.2	107
1137.7 ± 43.2	93

Table 6 - 5 Fe@Ag TEM samples made at differing temperatures of the core shell evaporator, and the number of nanoparticles analysed per sample.

2.3 Results

TEM images collected showed no indication of the abnormal morphology as published by Pratt, et al., (2014). All the TEM images showed normal core-shell nanoparticle similar to those in Figure 4 and some example images are given in Figure 73.

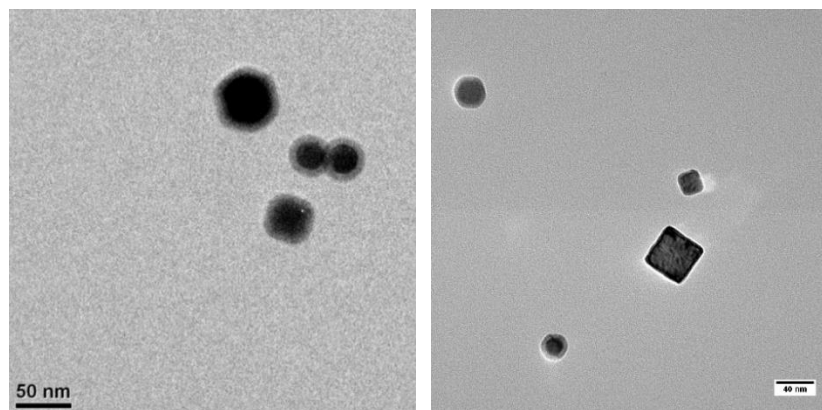


Figure 73 – Example TEM images of the Fe@Ag samples.

The geometry factor for each dataset was separated into bins and plotted into a histogram and a 2-parameter Weibull distribution fitted. An example of this fitting is provided in Figure 74, for the sample produced at 1137.7 ± 43.2 °C.

As mentioned in the previous 2 chapters, the Weibull distribution is very useful for fitting data that follow an atypical normal distribution, with a skew in either direction. Mainly, it is used for right-skewed data such as that shown in the left-hand plot in Figure 74, and it follows a stretched exponential distribution. The probability function of a Weibull is as follows,

$$P(x|a, b) = ba^{-b} x^{b-1} e^{-\left(\frac{x}{a}\right)^b},$$

where a is the scale parameter and b the shape parameter. The scale parameter indicates the spread of the distribution, where a large number indicates a large spread. The shape parameter gives an indication on the shape of the distribution. For example, a b value between 3 and 4 gives a bell-shaped curve, similar to a normal distribution. A value below this gives a left-skewed plot, much like a lognormal, whereas a value above 4 gives a right-skewed dataset, as is observed in the data presented in Figure 74, which has a shape parameter value of 27.1.

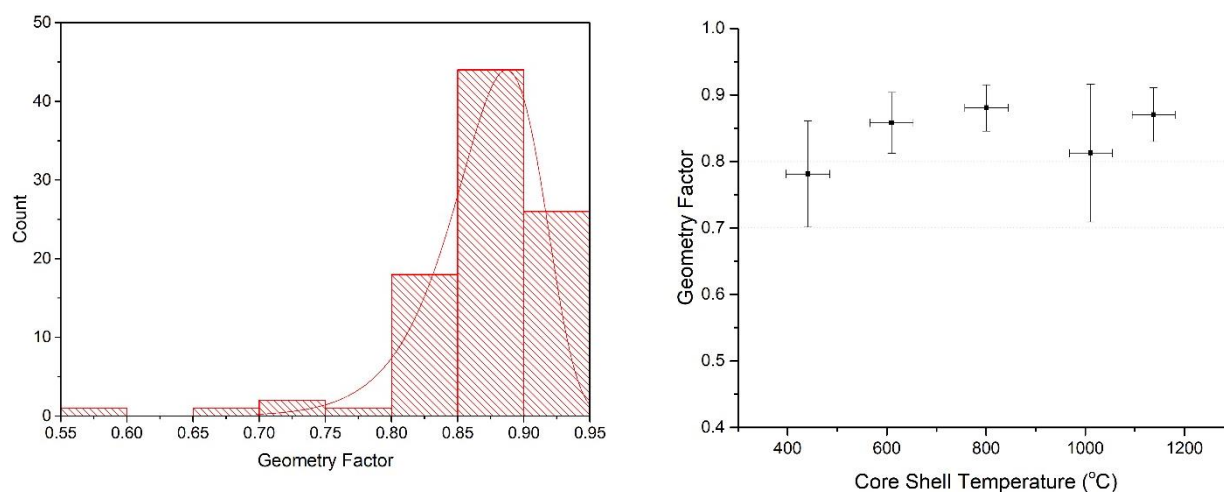


Figure 74 – Left: Geometry factor histogram with a Weibull distribution overplotted for the 1137.7 ± 43.2 °C Fe@Ag sample. Right: The geometry factor versus the temperature of the core shell evaporator, where the plotted values are the means for the Weibull distributions fits (\pm one sigma error bar).

Fitting the measured distributions to the Weibull distributions allows one to assign a mean value for the geometry factor, along with a \pm one sigma value, for each core shell temperature. The right-hand plot in Figure 74, illustrates this data.

Figure 75 plots the geometry factor for both the pure Fe samples (see *Chapter 4: Pure Fe Studies*), and the Fe@Ag samples to investigate any differences.

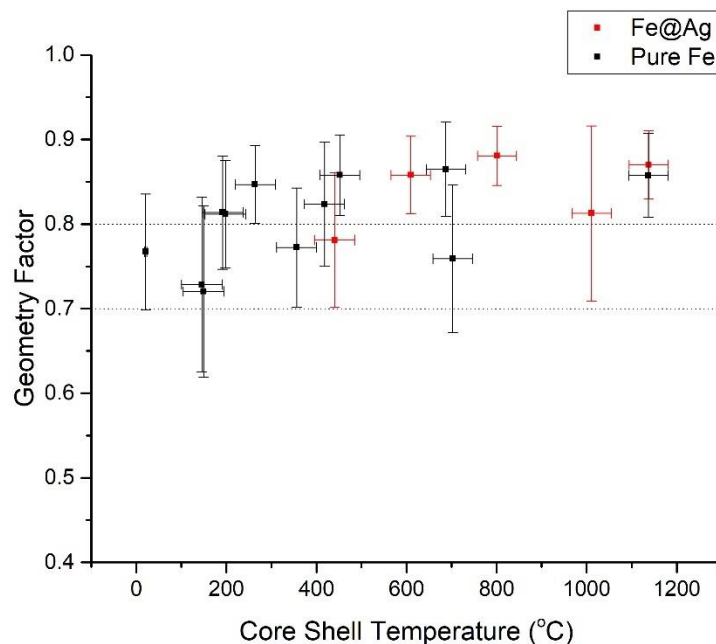


Figure 75 - The geometry factor versus the temperature of the core shell evaporator, where the plotted values are the means for the Weibull distributions fits \pm one sigma error bar. The data from the Pure Fe samples in black (see *Chapter 4: Pure Fe Studies* for further information) and the Fe@Ag samples in red. The dotted lines indicate the separation of the cubic (0.4 – 0.7), cuboctahedral (0.7 – 0.8), and spherical (0.8 – 1.0) regions.

Figure 74 suggests that most of the nanoparticles fall within the spherical range FOR the Fe@Ag samples, and it could be argued that the geometry factor increases with an increased core shell evaporator temperature. This does not disagree with the pure Fe nanoparticle trend, as indicated in Figure 75. In fact, if these two sample sets were not distinguished, one would not be able to decipher between the two.

The plots in Figure 74 and Figure 75, however, do not indicate the proportions of cube, cuboctahedral, and spherical nanoparticles. As in previous chapters, the data has been separated into these regions and plotted in Figure 76, below.

Figure 76 indicates that the percentage of spherical nanoparticles does indeed dominate almost all of the samples, excluding the coldest one produced at 440.8 ± 43.6 °C. The percentage of spheres also tends to increase, with the cuboctahedral nanoparticle percentage decreasing with an increased core shell temperature. This follows the same trend as found for the pure Fe samples in *Chapter 4: Pure Fe Studies*, in Figure 24.

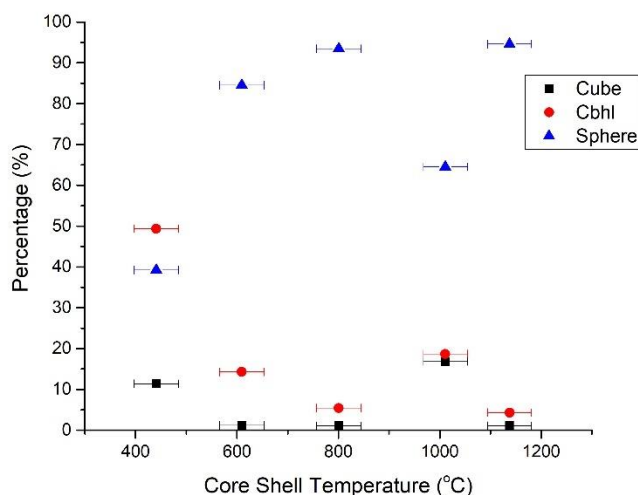


Figure 76 - The percentage of cubes (black squares), cuboctahedrons (red circles), and spheres (blue triangles) for each Fe@Ag sample.

From the true area measurements of the 2-D images of nanoparticles, the particle diameters can be inferred. The diameter measurements were calculated assuming spherical and cubic shapes, with the average of the two taken. These were then plotted into a histogram and fitted with lognormal distributions. The mean and standard deviations (plotted as error bars) of these are plotted in Figure 77.

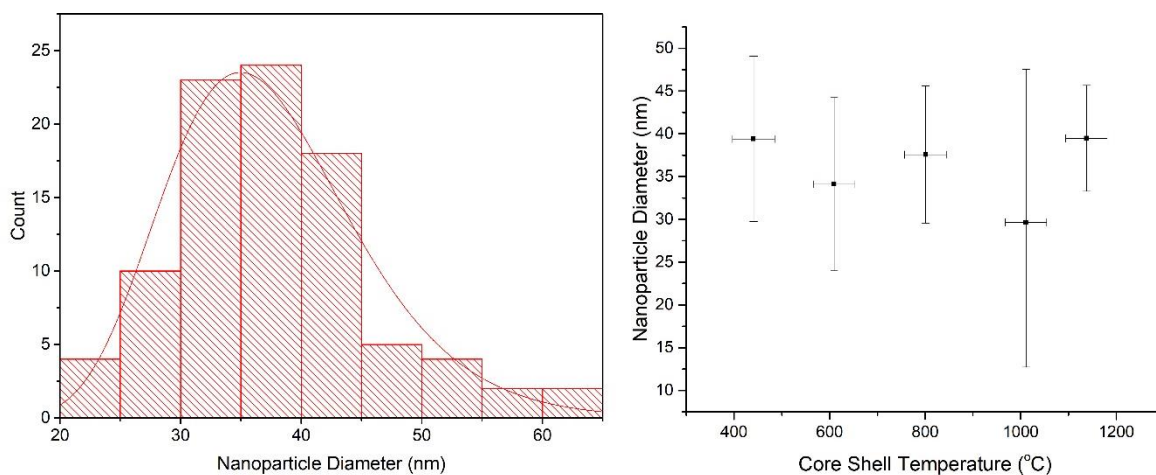


Figure 77 – Left: An example histogram plus lognormal fit for the Fe@Ag sample made at 800.7 ± 43.4 °C. The means and one sigma values (error bars) from this and the other 4 samples are plotted in the right-hand plot.

The diameters in Figure 77 appear to have no overarching trend. Plotting this data alongside the corresponding data for the pure Fe samples shows that the two datasets do not diverge from one another (see Figure 78).

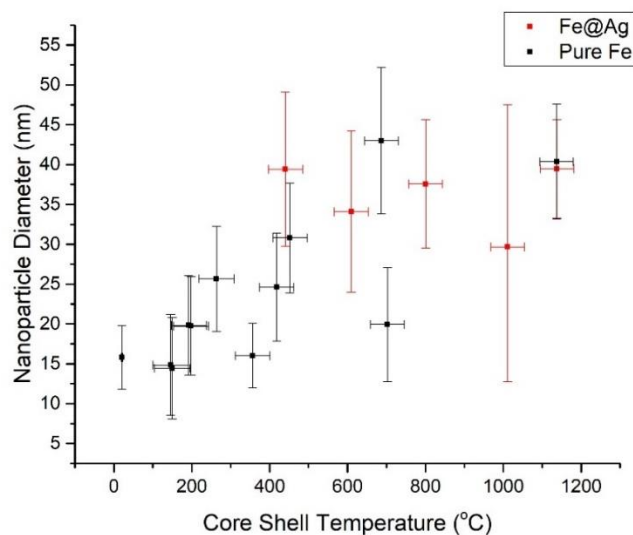


Figure 78 - The diameter of each 2-D nanoparticle vs the temperature of the core shell evaporator for both the Fe@Ag and the pure Fe samples from *Chapter 4: Pure Fe Studies*. Plotted values are the means of the sample from lognormal fitting with one sigma error bars.

As these Fe@Ag samples appear to be of a similar size and geometry factor at comparable core shell temperatures to the pure Fe samples, the geometry factor and area relationship was investigated. As was done for the pure Fe samples and the Fe@Cu samples, particle areas were plotted as a function of geometry factor for all nanoparticles analysed in this dataset (as can be seen in Figure 79).

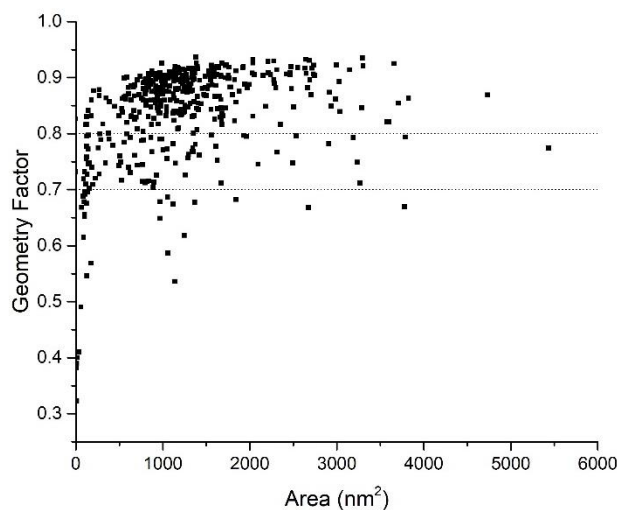


Figure 79 – Geometry factor as a fraction of area for all 455 nanoparticles analysed in this dataset. The dotted lines indicate the separation of the cubic (0.4 – 0.7), cuboctahedral (0.6 – 0.8), and spherical (0.8 – 1.0) regions

From the cluster of points in the top-left of the plot, the vast majority of the nanoparticles appear to within an area range of 500 - 1500 nm² and a geometry factor ranging from 0.7

- 0.9, with very few nanoparticles with areas outside this range. This is very similar to what was found for the pure Fe samples.

Further to this, the number of cubic, cuboctahedral, and spherical nanoparticles within area bins of 200 nm² were calculated and plotted in Figure 80.

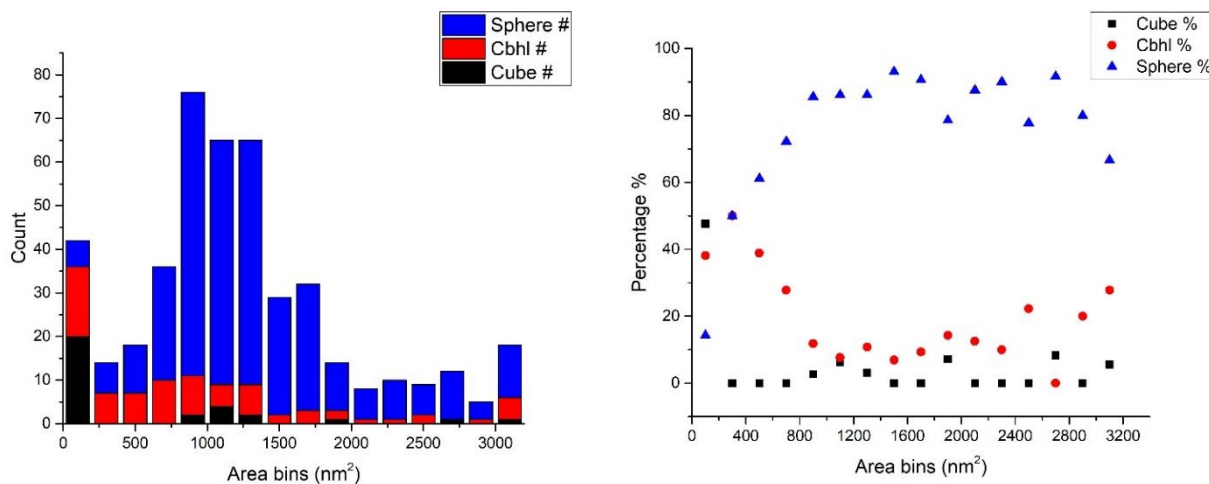


Figure 80 – Left: the number of spheres (blue), cuboctahedrals/cbhl (red) and cubic (black) Fe@Ag nanoparticles in each area bin (200 nm² in size). Right: the percentage of spheres (blue), cuboctahedrals/cbhl (red) and cubic (black) nanoparticles within the same area bins.

Figure 80 shows that the majority of the nanoparticles above 200 nm² are spherical, with very few cubes. The most frequent nanoparticle area is between 800 – 1000 nm², with the vast majority of the nanoparticles having an area between 800 – 1400 nm². This makes the most frequent area of these Fe@Ag nanoparticles to be above that of the pure Fe samples (see *Chapter 4: Pure Fe Studies*), which are mostly below 400 nm² in area. However, this is most likely due to the larger temperature range investigated for the pure Fe samples; lower temperatures were not included here due to the expected lack of Ag vapour at these relatively low temperatures.

2.4 Discussion

This section has investigated the possibility of attaching Ag to our Fe nanoparticle cores, and the effect that this has on size and shape through TEM imagery and analysis.

The geometry factor utilised throughout this project gives an indication of the nanoparticle shape. Here, the geometry factor appears to start in the cuboctahedral range

(0.7 – 0.8) and increase into the spherical region (0.8 – 1.0), as seen in Figure 74. This is indistinguishable from the behaviour of the pure Fe samples, as shown in Figure 75.

Figure 77 gives the nanoparticle diameter from lognormal fitting of the data from each of the 4 temperatures at which the core shell evaporator was run. This plot does not indicate any increase or decrease in nanoparticle diameter, much like the pure Fe samples indicated in *Chapter 4: Pure Fe Studies*. When these two sample sets are plotted side by side as in Figure 78, there is no obvious difference between the two.

Comparisons between the geometry factor and the 2-D area of the Fe@Ag nanoparticles were given in the plots in Figure 79 and Figure 80. Here, the relationship differs from the pure Fe samples from *Chapter 4: Pure Fe Studies*, as the majority of the pure Fe samples were within the 0 – 400 nm² range. This is, however, probably due to the number of samples produced at a temperature lower than the temperatures investigated for the Fe@Ag samples. If the lower area range is ignored when comparing these two sample sets, the percentages of cubes, cuboctahedrals, and spheres are not dissimilar in both cases.

In light of these outcomes, and due to a lack of EDX data, it must be concluded firstly, that significant amounts of Ag have not bound to the Fe cores, and secondly, any small amounts of Ag attachment have no significant effect on the nanoparticle shape or sizing, regardless of core shell evaporator temperature (over the range investigated).

3. No coolant Fe

3.1 Introduction

Previous studies by the group indicated that the size of the nanoparticles could be altered by removal of the water coolant to the sputter head of the magnetron sputter source. The size of the nanoparticles drastically alters their magnetic properties as discussed at length in *Chapter 3: Magnetic Nanoparticle Theory and Medical Applications*; smaller nanoparticles are more suitable for MRI contrast agents and for MPI if they are superparamagnetic.

The following section details data obtained from 10 TEM samples, and 5 samples prepared for SQUID analysis, to investigate more fully the effect of removing the water coolant to the sputter head on the nanoparticle size, shape, and magnetic properties.

3.2 Analysis Methods

This section starts by presenting the data obtained from TEM imagery, outlining the overall size and shape distributions of the nanoparticles. The 10 temperatures that the nanoparticles were subjected to in the coating cell for TEM investigations are given in Table 7.

5 samples were also prepared for SQUID magnetometry and consisted of ~ 20 nm buffer layer of Ag, ~ 100 - 150 nm of 5 – 10 % volume fraction of Fe in Ag, and a minimum cap of 50 nm Ag. The samples were deposited on Si (100) substrates of 7 mm x 5 mm and stored in gelatine capsules for ease of transportation and analysis. 7 samples were produced at varying core-shell temperatures: 21 ± 1 °C, 198.7 ± 45.0 °C, 457.0 ± 44.1 °C, 677.5 ± 43.6 °C, 1138.7 ± 43.2 °C. For all samples, the total sample moment was measured as a function of applied magnetic field, at 5 K and 300 K. The field was varied between ± 5 T.

Core Shell Temperature (°C)	Number of Nanoparticles Analysed
21 ± 1	105
21 ± 1	107
149.5 ± 45.1	84
296.5 ± 44.6	99
423.3 ± 44.2	125
537.3 ± 43.9	112
661.4 ± 43.7	125
779.8 ± 43.5	113
1056.8 ± 43.2	115
1137.6 ± 43.2	92

Table 7 – The 11 different temperatures the nanoparticle TEM samples were produced at, and the number of nanoparticles analysed in each sample.

The measurements enabled us to determine whether the nanoparticles were superparamagnetic or magnetically blocked. From these M-H plots, the saturation magnetisations of each of these samples was also calculated.

As in previous chapters (*Chapter 4: Pure Fe Studies* and *Chapter 5: Fe@Cu Studies*), the moment per gram of Fe (Am^2/g) was plotted versus the magnetic field (T), yielding the magnetisation curve, which characterises the magnetic behaviour of the nanoparticle sample. This can be in the form of a hysteresis loop, dependent on the size of the nanoparticles produced and on the measurement temperature (see *Chapter 3: Magnetic Nanoparticle Theory and Medical Applications* for more information).

3.3 Results

As in the previous section, the geometry factor for each sample was separated into appropriate bins and plotted into a histogram. These histograms were then fitted with a 2-parameter Weibull distribution. The Weibull distributions gave a mean value for the geometry factor, along with a \pm one sigma value, for each core shell evaporator temperature. Figure 81 shows the geometry factor for these pure Fe samples without coolant supplied to the sputter head.

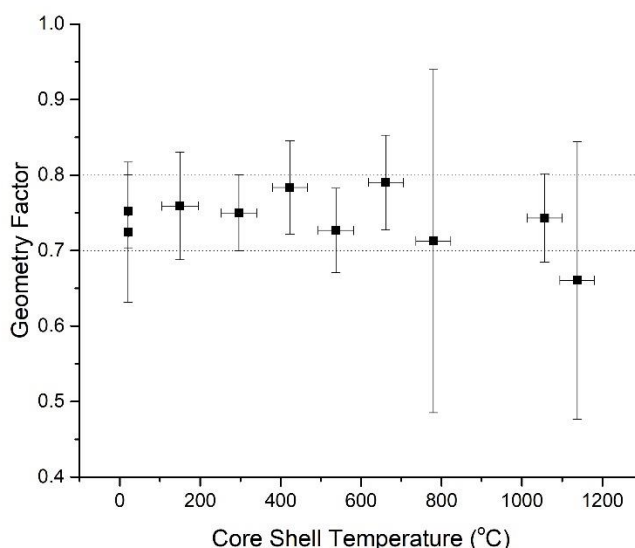


Figure 81 - Geometry factor for the 10 pure Fe TEM samples produced without coolant supplied to the sputter head. The dotted lines indicate the separation of the cubic (0.4 – 0.7), cuboctahedral (0.7 – 0.8), and spherical (0.8 – 1.0) regions. The values come from Weibull fits of the raw data with ± 1 sigma error bars.

The geometry factor remains within the cuboctahedral range (0.7 – 0.8) for almost all temperatures investigated here. This differs from the pure Fe samples with the coolant supplied to the sputter head, which tends to increase with an increasing core shell evaporator temperature.

Figure 82 plots the percentage of cubic, cuboctahedral, and spherical shaped nanoparticles against the core shell temperature to investigate the trends in the shape change that may be overlooked when plotting only the mean geometry factor (\pm one sigma error bars). This figure does not suggest any significant trends between the temperature and shape. Cube nanoparticle percentages and spherical nanoparticle percentages appear to remain roughly constant throughout the core shell evaporator temperatures. These trends differ from those of the pure Fe samples (see Figure 24 in *Chapter 4: Pure Fe Studies*) where the percentage of cubic nanoparticles drastically decreases, and the spherical percentage increases with increased core shell temperature.

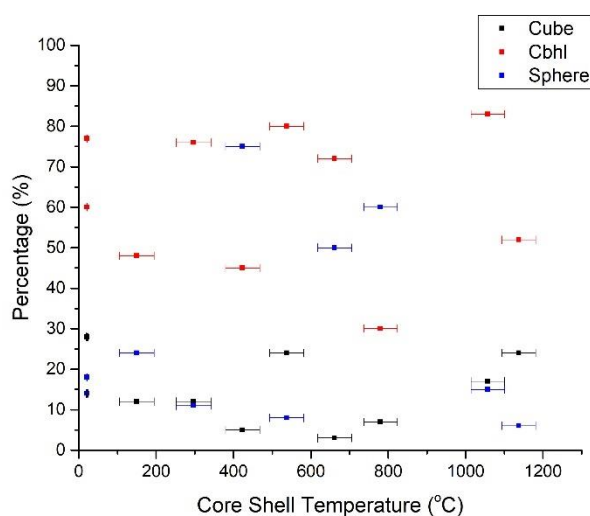


Figure 82 - The percentage of cubes (geometry factor 0.4 -0.7, black), cuboctahedrals (0.7 – 0.8, red) and spheres (0.8 - 1.0, blue) versus the core shell temperature for the 10 pure Fe TEM samples without coolant supplied to the sputter head.

As previously discussed, the nanoparticle diameter (\pm one sigma error bars) can be calculated by fitting lognormal distributions of the raw area measurements taken from TEM images using ImageJ. These values are plotted in Figure 83. Comparison with the pure Fe samples prepared with the coolant supplied to the sputter head is included in Figure 84.

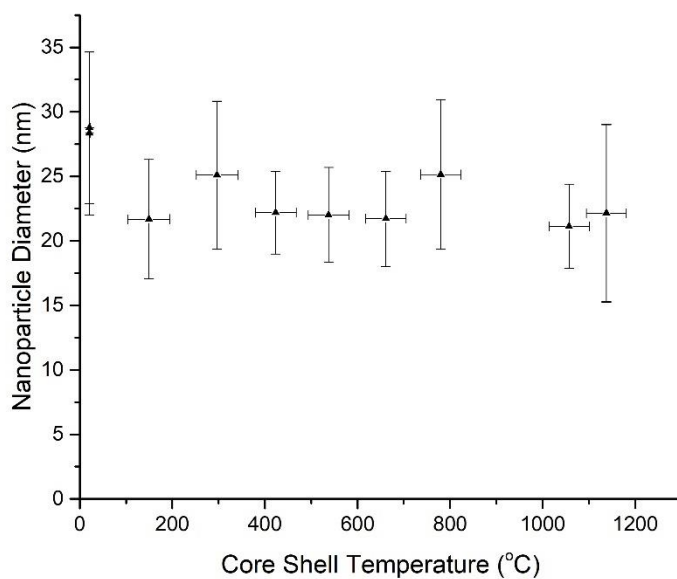


Figure 83 - The diameter of each 2-D pure Fe (no coolant) nanoparticle vs the temperature of the core shell evaporator. Plotted values are the means for the sample obtained from lognormal fitting with one sigma error bars.

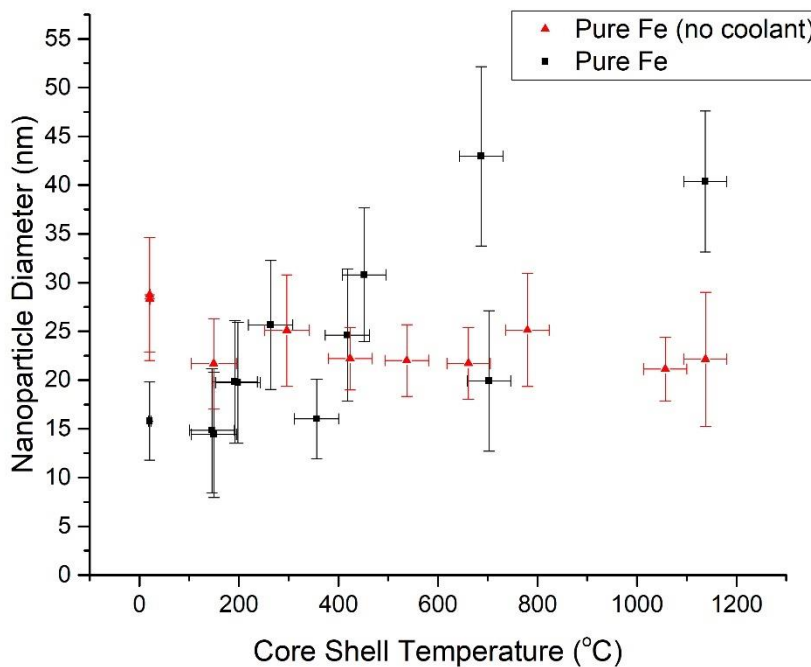


Figure 84 - Comparison of nanoparticle diameter for the 12 pure Fe TEM samples with the coolant supplied to the sputter head (black squares), and the 10 pure Fe (no coolant) TEM samples (red triangles).

From Figure 84, it is clear that the pure Fe samples without the coolant supplied to the sputter head have a different size dependence on core shell temperature than the samples with the coolant attached. The pure Fe (no coolant) samples follow a similar relationship to that of the Fe@Cu samples in *Chapter 5: Fe@Cu Studies*. Both the Fe@Cu samples and the pure Fe (no coolant) have a similar diameter to that of the pure Fe (with coolant) until approximately 700 °C, where the relationship with temperature bifurcates from that of the pure Fe (with coolant). The pure Fe (with coolant) samples increase in diameter up to ~ 40 nm at temperatures above 700 °C, whereas the Fe@Cu and the pure Fe (without coolant) diameters tend to stay below 35 nm (as for lower temperatures).

As investigated previously, the link between geometry factor and 2-D nanoparticle area (nm^2) was investigated for the pure Fe (no coolant) samples and is included in Figure 85. Interestingly, there are two distinct clusters of data points: one at 250 – 1000 nm^2 and with a geometry factor of 0.7 – 0.9, and the other around 0 – 500 nm^2 with a geometry factor of 0.1 – 0.3. In all previous samples analysed in this thesis, (pure Fe with coolant, Fe@Cu, and Fe@Ag), there is only one cluster in the top-left of the area versus geometry factor plot. This suggests that there are some nanoparticles with abnormal shapes that are elongated in one direction to give such a low geometry factor.

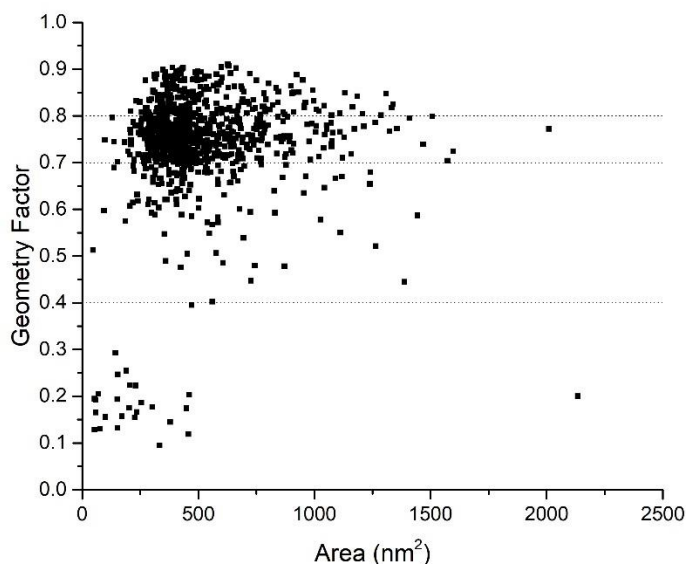


Figure 85 – Geometry factor versus area for all 1077 pure Fe (no coolant) nanoparticles analysed in this dataset. The dotted lines indicate the separation of the cubic (0.4 – 0.7), cuboctahedral (0.6 – 0.8), and spherical (0.8 – 1.0) regions.

The relationship between the 2-D area and the geometry factor was further investigated, as in the previous section, by splitting the area bins into their corresponding shape categories. The results of this analysis is plotted in Figure 86.

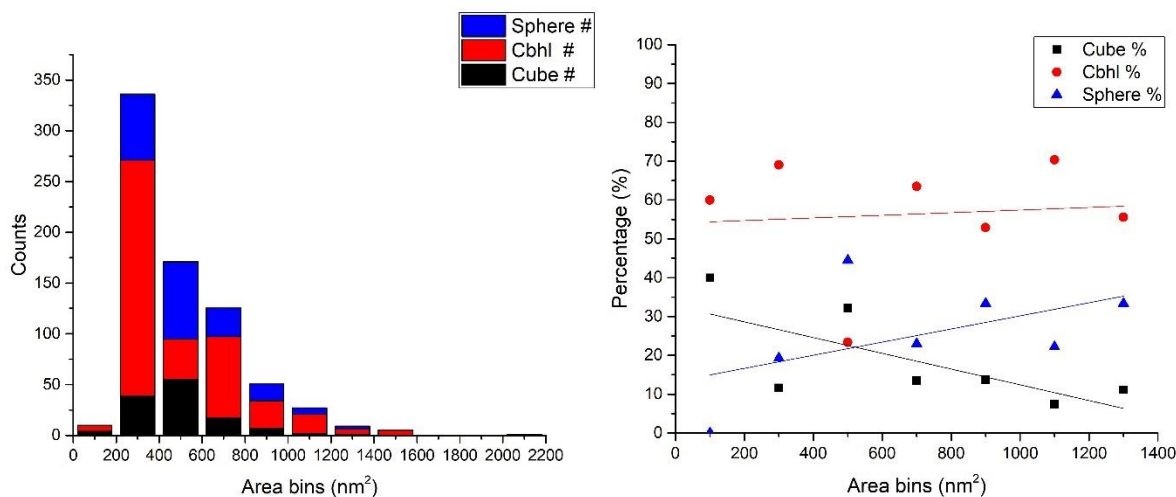


Figure 86 - Number of spheres (blue), cuboctahedrals/cbhl (red), and cubic (black) nanoparticles in each area bin (200 nm²) in size for the pure Fe (no coolant) samples.

Figure 86 shows that the majority of the nanoparticles analysed are within the 200 – 800 nm² range and are heavily dominated by cuboctahedral shaped nanoparticles. The cuboctahedral percentages remains relatively constant for each of the area bins. With the original pure Fe (coolant) samples, the percentages of the cubic and cuboctahedral nanoparticles decreased for larger areas, and the percentage of spheres drastically increased from ~ 20 % (0 – 200 nm²) up to ~ 85 % (1200 - 1400 nm²). For the pure Fe samples (no coolant) in Figure 86, this is not the case.

5 pure Fe (no coolant) samples were also prepared for magnetometry measurements. Figure 87 a) shows the magnetisation curves for the 5 samples measured over the full field range ± 5 T and at 5 K for an easy comparison of the saturation magnetisation values at each core shell temperature; Figure 87 b) shows an expanded view of the hysteresis behaviour in the field range ± 1 T. Figure 88 a) shows the corresponding information but at 300 K for ± 5 T with Figure 88 b) showing the data between ± 0.5 T.

Figure 87 and Figure 88 show that the magnetisation curves for all samples have the same general shape, and that the nanoparticles within these samples are blocked, as evidenced by the hysteresis loops present.

As in *Chapter 4: Pure Fe Studies* and in *Chapter 5: Fe@Cu Studies*, a Langevin function was fitted to the curves in Figure 87 and Figure 88. By fitting Langevin functions, the saturation magnetisation values were calculated and plotted against temperature. The error bars are \pm one sigma taken from the Langevin fits.

The magnetisation curves for our nanoparticles do not fit to a simple Langevin function, since they are modified by the hysteresis, but the lower and upper saturation limits of the magnetisation do converge to a Langevin. The saturation magnetisations obtained from these fits are used to give a value for the saturation magnetisation for each of our nanoparticle samples. These fits (\pm one sigma) are plotted in Figure 89.

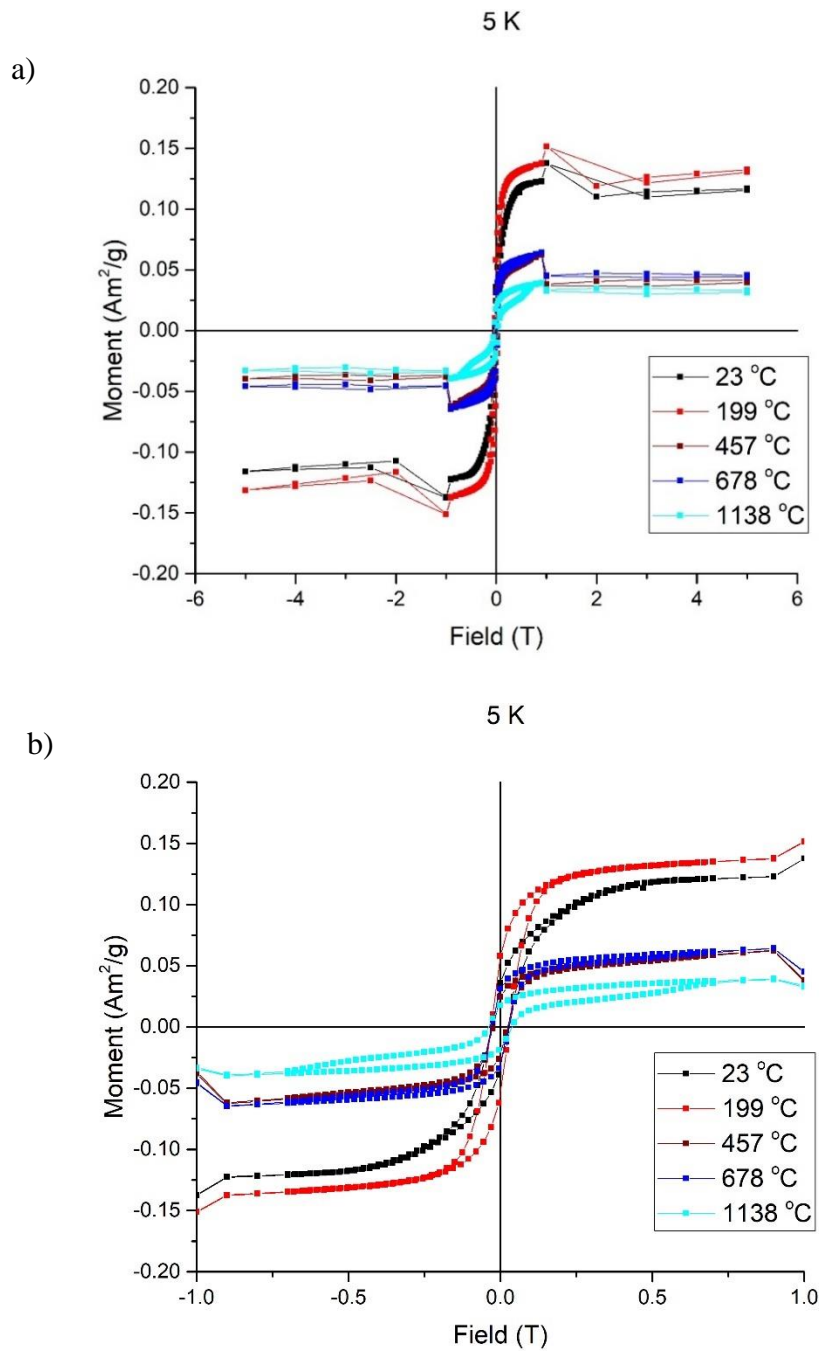


Figure 87 - Raw magnetometry data for the pure Fe (no coolant) samples from SQUID measurements at 5 K. a) shows the full data range obtained from -5 T to +5 T and b) shows the same data but between -1 T and +1 T to show the hysteresis behaviour in more detail.

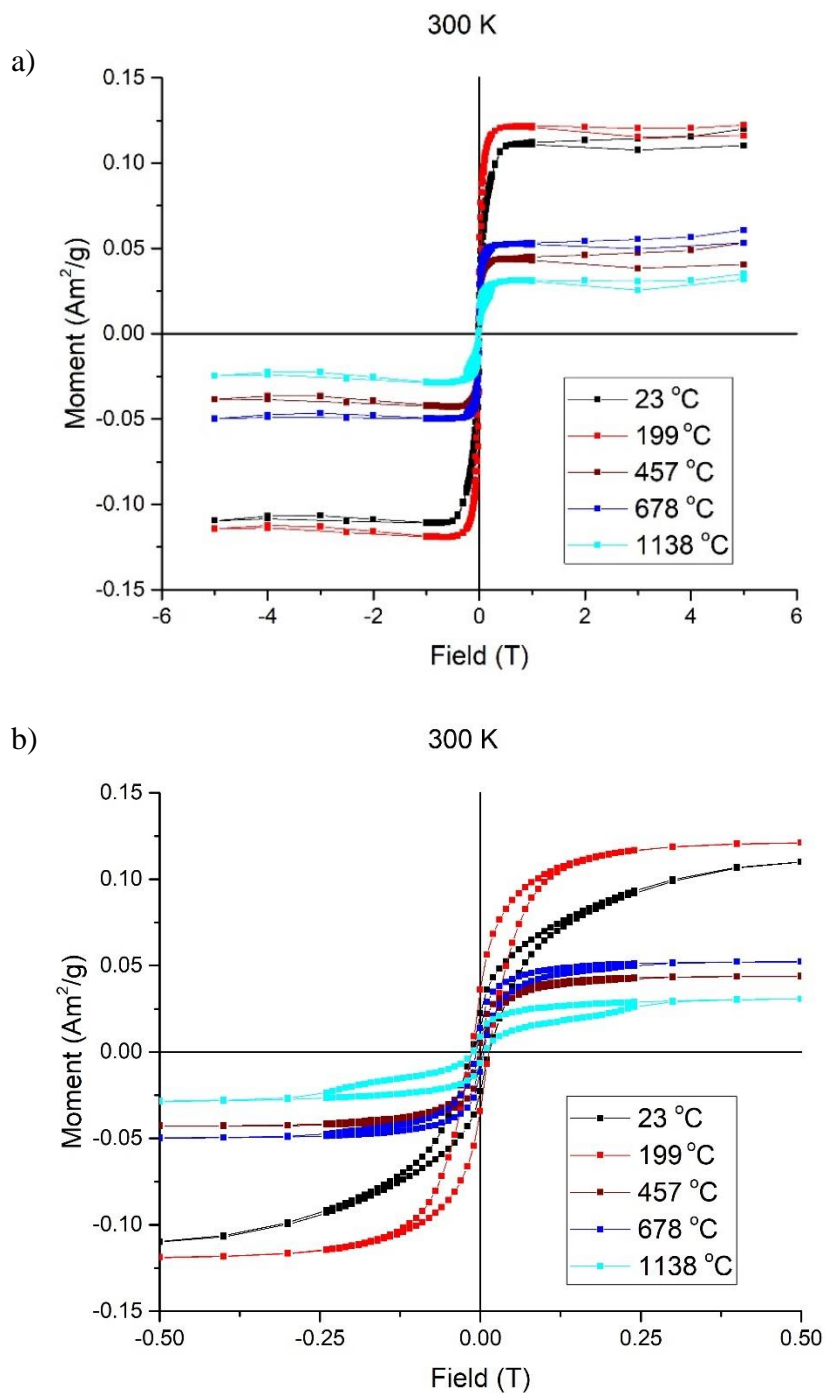


Figure 88 - Raw magnetometry from the pure Fe (no coolant) data from SQUID measurements at 300 K. a) shows the full data range obtained from -5 T to +5 T and b) shows the same data but between -1 T and +1 T to show the hysteresis behaviour in more detail.

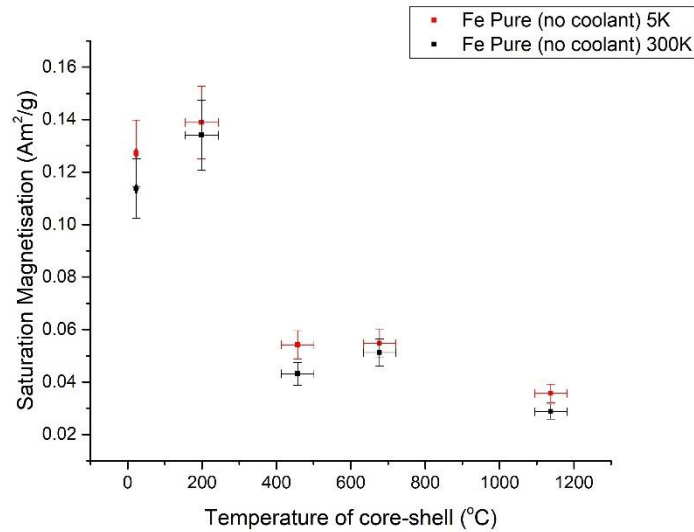


Figure 89 - Saturation Magnetisation obtained from Langevin fits of the raw hysteresis curves shown in Figure 87 and Figure 88, plotted against the temperature of the core shell evaporator to which the pure Fe (no coolant) nanoparticles were subjected.

Figure 89 shows the saturation magnetisation for the pure Fe (no coolant) samples as a function of core shell evaporator temperatures. The overall trend, as with the pure Fe (with coolant) samples is that the saturation magnetisation decreases with an increasing core shell temperature. The comparisons for both the 5 K and 300 K SQUID measurements for pure Fe samples (no coolant) and the pure Fe samples with coolant supplied are given in Figure 90. The saturation magnetisation values for the pure Fe samples without coolant supplied are up to $\sim 50\%$ lower than those for the pure Fe samples with the coolant supplied to the sputter head.

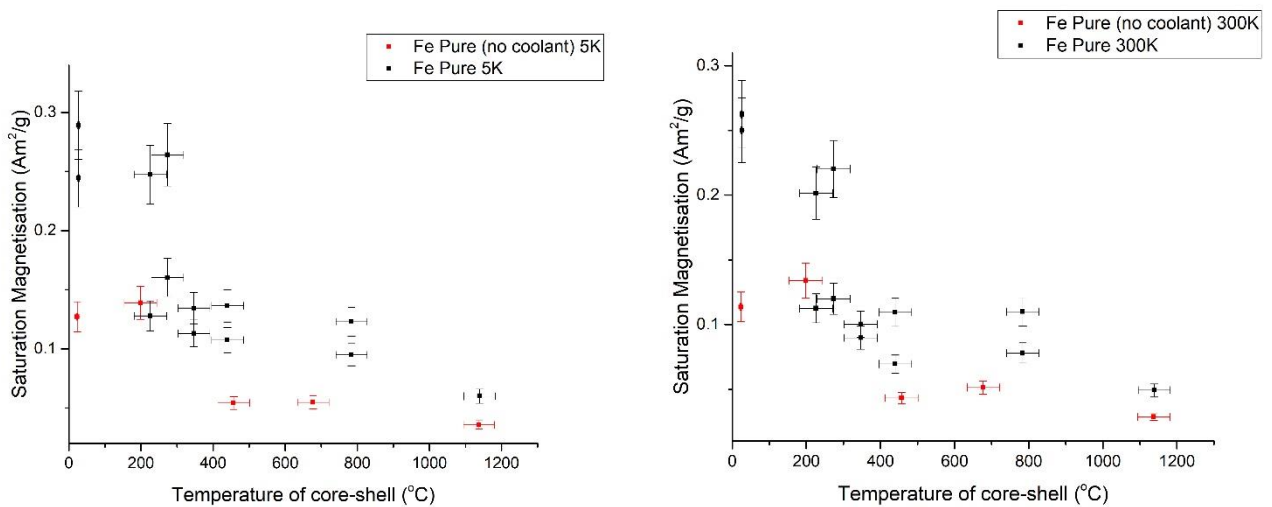


Figure 90 - Comparison of the saturation magnetisation of the pure Fe samples (no coolant, red) and the pure Fe samples (with coolant, black) obtained from Langevin fits to the raw magnetometry data for samples measured at 5 K (left) and 300 K (right).

3.4 Discussion

This section has detailed data from samples analysed with TEM and SQUID magnetometry for pure Fe samples with no coolant attached to the sputter head.

The geometry factor remains within the cuboctahedral range (0.7 – 0.8) for almost all temperatures investigated here, as seen in Figure 81. This differs from the pure Fe samples with the coolant supplied to the sputter head, for which the geometry factor tends to increase with an increasing core shell evaporator temperature.

The nanoparticle diameter for the pure Fe samples (without coolant) also differs from the corresponding observations for the pure Fe samples (with coolant). The nanoparticle diameter increased with an increasing core shell evaporator temperature when the coolant was supplied, but without the water cooling, the nanoparticle diameters appear to remain roughly constant as can be observed in Figure 83 and Figure 84.

The geometry factor versus 2-D nanoparticle area (nm^2) relationship was investigated for the pure Fe (no coolant) samples and is illustrated in Figure 85. Interestingly, there are two distinct clusters of data points; one at 250 – 1000 nm^2 and with a geometry factor of 0.7 – 0.9, and the other around 0 – 500 nm^2 and a geometry factor of 0.1 – 0.3. In all previous samples analysed in this thesis, (pure Fe (coolant), Fe@Cu (coolant), and Fe@Ag), there is only one cluster of data points in the top-left of the area versus geometry factor plot. This suggests in the case of the pure Fe (no coolant) samples there are some nanoparticles with abnormal shapes to give such a low geometry factor.

This was investigated further by splitting each area bin into its corresponding shapes. Figure 86 shows that the majority of the nanoparticles analysed are within the 200 – 800 nm^2 range and are heavily dominated by cuboctahedral shaped nanoparticles. The cuboctahedral percentages remains relatively constant for each of the area bins. For the original pure Fe (coolant) samples, the percentages of the cubic and cuboctahedral nanoparticles decreased for larger areas, and the percentages of spheres drastically increased from ~ 20 % (0 – 200 nm^2) up to ~ 85 % (1200 - 1400 nm^2). For the pure Fe samples (no coolant) in Figure 86, this is not the case.

The 5 samples on which magnetometry measurements were made all produced hysteresis curves, indicating that they are magnetically blocked, and are not superparamagnetic. The

saturation magnetisation values obtained from these plots decreased with increasing temperature and were, in some cases, ~ 50 % smaller than for the corresponding values for the pure Fe (with coolant) samples – see Figure 90.

4. No coolant Fe@Cu

4.1 Introduction

As was described in the previous section, when the core shell evaporator was operated at temperatures above 700 °C and the coolant was not supplied to the magnetron sputter source, the diameter of the pure Fe nanoparticles remained below 35 nm (see Figure 84). – in contrast to those prepared with coolant. Following the work described in *Chapter 5: Fe@Cu Studies*, it was decided to investigate the effect of coating the Fe nanoparticles (without coolant) with copper.

The following section details data obtained from 4 TEM samples, and 3 samples prepared for SQUID analysis, to investigate the effect of removing the water coolant to the sputter head on the nanoparticle size, shape, and magnetic properties.

4.2 Analysis Methods

This section starts with data obtained from TEM imagery, outlining the overall size and shape distributions of the nanoparticles. The 4 temperatures the nanoparticles were subjected to for TEM investigations and their information given in Table 8.

Core Shell Temperature (°C)	Number of Nanoparticles Analysed
693.1 ± 43.6	120
896.1 ± 43.3	100
1097.7 ± 43.2	110
1137.7 ± 43.2	126

Table 8 – Temperatures of the 4 Fe@Cu (no coolant) TEM samples produced and the number of nanoparticles analysed in each sample.

3 samples were also prepared for SQUID magnetometry and consisted of ~ 20 nm buffer layer of Ag, ~ 100 - 150 nm of 5 – 10 % volume fraction Fe in Ag, and a minimum cap of 50 nm Ag. The samples were deposited on Si (100) substrates of 7 mm x 5 mm and stored in gelatine capsules for ease of transportation and analysis. 3 samples were produced at the following core shell temperatures: 439.1 ± 44.2 °C, 773.6 ± 43.5 °C, 1137.7 ± 43.2 °C. For all samples, the total sample moment was measured as a fraction of applied magnetic field, at 5 K and at 300 K. The field was varied between ± 5 T.

The measurements enabled us to determine whether the nanoparticles were superparamagnetic or magnetically blocked. Saturation magnetisations and estimates for the heating that the particles could produce, were also obtained from the data.

As in previous chapters (*Chapter 4: Pure Fe Studies* and *Chapter 5: Fe@Cu Studies*), the moment per gram of Fe (Am^2/g) was plotted versus the magnetic field (T), yielding the magnetisation curve, which characterises the magnetic behaviour of the nanoparticle sample. This can be in the form of a hysteresis loop, dependent on the size of the nanoparticles produced and on the measurement temperature (see *Chapter 3: Magnetic Nanoparticle Theory and Medical Applications* for more information).

4.3 Results

As previously described earlier in this chapter, and in the chapters before this one, the geometry factor for each sample was separated into appropriate bins and plotted into a histogram. These histograms were then fitted with a 2-parameter Weibull distribution. An example of this fitting is provided in Figure 91, for the sample produced at 693.1 ± 43.6 °C.

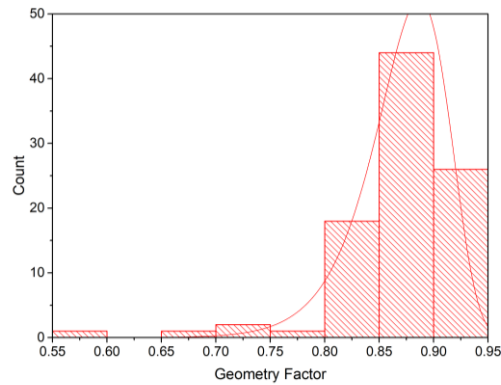


Figure 91 – Fe@Cu (no coolant) sample produced at 693.1 ± 43.6 °C with the Weibull fitting overplotted (red line).

Fitting the measured distributions to the Weibull distributions allows one to assign a mean value for the geometry factor, along with a \pm one sigma value, for each core shell temperature. These are plotted in Figure 92 with dotted lines to indicate the separation of the 3 regions of interest: cubic (0.4 – 0.7), cuboctahedral (0.7 – 0.8), and spherical (0.8 – 1.0).

Figure 92 does not indicate any clear shift in geometry factor across the range of core shell evaporator temperatures investigated. As mentioned in the previous chapter (*Chapter 4: Pure Fe Studies*), the geometry factor of the pure Fe samples was found to increase into the spherical regime with increasing temperature of the core shell evaporator. Here, however, the geometry factor of the Fe@Cu (no coolant) samples remains mostly within the cuboctahedral range.

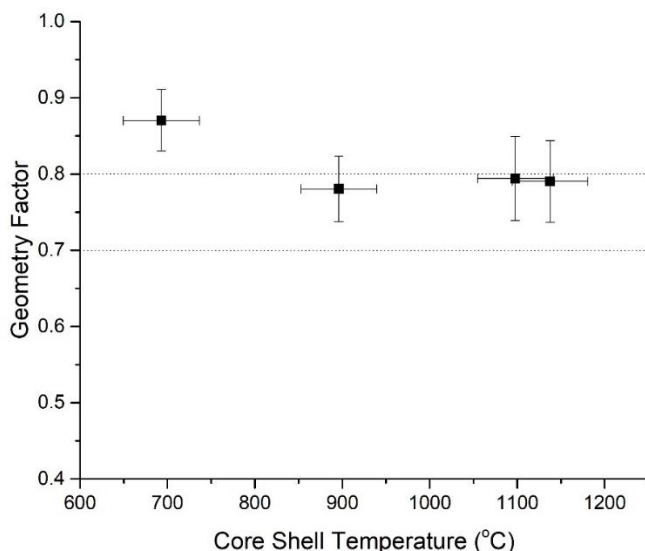


Figure 92 – Geometry factor for the 4 Fe@Cu (no coolant) TEM samples produced with the core shell evaporator loaded with ~ 1 g Cu. The dotted lines indicate the separation of the cubic (0.4 – 0.7), cuboctahedral (0.7 – 0.8), and spherical (0.8 – 1.0) regions. The values come from Weibull fits of the raw data with ± 1 sigma error bars.

Figure 93 compares the geometry factor of the Fe@Cu (no coolant) with the geometry factor of the Fe@Cu (with coolant supplied). There is no significant difference between the two sets of samples, both remaining within the cuboctahedral range (0.7- 0.8).

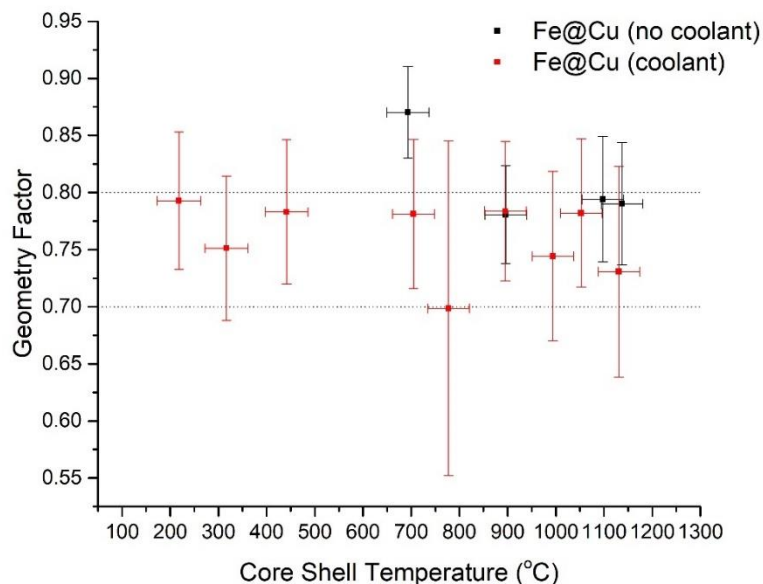


Figure 93 - Geometry factor for the 9 Fe@Cu (with coolant) TEM samples (red) and the 4 Fe@Cu (no coolant) TEM samples (black) produced with the core shell evaporator. The dotted lines indicate the separation of the cubic (0.4 – 0.7), cuboctahedral (0.7 – 0.8), and spherical (0.8 – 1.0) regions. The values come from Weibull fits of the raw data with ± 1 sigma error bars.

Figure 94 splits the percentage of cubic, cuboctahedral, and spherical shaped nanoparticles against the core shell temperature investigates the trends in the shape change that may be overlooked when plotting only the mean geometry factor (\pm one sigma error bars) as in Figure 92 and Figure 93. The percentage of spherical nanoparticles decreases, and the percentage of cuboctahedral nanoparticles increased with an increased core shell evaporator temperature. The cubic nanoparticle percentages remain very low throughout the temperature range. For the Fe@Cu samples with the coolant attached, the percentage of cuboctahedrals decreased, the percentage of cubes increased, and the sphere percentages decreased as the temperature of the core shell evaporator was increased.

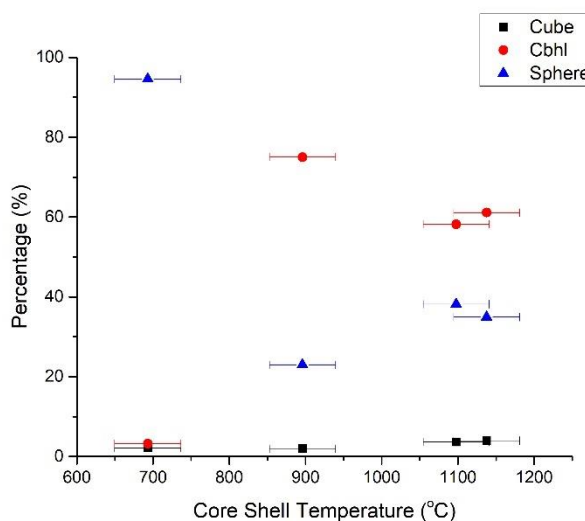


Figure 94 - The percentage of cubes (geometry factor 0.4 -0.7, black squares), cuboctahedrals (0.7 – 0.8, red circles) and spheres (0.8 - 1.0, blue triangles) versus the core shell temperature when loaded with ~ 1 g of Cu.

Figure 95 plots the nanoparticle diameter (\pm one sigma error bars) from lognormal distributions of the raw area measurements from TEM images. The comparison of Fe@Cu (no coolant) and Fe@Cu (coolant) diameters are plotted in Figure 96. From this, it can be seen that there appears to be no obvious trend between the diameter of the nanoparticles and the core shell evaporator temperature. It is also clear that the particle diameters do not drastically differ from the Fe@Cu (coolant) samples, bar the 693.1 ± 43.6 °C sample, although this had an abnormally large diameter and sigma value. Also, this sample did not follow a regular lognormal distribution, rather a normal distribution.

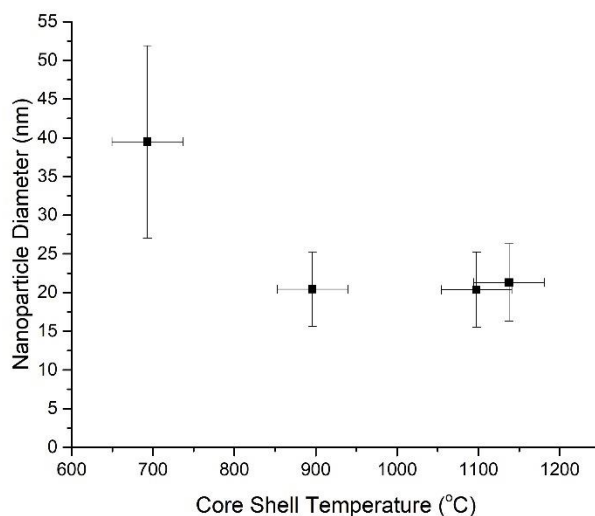


Figure 95 - The diameter of each 2-D Fe@Cu (no coolant) nanoparticle vs the temperature of the core shell evaporator. Plotted values are the means for the sample obtained from lognormal fitting with one sigma error bars.

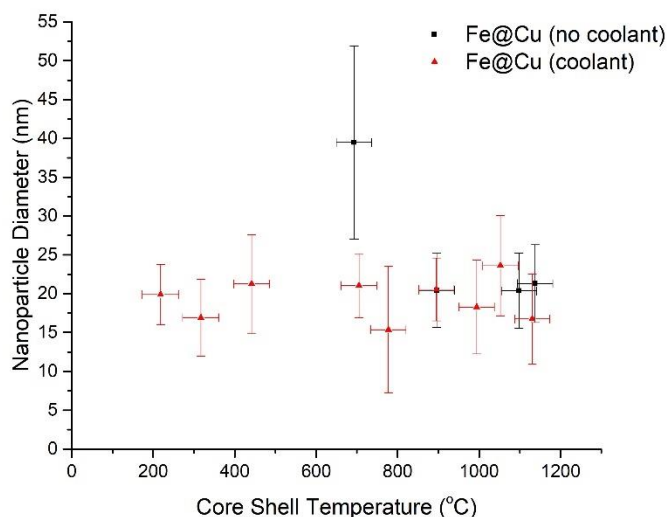


Figure 96 - The diameter of each 2-D nanoparticle vs the temperature of the core shell evaporator for the Fe@Cu (no coolant) samples (black squares) and the Fe@Cu (with coolant) samples (red triangles). Plotted values are the means for the sample obtained from lognormal fitting with \pm one sigma error bars.

As with previous samples, the relationship between the 2-D area of the nanoparticles and their geometry factor was investigated, and the raw data is plotted in Figure 97. Here, as in previous samples, there is a cluster in the top left corner of the plot, between 0 – 500 nm² and a geometry factor between 0.7 - 0.9. Here, the samples have been split into their temperatures to investigate the difference between them, and if the 693.1 ± 43.6 °C sample still remains anomalous.

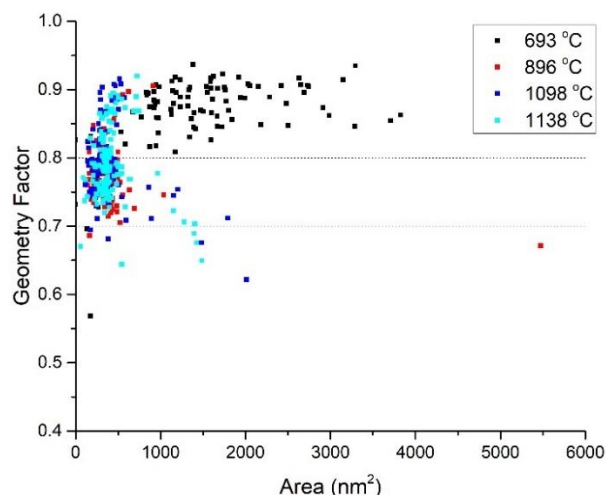


Figure 97 – Geometry factor versus area for all 456 nanoparticles analysed in the Fe@Cu (no coolant) dataset. The dotted lines indicate the separation of the cubic (0.4 – 0.7), cuboctahedral (0.7 – 0.8), and spherical (0.8 – 1.0) regions.

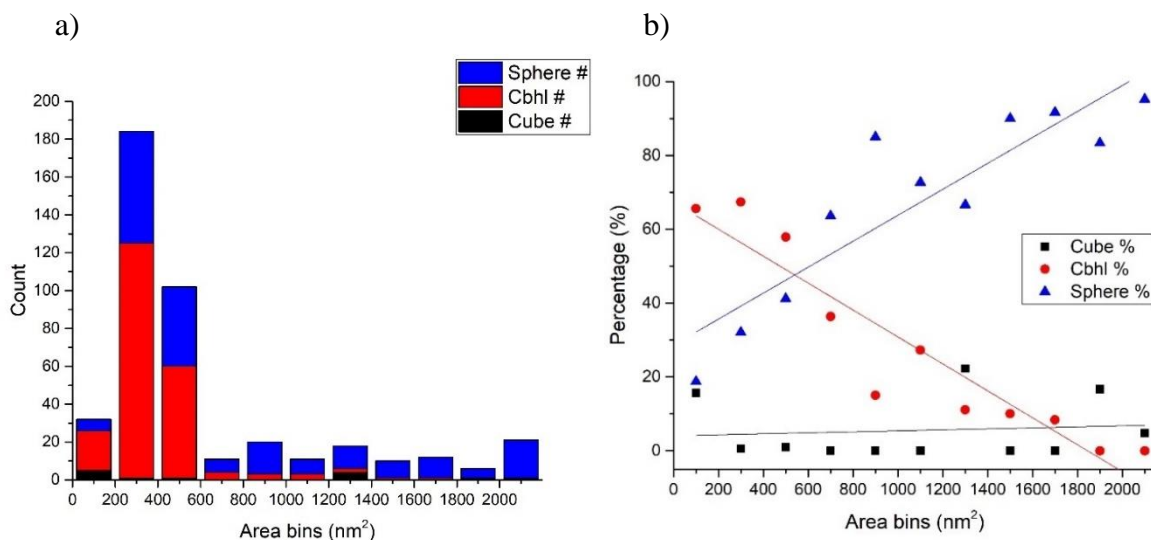


Figure 98 - Number of spheres (blue), cuboctahedrals/cbhl (red), and cubic (black) nanoparticles in each area bin (200 nm²) in size for the Fe@Cu (no coolant) samples.

The raw data in Figure 97 was then split into 200 nm² area bins and into their corresponding shape categories to investigate this relationship further. Figure 98 a) shows that the majority of the nanoparticles have an area between 200 nm² and 400 nm², and that the nanoparticles within this range are mostly cuboctahedral. Figure 98 b) gives the percentage of each shape for the area bins and shows an increase in spherical nanoparticles, a decrease in cuboctahedral nanoparticles, and that the cubic percentages remain roughly constant when the size of the nanoparticle increases. This is in contrast to the Fe@Cu samples created with coolant attached, whereby the cubic percentages

drastically increased, while the spherical and cuboctahedral percentages decreased with increasing particle area.

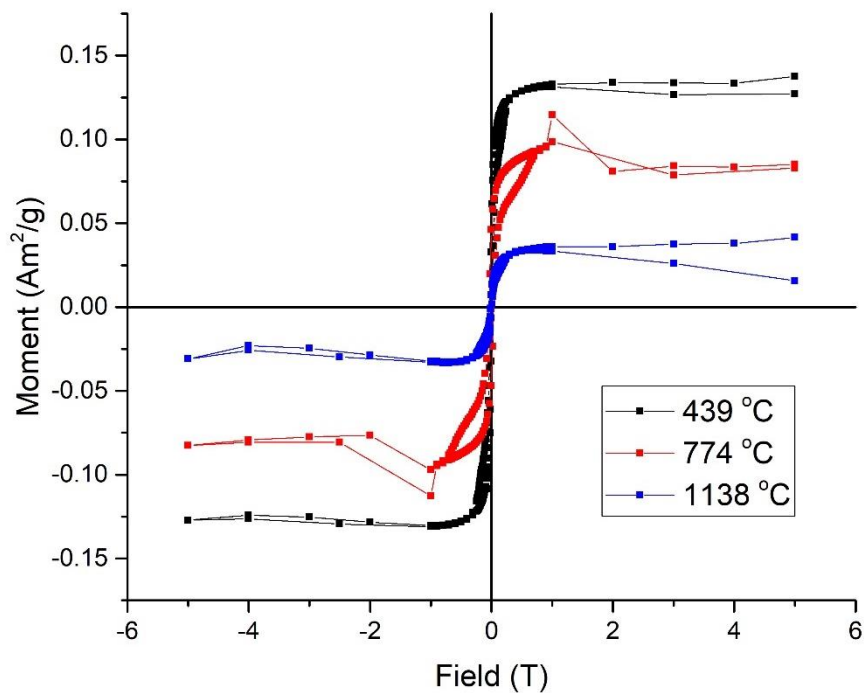
Following the TEM analysis, 3 samples were prepared for magnetometry measurements. Figure 99 a) shows the magnetisation curves for the 3 samples over the full field range ± 5 T at 300 K for an easy comparison of the saturation magnetisation values at each core shell temperature, whereas Figure 99 b) shows an expanded view of the hysteresis behaviour in the field range ± 1 T. Figure 100 a) shows the corresponding information but at 5 K for ± 5 T, Figure 100 b) showing this information between ± 0.5 T to highlight the hysteresis behaviour of the nanoparticles more clearly.

Figure 99 and Figure 100 show that the magnetisation curves for all 3 samples have the same general shape, and that the nanoparticles within these samples are blocked since hysteresis loops are present in the data at both measurement temperatures.

As before, a Langevin function was fitted to the curves plotted in Figure 99 and Figure 100. By fitting Langevin functions, the saturation magnetisation values were obtained and plotted against core shell temperature. The error bars are \pm one sigma taken from the Langevin fits.

As mentioned previously, the magnetisation curves for our nanoparticles do not fit to a simple Langevin function, since they are modified by the hysteresis, but the lower and upper saturation limits of the magnetisation do converge to a Langevin. The saturation magnetisations obtained from these fits are used to give a value for the saturation magnetisation for each of our nanoparticle samples. The results of such fits (\pm one sigma) are plotted in Figure 101.

a)



b)

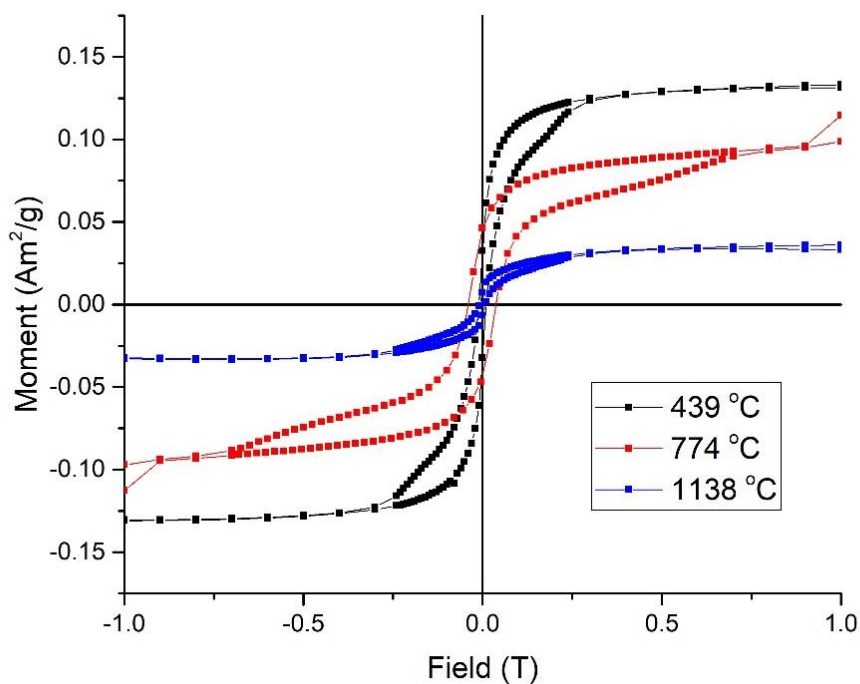


Figure 99 - Raw data from SQUID magnetometry of the Fe@Cu (no coolant) samples with measurements at 300 K. a) shows the full data range obtained from -5 T to +5 T and b) shows the same data but between -1 T and +1 T to show the hysteresis behaviour in more detail.

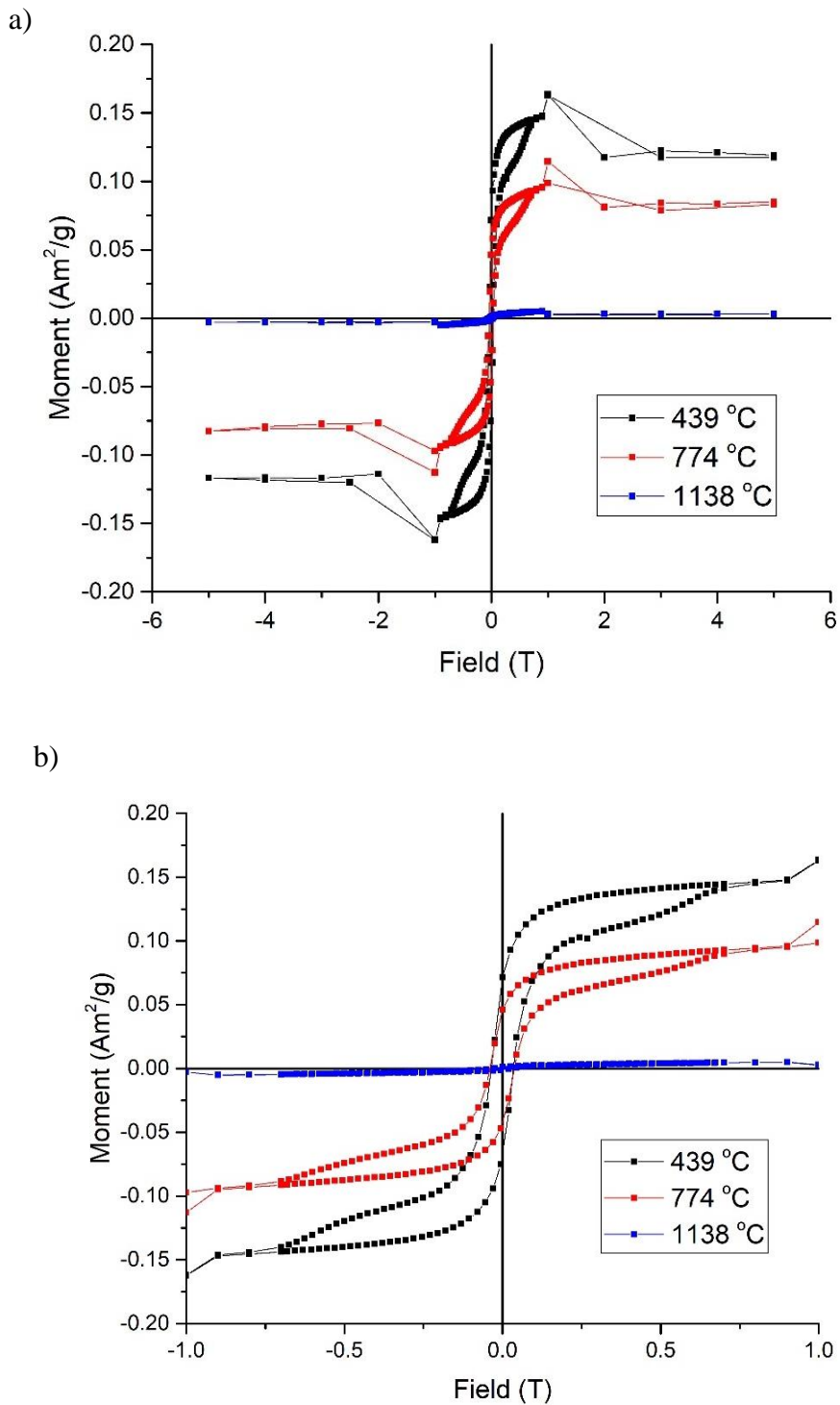


Figure 100 - Raw data from SQUID magnetometry of the Fe@Cu (no coolant) samples with measurements at 5 K. a) shows the full data range obtained from -5 T to +5 T and b) shows the same data but between -1 T and +1 T to show the hysteresis behaviour in more detail.

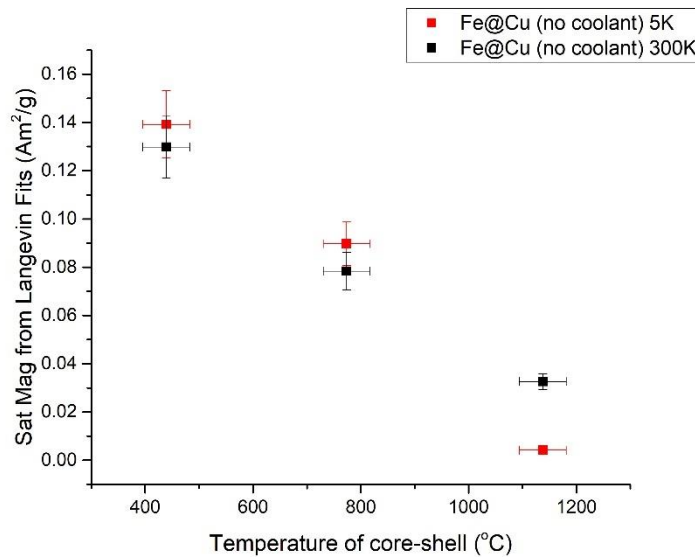


Figure 101 - Saturation Magnetisation from Langevin fits of the raw hysteresis curves shown in Figure 99 and Figure 100, plotted against the temperature of the core shell evaporator that the Fe@Cu (no coolant) nanoparticles were subjected to.

Figure 101 shows, as with all previous sets of samples, that an increase in core shell evaporator temperature decreased the saturation magnetisation of the Fe@Cu (no coolant) samples within the 300 K and 5 K measurements. Comparison with the Fe@Cu (coolant) saturation magnetisation values are given in Figure 102. There is no significant difference in the magnitudes of the two samples, apart from for the Fe@Cu (no coolant) sample at 1137.7 ± 43.2 °C, where the saturation magnetisation values at 5 K and 300 K are much lower than for the equivalent Fe@Cu (coolant) sample.

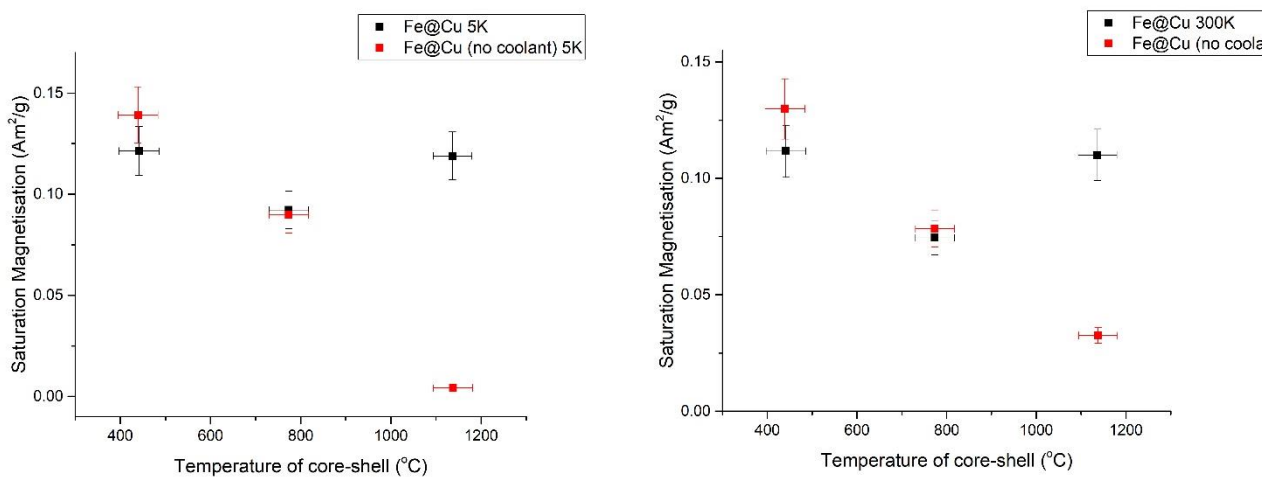


Figure 102 - Saturation Magnetisation of the Fe@Cu (no coolant) sample (red), and the Fe@Cu (coolant) sample (black) plotted against the temperature of the core shell evaporator for the 5 K (left) and 300 K (right) measurements in the SQUID magnetometer.

The saturation magnetisation values for the Fe@Cu (no coolant) samples were then compared with the pure Fe (no coolant) samples and given in Figure 103. Again, there is no significant difference between the two samples, indicating that addition of Cu (assumed) to the nanoparticles does not detrimentally affect their saturation magnetisation.

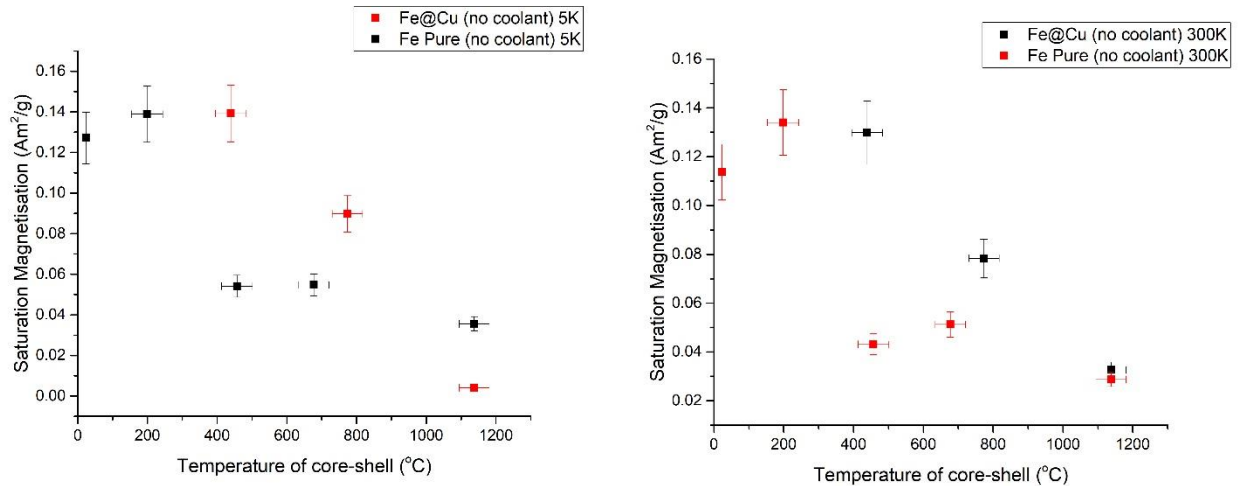


Figure 103 - Saturation Magnetisation of the Fe@Cu (no coolant) sample (red), and the pure Fe (no coolant) sample (black) plotted against the temperature of the core shell evaporator for the 5 K (left) and 300 K (right) measurements in the SQUID magnetometer.

The Fe@Cu (no coolant) tend to perform just as well, if not slightly better, than the pure Fe (no coolant), as seen in Figure 103. This is consistent with the samples where coolant is attached to the sputter head in *Chapter 4: Pure Fe Studies* and *Chapter 5: Fe@Cu Studies*, whereby the addition of Cu did not drastically decrease the saturation magnetisation of the samples.

4.4 Discussion

The geometry factor of the Fe@Cu (no coolant) samples did not change throughout the temperature increase of the core shell evaporator, unlike the pure Fe (coolant) samples for which the geometry factor increased with an increasing core shell evaporator temperature. The particle shapes did, however, remain mostly in the cuboctahedral range (0.7 - 0.8), as for the Fe@Cu (coolant) samples in *Chapter 5: Fe@Cu Studies*, as seen in Figure 93.

Figure 95 plots the nanoparticle diameter (\pm one sigma error bars) from lognormal distributions of the raw 2-D area measurements from TEM images. The comparison of diameters for Fe@Cu (no coolant) and Fe@Cu (coolant) is given in Figure 96. Here, there appears to be no obvious trend between the diameter of the nanoparticles and the core shell evaporator temperature; there is also no significant difference between the Fe@Cu (no coolant) and Fe@Cu (coolant) samples, except for the 693.1 ± 43.6 °C sample which had an abnormally large diameter and sigma values. (This sample also did not follow a regular lognormal distribution, which may well indicate an anomalous sample. Production of additional samples would be required to investigate this relationship further).

Figure 97 shows the area and geometry factor for all 453 nanoparticles analysed within this section. Here, the 693.1 ± 43.6 °C sample again appears to follow a different relationship than the other samples, stretching out across the higher area ranges, whereas the others remain within $\sim 0 - 500$ nm².

The raw data in Figure 97 was then split into 200 nm² area bins and into their corresponding shape categories to investigate this relationship further. Figure 98 a) shows the majority of the nanoparticles have an area between 200 nm² and 400 nm², and the nanoparticles within this range are mostly cuboctahedral. Figure 98 b) gives the percentage of each particle shape for the area bins and shows an increase in spherical nanoparticles, a decrease in cuboctahedral nanoparticles, and that the cubic percentages remain roughly constant when the size of the nanoparticle increases. This is in contrast to the Fe@Cu (with coolant) samples whereby the cubic percentages drastically increased, with the spherical and cuboctahedral percentages decreasing with increased particle area.

The 3 samples on which magnetometry measurements were made produced hysteresis curves, indicating their blocked behaviour. Their saturation magnetisation values were within a similar range to the Fe@Cu (coolant) samples from *Chapter 5: Fe@Cu Studies*, (apart from the 1137.7 ± 43.2 °C, where the saturation magnetisation values at 5 K and 300 K are much lower than the Fe@Cu (coolant) samples, see Figure 102). Figure 103 compares the pure Fe (no coolant) and the Fe@Cu (no coolant) samples, and shows that their values are very similar, indicating that the addition of Cu to the system when there is no coolant supplied to the sputter head, does not drastically affect the magnetic properties of the nanoparticles.

A lack of EDX data does not allow us to definitively claim that Cu has attached to the samples, although the data here does suggest that the nanoparticles are very similar to the Fe@Cu samples analysed in *Chapter 5: Fe@Cu Studies*, leading to the belief that these attaching to the nanoparticles are will lead to alloying between the Fe and Cu.

5. Conclusions

The Fe@Ag samples produced cannot definitely be proven with the TEM data discussed here to contain any Ag, but their shape and size analysis was carried out in detail. The geometry factor was found to be indistinguishable from that for the pure Fe samples from *Chapter 4: Pure Fe Studies*, as shown in Figure 75. The nanoparticle diameter also did not appear to deviate from the pure Fe samples when plotted alongside, as in Figure 78.

Comparisons between the geometry factor and the 2-D area of the Fe@Ag nanoparticles were also investigated; an apparent difference was noted compared to the data for the pure Fe samples from *Chapter 4: Pure Fe Studies*, as the majority of the pure Fe samples were within the 0 – 400 nm² range. However, this is almost certainly due to the number of samples produced at a temperature lower than the temperatures investigated for the Fe@Ag samples. If the lower area ranges are ignored when comparing these two sample sets, the percentages of cubes, cuboctahedrals, and spheres are not dissimilar.

In light of these outcomes, and due to a lack of EDX data, it must be concluded that significant amounts of Ag have not attached to the Fe cores, and that any attachment of Ag is small enough to have no significant effect on the nanoparticle shape or sizing. EDX data would clearly be a valuable addition to this analysis.

The two sections following the section describing the work on Fe@Ag samples investigated the impact, if any, of removing the water coolant from the sputter head, as previous research indicated that this produces nanoparticles with a lower diameter. However, the diameters for the pure Fe (no coolant) and the Fe@Cu (no coolant) samples analysed here, do not differ very much from their corresponding samples with the added coolant in *Chapter 4: Pure Fe Studies* and *Chapter 5: Fe@Cu Studies* (as shown in Figure 84 and Figure 96). Although the pure Fe (no coolant) samples do produce smaller nanoparticles at temperatures above 700 °C, below this their diameters are similar to those for the pure Fe (coolant) samples.

There are a few differences that can be noted for particles produced when the sputter head is lacking water coolant. The geometry factor for the pure Fe (no coolant) samples remained within the cuboctahedral range (0.7 – 0.8) for almost all temperatures investigated here, as can be seen in Figure 81. This differs from the data for the pure Fe samples with coolant supplied to the sputter head, which tends to increase with an increasing core shell evaporator temperature. The Fe@Cu (no coolant) geometry factor across the temperature range investigated here does not differ from the Fe@Cu (coolant), as Figure 93 shows.

The magnetometry measurements showed that all the nanoparticles synthesised without water coolant are magnetically blocked and are not superparamagnetic. The saturation magnetisation values for the pure Fe (no coolant) samples decreased with increasing temperature and were, in some cases, ~ 50 % times smaller than for the samples with coolant – see Figure 90.

However, Figure 102 shows there is little difference between the saturation magnetisation values of the Fe@Cu (coolant) and the Fe@Cu (no coolant) samples, which is unsurprising as most of the TEM analysis indicated there is almost no difference between these two sets of samples.

In conclusion, the removal of water coolant does not produce pure Fe nanoparticles with a lower diameter range, unless the temperature of the core shell evaporator is above 700 °C. Previously, it was suggested that Fe could be re-evaporating from the crucible, causing such an increase in the case of Fe particles produced with coolant. However, this does not seem to be the case here, possibly due to the repeated use of the same crucible for the first set of samples, and the use of a different (new) crucible for the later sample sets. This highlights some of the technical issues associated with producing core shell nanoparticles from the gas phase.

Chapter 7: Conclusions

This work included a variety of novel techniques to characterise a range of nanoparticle systems, and set out to expand upon the work of my predecessors (Atkas, et al., 2015; Atkas S. , 2014; Binns, et al., 2012; Pratt, et al., 2014). Extensive image analysis coupled with magnetometry has not only expanded on previous research but has highlighted new avenues of investigation.

To summarise, the previous 3 chapters report on the synthesis and analysis of 5 distinct sample sets of Fe nanoparticles: pure Fe, Fe@Cu, Fe@Ag, pure Fe (no coolant), and Fe@Cu (no coolant). Investigations were carried out by means of TEM, EDX, and also SQUID magnetometry measurements. Brief findings of these investigations are summarised below in Table 9, where only the Pure Fe (coolant) sample possibly behaving differently to the other 4 samples.

Sample	Response to an increasing core shell evaporator temperature		
	Nanoparticle Diameter response	Geometry Factor response	Saturation Magnetisation response
Pure Fe (coolant)	Possible increase	Possible increase	Decrease
Fe@Cu (coolant)	No change	No change	Decrease
Fe@Ag	No change	No change	Decrease
Pure Fe (no coolant)	No change	No change	Decrease
Fe@Cu (no coolant)	No change	No change	Decrease

Table 9 – Summary of the nanoparticle diameter, the geometry factor, and the saturation magnetisation responses of the 5 samples investigated in this thesis with an increased core shell evaporator temperature. Interestingly, the nanoparticle diameter and geometry factor across all samples is not significantly affected by the temperature of the core shell evaporator. The specific shape percentages (cube/cuboctahedra/sphere), however, are different for each sample. This is interesting when compared with the consistent decline in saturation magnetisation as previous studies tend to link this with shape change – not observed here (Atkas S. , 2014).

During these investigations, some technical issues were highlighted with regard to the core shell crucible. It was suggested that at high crucible temperatures Fe could be re-evaporating from the crucible ends, causing an increase in the particle diameter. Such an increase in diameter was seen in the data presented in *Chapter 4: Pure Fe Studies* and indicated in Table 9, where the crucible was repeatedly used for samples previous to this

project. This hypothesis was further supported by the lack of a particle diameter increase for the pure Fe (no coolant) samples; for these samples, a different (new) crucible was used, and was therefore assumed to contain little to no Fe deposited on the inside of the cell. An increase in particle diameter was also not observed in the Fe@Cu and Fe@Ag samples, most likely due to the high vapour pressure of Cu or Ag within the evaporator inhibiting or attenuating the progress of any Fe evaporated from the crucible end back towards the centre of the cell.

A second technical difficulty related to the process of forming a full shell of material around the Fe cores. The Mg and Al attempts both failed to produce any Mg or Al on the nanoparticles according to EDX analysis. Previous studies by the group using the same cluster source showed that Ag does not produce a complete shell, rather multiple clusters of Ag atoms at the Fe core surface, where the Ag more favourably binds to itself rather than to the Fe (Pratt, et al., 2014). This is somewhat surprising from the point of view of lattice match, as fcc Ag and bcc Fe structures match closely if one structure is rotated by 45° relative to the other. This may well have something to do with the surface energy of these nanoparticles, or perhaps their relative thermal conductivities, but this would require further research and investigation to discern.

Chapter 5: Fe@Cu Studies outlines the analysis of Fe@Cu core shell nanoparticles, produced when ~ 1 g of Cu was inserted into the crucible. The EDX data shows that there is Cu coverage on all of the samples investigated, but with low proportions of Cu. The EDX maps in *Chapter 5: Fe@Cu Studies* show Cu signals originating from areas other than the nanoparticle, indicating that there is also some Cu leakage from the core shell evaporator into the deposition. The density of the Cu signal, however, is higher at the nanoparticle locations, indicating that the inclusion of Cu on the Fe nanoparticles is significant. The fact that the Cu signal is strongest from the centre of the nanoparticles is more suggestive of alloying rather than shell formation.

Even with these technical issues, our best performing pure Fe nanoparticles have a saturation magnetisation higher than that of bulk pure Fe ($0.220 \text{ Am}^2/\text{g}$) of $0.262 \pm 0.026 \text{ Am}^2/\text{g}$ at 300 K. These nanoparticles were produced at room temperature ($21 \text{ }^\circ\text{C} \pm 2 \text{ }^\circ\text{C}$), have a mean diameter of ~ 18 nm, and a geometry factor of ~ 0.8 , indicating they are likely to contain mostly cuboctahedral shapes. The observation of hysteresis at 300 K shows that they are magnetically blocked. Hence any heating that they produce in an AC

magnetic field will arise from hysteresis heating (which is more efficient than superparamagnetic heating - see *Chapter 3: Magnetic Nanoparticle Theory and Applications*).

The magnetometry curves in *Chapter 5: Fe@Cu Studies* indicate that the Fe@Cu nanoparticles are also “blocked,” like the pure Fe nanoparticles in the previous chapter. Considering the change in geometry factor between the higher temperature ranges (between 0.7 - 0.8 for the Fe@Cu samples and > 0.8 for the pure Fe samples), this indicates that the shape of the nanoparticle does not drastically affect its saturation magnetisation.

The data in *Chapter 5: Fe@Cu Studies* show an increase in the production of cubic nanoparticles as the temperature of the core shell evaporator is increased. This contrasts with the observations for the pure Fe nanoparticles (in the previous chapter) whereby the percentages of cubic nanoparticles drastically decreased with an increased evaporator temperature. As discussed previously, this is consistent with a reduced surface energy in Cu relative to Fe. This is particularly interesting for MRI relaxivity as Atkas, et al., (2015) reported that samples with a higher cubic content performed better as image enhancers for that technique. However, as stated previously, the nanoparticle shape does not appear to affect the saturation magnetisation. It is clear that further studies are required to understand the complicated mechanisms between the nanoparticle structure and its magnetic behaviour.

The Fe@Ag samples analysed here did not show any abnormal morphology as suggested in Pratt, et al., (2014). Also, there is no apparent deviation from the pure Fe samples (*Chapter 4: Pure Fe Studies*) in nanoparticle diameter, geometry factor, or the percentages of cubes, cuboctahedrals, and spheres for each core shell evaporator temperature. In the light of these outcomes, and due to a lack of EDX data, it must be concluded that significant amounts of Ag have either not attached to the Fe cores, or that any attachment of Ag is small enough not to have any significant effect on the nanoparticle shape or sizing. It should be noted that Fe and Ag do not alloy, so any Ag inclusion will be on the surface of the Fe nanoparticles

The effect, if any, of removing the water coolant from the sputter head was investigated in *Chapter 6: Other Core Shell Studies*. Previous in-house research had indicated that

this produces a lower nanoparticle diameter. However, the diameters for the pure Fe (no coolant) and the Fe@Cu (no coolant) samples analysed here, do not differ significantly from their corresponding samples with added coolant in *Chapter 4: Pure Fe Studies* and *Chapter 5: Fe@Cu Studies*. The data presented here does suggest that pure Fe samples (no coolant) do appear to have smaller nanoparticles at temperatures above 700 °C, but below this, their diameters are much the same as for the pure Fe (coolant) samples. As mentioned previously, though, this is most likely due to technical factors rather than anything fundamentally different between these two sample sets. Or, perhaps, the 3 data points above 700 °C in the Pure Fe (coolant) sample are in doubt.

The magnetometry measurements showed that all the nanoparticles synthesised without water coolant are magnetically blocked, and not superparamagnetic. Given that a significant decrease in particle size could have led to the onset of superparamagnetic behaviour, this is consistent with the TEM results.

Further work on the Fe@Ag samples would include EDX analysis on the Fe@Ag samples as this should reveal the extent of any Ag coverage on the Fe cores. Since the atomic moments in Fe nanoparticles embedded in a Ag matrix are known to be comparable with those in bulk Fe (Binns, et al., 2012) the same should be true for Fe@Ag nanoparticles (assumed the formation of complete Ag shells). Magnetometry measurements would confirm this, and form part of the further work required for this system.

From a technical viewpoint, reducing the amount of Fe re-evaporated from the core shell crucible ends is an important consideration. Some form of additional shielding and/or additional cooling to the crucible ends could provide a solution.

One particular outcome of interest from this work is that the Fe@Ag samples did not produce interesting shapes as detailed in Pratt, et al. (2014); they remained similar to the Pure Fe samples in appearance. Another fascinating result is the magnetisation saturation values decrease with an increased core shell temperature but does not appear to be due to a shape change as previously hypothesised (Atkas, et al., 2015) as all the samples have a decreasing magnetisation saturation (and polygon area) with an increasing core shell temperature, regardless of the cubic, cuboctahedral, and spherical percentages.

Further methods of investigating our nanoparticle performance would, of course, be beneficial. From a measurement viewpoint, an AC magnetometer would be highly

valuable. This would yield hysteresis plots for our samples at differing magnitudes of applied magnetic field. From this an appropriate frequency could be selected (ensuring that their combination remains below the Atkinson-Brezovich limit, $H_o \times f, = 4.85 \times 10^8 \text{ Am}^{-1} \text{ s}^{-1}$ (Atkinson, Brezovich, & Chakraborty, 1984), see *Chapter 3: Magnetic Nanoparticle Theory and Applications*), and the maximum heat output, or true SAR value, for each sample calculated.

The fact that the Fe@Cu nanoparticles discussed here were alloyed rather than core-shell in structure indicates that the synthesis method used in this work may provide a valuable means for producing magnetic alloy nanoparticles of interest, e.g. Fe-Co, Fe-Pd. Fe-Co alloys are well known, with Fe₆₀Co₄₀ being the material with the (current) highest saturation magnetisation. Nanocomposite films containing FeCo alloy nanoparticles would therefore be of much interest as candidates for new high moment materials. Given that enhanced moments are already known in embedded Fe and Co nanoparticles, Fe@Co and Co@Fe core-shell nanoparticles are also promising candidates as building blocks for new high moment materials. A detailed study into the morphology of Fe/Co nanoparticles produced by our synthesis technique would therefore be an important first step before carrying out a thorough magnetic characterisation.

References

- Amin, G. (2012). *EDN Network*. Retrieved from www.edn.com/Home/PrintView?contentItemId=4396478
- Atkas, S. (2014). Gas Phase Preparation of Magnetic Nanoparticle Hydrosols. *PhD, University of Leicester, Leicester*.
- Atkas, S., Thornton, S., Binns, C., Lari, L., Pratt, A., Kroeger, R., & Horsfield, M. (2015). Control of gas phase nanoparticle shape and its effect on MRI relaxivity. *Materials Research Express*.
- Atkinson, W. J., Brezovich, I. A., & Chakraborty, D. P. (1984). Usable Frequencies in Hyperthermia with Thermal Seeds. *IEEE Transactions on Biomedical Engineering, BME-31*, 70-75.
- Bahadur, D., & Giri, J. (2003). *Biomaterials and magnetism*. Sadhana.
- Baker, S., Asaduzzaman, A. M., Roy, M., Gurman, S. J., Binns, C., Blackman, J. A., & Xie, Y. (2008). Atomic structure and magnetic moments in cluster-assembled nanocomposite Fe/Cu films. *Physical Review B*.
- Baker, S., Thornton, S., Edmonds, W., Maher, M. J., Norris, C., & Binns, C. (2000). The construction of a gas aggregation source for the preparation of size-selected nanoscale transition metal clusters. *Review of Scientific Instruments*, 3178-3183.
- Binns, C. (2010). *Introduction to Nanoscience and Nanotechnology*. Wiley.
- Binns, C., Prieto, P., Baker, S., Howes, P., Dondi, R., Burley, G., . . . Mellon, J. (2012). Preparation of hydrosol suspensions of elemental and core-shell nanoparticles by co-deposition with water vapour from the gas-phase in ultra-high vacuum conditions. *J Nanopart Res*.
- Bloch, F. (1946). Nuclear Induction. *Phys Rev.*, 127.
- Bonnemann, H., Brijoux, W., Brinkmann, R., Matoussevitch, N., Waldofner, N., & Palina, N. (2003). A size-selective synthesis of air stable colloidal magnetic cobalt nanoparticles. *Inorganica Chimica Acta*, 617-624.
- Brusentsov, N. A., Nitkin, L. V., Brusentsova, T., Kuznetsov, A., Bayburtskiy, F., Shumakov, L. I., & Jurchenko, N. Y. (2002). Magnetic fluid hyperthermia of the mouse experimental tumor. *Journal of magnetism and magnetic materials*, 378-380.
- Campbell, N. A., & Reece, J. B. (2008). *Biology*. Pearson.

- Carrey, J., Mehdaoui, B., & Respaud, M. (2011). Simple models for dynamic hysteresis loop calculations of single-domain sized nanoparticles: Application to magnetic hyperthermia optimization. *Journal of Applied Physics*.
- Curie, P. (1895). Propriétés magnétiques des corps a diverses températures. *Gauthier-Villars et fils*.
- Davies, P. (2013). Exposing Cancer's Deep Evolutionary Roots. *Physics of Cancer*, 37-40.
- Dewhirst, M., Viglianti, B., Lora-Michiels, M., Hanson, M., & Hoopes, P. J. (2005). Basic principles of thermal dosimetry and thermal thresholds for tissue damage from hyperthermia. *Int. J. Hyperthermia*, 267-294.
- Electronics-micros*. (2017). Retrieved from www.electronics-micro.com
- Ferlay, J., Steliarova-Foucher, E., Loret-Tieulent, J., Rosso, S., Coebergh, J. W., Comber, H., . . . Bray, F. (2013). Cancer incidence and mortality patterns in Europe: estimates for 40 countries in 2012. *Eur J Cancer*, 1374-403.
- Foner, S. (1959). Versatile and Sensitive Vibrating-Sample Magnetometer*. *The Review of Scientific Instruments*.
- Fortin, J.-P., Wilhelm, C., Servais, J., Menager, C., Bacri, J.-C., & Gazeau, F. (2007). Size-sorted anionic iron oxide nanomagnetic as colloidal mediators for magnetic hyperthermia. *J. Am. Chem. Soc.*, 2628-2635.
- Gleich, B., & Weizenecker, J. (2005). Tomographic imaging using the nonlinear response of magnetic nanoparticles. *Nano Letters*, 1214-1217.
- Gleich, B., Weizenecker, J., Timminger, H., Bontus, C., Schamle, I., Rahmer, J., & Borgert, J. (2010). Fast MPI Demonstrator with Enlarged Field of View.
- Goodwill, P. (2009). Narrowband Magnetic Particle Imaging. *IEEE Transactions on Medical Imaging*, 8.
- Guardia, P., Di Corato, R., Lartigue, L., Wilhelm, C., Espinosa, A., Garcia-Hernandez, M., . . . Pellegrino, T. (2012). Water-soluble Iron Oxide Nanocubes with High Values of Specific Absorption Rate for Cancer Cell Hyperthermia Treatment. *ASC Nano*, 3080-3097.
- Hansen, M. (1958). *Constitution of Binary Alloys 2ed*. McGraw-Hill.
- Heck, C. (1974). *Magnetic Materials and Their Applications*. Butterworths.
- Hellerhoff. (2010). *Wikipedia*. Retrieved from https://en.wikipedia.org/wiki/MRI_contrast_agent#/media/File:Bluthirnschranke_nach_Infarkt_nativ_und_KM.png

- Hergt, R., Andra, W., d'Ambly, C., Hilger, I., Kaiser, W., Richter, U., & Schmidt, H.-G. (1998). Physical Limits of Hyperthermia Using Magnetite Fine Particles. *IEEE Trans. Magn.*, 3745-3754.
- Hergt, R., Dutz, S., Muller, R., & Zeisberger, M. (2006). Magnetic particle hyperthermia: nanoparticle magnetism and materials development for cancer therapy. *Journal of Physics: Condensed Matter*, 14, S2919-S2934.
- Kallimudil, M., Tada, M., Nakagawa, T., Abe, M., Southern, P., & Pankhurst, Q. (2009). Suitability of commercial colloids for magnetic nanoparticle hyperthermia. *J. Magn. Matter*, 1509-1513.
- King, R., & Robins, M. (2006). *Cancer Biology, 3rd Edition*. Pearson.
- Knopp, T., Biederer, S., Sattel, T., Weizenecker, J., Gleich, B., Borgert, J., & Buzug, T. M. (2009). Trajectory analysis for magnetic particle imaging. *Phys. Med. Biol.*, 385-397.
- Laurent, S., Dutz, S., Hafeli, U., & Mahmoudi, M. (2011). Magnetic fluid hyperthermia: Focus of superparamagnetic iron oxide nanoparticles. *Advances in Colloid and Interface Science*, 8-23.
- Lee, J.-H., Jang, J.-T., Choi, J.-S., & Moon, S. H. (2011). Exchange-coupled magnetic nanoparticles for efficient heat radiation. *Nature Nanotechnology Letters*, 418-422.
- Leicester University, P. D. (1990). LUXC Manual.
- Lenz, J. E. (1990). A Review of Magnetic Sensors. *Proceedings of the IEEE*.
- Maier-Hauff, K., Rothe, R., Scholz, R., Gneveckow, U., Wust, P., Thiesen, B., . . . Jordan, A. (2007). Intracranial thermotherapy using magnetic nanoparticles combined with external beam radiotherapy: results of a feasibility study on patients with glioblastoma multiforme. *J. Neurooncol.*, 53-60.
- Mehdaoui, B., Meffre, A., Lacroix, L.-M., Carrey, J., Lachaize, S., Gougeon, M., . . . Chaudret, B. (2010). Large specific absorption rates in the magnetic hyperthermia properties of metallic iron nanocubes. *Journal of Magnetism and Magnetic Materials*, 149-152.
- Milton, O. (2001). *Materials Science of Thin Films*. Academic Press.
- Morley, G. (2011, 11 25). *Wikimedia*. Retrieved from upload.wikimedia.org/wikipedia/commons/9/9b/HahnEcho_GWM.gif
- Moroz, P., Jones, S., & Gray, B. (21012). Tumor Response to Arterial Embolization Hyperthermia and Direct Injection Hyperthermia is a Rabbit Liver Tumor Model. *J. Surg. Oncol.*, 149-156.

- Na, H., Song, I., & Hyeon, T. (2009). Inorganic Nanoparticles for MRI Contrast Agents. *Adv. Mater.*, 2133-2148.
- Pankhurst, Q. A., Thanh, N., Jones, S. K., & Dobson, J. (2009). Progress in applications of magnetic nanoparticles in biomedicine. *J. Phys. D: Appl. Phys.*
- Pankhurst, Q., Connolly, J., Jones, S., & Dobson, J. (2003). Applications of magnetic nanoparticles in biomedicine. *J. Phys. D: Appl. Phys.*, 167-181.
- Pratt, A., Lari, L., Hovorka, O., Shah, A., Woffinden, C., Tear, S. P., . . . Kroeger, R. (2014). Enhanced oxidation of nanoparticles through strain-mediated ionic transport. *Nature Materials*, 26-30.
- Rosensweig, R. (2002). Heating magnetic fluid with alternating magnetic field. *Journal of Magnetism and Magnetic Materials*, 370-374.
- Sattel, T., Knopp, T., Biederer, S., Gleich, B., Weizenecker, J., Borgert, J., & Buzug, T. (2009). Single-sided device for magnetic particle imaging.
- Sears, F., & Sallinger, G. (1982). *Thermodynamics, Kinetic Theory, and Statistical Thermodynamics 3rd Edition*. Addison-Wesley.
- Softley, T. P. (1999). *Atomic Spectra*. Oxford University Press.
- Vallejo-Fernandez, G., & Whear, O. (2013). Mechanisms of hyperthermia in magnetic nanoparticles. *J. Appl. Phys.*
- Weaver, J., Rauwerdink, A., Sullivan, C., & Baker, I. (2008). Frequency distribution of the nanoparticle magnetization in the presence of a static as well as a harmonic magnetic field. *Med. Phys.*
- Webb. (1988). *The Physics of Medical Imaging*. IoP.
- Weizenecker, J., & Gleich, B. (2007). A simulation study on the resolution and sensitivity of magnetic particle imaging.
- Weizenecker, J., Gleich, B., Rahmer, J., Dahnke, H., & Borgert, J. (2009). Three-dimensional real-time in vivo magnetic particle imaging. *Phys. Med. Biol.*, 1-10.
- Williams, D. B., & Carter, B. C. (1996). *Transmission Electron Microscopy, Part 1: Basics*. Springer.
- Zhang, J.-M., Ma, F., & Xu, K.-W. (2004). Calculation of the surface energy of fcc metals with modified embedded-atom method. *Chinese Physics*, 1082-1090.
- Zureks. (2008). Retrieved from Wikipedia: https://commons.wikimedia.org/wiki/File:Powstawanie_domen_by_Zureks.png